A MEASUREMENT OF $\sigma \cdot B(Z^\circ \rightarrow \mu^+\mu^-)$ IN $P\bar{P}$ COLLISIONS AT $\sqrt{S} = 1.8$ TEV

BY

DAVID ANTHONY KARDELIS

B.S., University of Illinois at Urbana-Champaign, 1987
M.S., University of Illinois at Urbana-Champaign, 1987

THESIS

Submitted in partial fulfillment of the requirements
for the degree of Doctor of Philosophy in Physics
in the Graduate College of the
University of Illinois at Urbana-Champaign, 1994

Urbana, Illinois

UNIVERSITY OF ILLINOIS AT URBANA-CHAMPAIGN

THE GRADUATE COLLEGE

FEBRUARY 1, 1994

WE HEREBY RECOMMEND THAT THE THESIS BY

DAVID ANTHONY KARDELIS

ENTITLED A MEASUREMENT OF $\sigma \bullet B(Z^0 \rightarrow \mu^+\mu^-)$ IN $P\bar{P}$ COLLISIONS AT $\sqrt{S} = 1.8$ TEV

BE ACCEPTED IN PARTIAL FULFILLMENT OF THE REQUIREMENTS FOR THE DEGREE OF DOCTOR OF PHILOSOPHY

L. E. Holloway
Director of Thesis Research

Head of Department

Committee on Final Examination†

L. E. Holloway
Chairperson

F. K. Lamb

H. W. Wyld

† Required for doctor's degree but not for master's.

O-517

UNIVERSITY OF ILLINOIS AT URBANA-CHAMPAIGN

GRADUATE COLLEGE DEPARTMENTAL FORMAT APPROVAL

THIS IS TO CERTIFY THAT THE FORMAT AND QUALITY OF PRESENTATION OF THE THESIS SUBMITTED BY David Anthony Kardelis AS ONE OF THE REQUIREMENTS FOR THE DEGREE OF Doctor of Philosophy ARE ACCEPTABLE TO THE Department of Physics.

Full Name of Department, Division or Unit

3-3-94

Date of Approval

Departmental Representative

A Measurement of $\sigma \cdot B(Z^\circ \rightarrow \mu^+\mu^-)$ in $p\bar{p}$ collisions at $\sqrt{S} = 1.8$ TeV

David Anthony Kardelis, Ph.D.
Department of Physics
University of Illinois at Urbana-Champaign, 1994
Professor Lee Holloway, advisor

A measurement in the muon channel of Z° production cross sections times branching ratios yields $\sigma \cdot B(Z^\circ \rightarrow \mu^+\mu^-) = 228 \pm 22(stat) \pm 19(sys)$ nb where the largest uncertainty comes from the statistics of the data sample. The Standard Model predictions agree with the above results.

Acknowledgments

I would like to thank the multitude of people who contributed to my finishing my degree. I must start with my parents since they were the first to support me. They have always encouraged me in my education. I would also like to thank my wife, Erica, whose help, love and prodding helped me to finish.

I need to thank all the people at CDF who helped keep the detector up and running letting us take a great deal of data. I would especially like to thank Steve and Dee who not only kept CDF running smoothly but also kept us entertained by handling the various holiday and Collaboration parties. I would especially like to thank Sarah and Dave who overseered much of this analysis. They both urged detailed analysis, which was essential for the job be done right. I would also like to thank Ray who helped this analysis along in many ways. I would also like to thank Steve, Henry, Aesook, Peter, and Aseet, for without their help this project would have been even more daunting.

I would also like to thank my friends Ray and Chris who introduced me to several new hobbies. They also shared many a beer and complaint about this work. I would also like to thank George for believing in me, and Dale and Tom who took me out many times. They all helped me to get some distance from the work and enjoy the other things in life. Thanks

to the many friends made during the first year of graduate school that helped me learn and survive the experience.

I also need to thank the support of people at the U of I. Dave and Jerry, thanks for the help on the many VAX questions. I want to thank Shirley and Sue who helped keep me registered and completing various paper work that the university required. Thanks to Fred for showing me how to use the various shop equipment and answering my questions on tools and materials. And a great many thanks to Tom who managed to get the travel vouchers through quickly. I also would like to thank Fred Lamb for his questions at my defense that reminded me that why we make the measurement is at least as important as how we make the measurement. I would also like to thank Tony for his comments on my thesis and prelim. They were most helpful.

Lastly, I need to thank my advisor, Lee for without his help this work probably still be unfinished. Thanks for that occasional push when I needed it.

This work was supported in part by the U.S. Department of Energy through contracts DE-ACO276-ER01195 and DE-FG029-ER40677.

TABLE OF CONTENTS

Chapter

LIST OF TABLES

LIST OF FIGURES

Chapter 1

Introduction and Theory

1.1 The Standard Model

The best current theory to describe the interaction of fundamental particles is called the Standard Model. Since its development, the theory has been very successful in its predictions.

The Standard Model incorporates both Quantum Chromodynamics (QCD), and the Electro-Weak theory which includes Quantum Electrodynamics (QED). The model describes the interaction of the two types of fundamental particles, fermions and bosons. The fermions interact via the exchange of bosons which have integer spin and are the carriers of force.

The Electro-Weak theory proposed by Glashow, Weinberg and Salam, [1] unifies the electromagnetic and weak interactions into a single interaction described by the group $SU(2)_L \otimes U(1)_Y$. This merging of two previously separate forces into one described by particle exchange layed much of the groundwork for the Standard Model. The Electro-Weak

theory predicts the existence of the $W^{\pm}$ vector bosons which carry the charged weak current and is described totally by the $SU(2)_L$ sector. The theory also predicts 2 neutral vector bosons for the neutral current, which are the photon (γ) and the Z^0. The neutral currents contain elements of both $SU(2)_L$ and the $U(1)_Y$ sectors. The photon describes the electromagnetic forces of classical electricity and magnetism. The W bosons were discovered in 1983 [2, 3] and shortly thereafter the Z° was found [4, 5]. The intrinsic properties of the bosons, such as their mass, width, and production cross section, are of interest since the bosons are an integral part of the Electro-Weak theory.

In the Standard Model, the fermions are composed of 3 generations of quarks and leptons. Each fermion has a spin of $1/2\ \hbar$. The quarks are called up, down, strange, charm, top, and bottom. While top has not been experimentally seen, indirect evidence points to its existence. Each quark in addition to having mass and fractional electric charge also carries color, the "charge" of the strong force or QCD. There are three color charges, red, green, and blue. The nature of this "charge" prevents direct observation of color, that is particles must appear colorless or white. The leptons also have three generations of particles, electron, electron neutrino, muon, muon neutrino, tau, and tau neutrino. While the electron, muon and tau possess mass and unit electrical charge, they do not carry color. The neutrinos as far as can be determined are massless and have no electric charge. Neutrinos do not carry color. The properties of the basic fermions are summarized in table 1.1.

The Standard model uses 12 bosons to mediate interactions between the fermions. The bosons are the $W^{\pm}, Z^{\circ}, \gamma$, and eight gluons. The $W^{\pm}, Z^{\circ}$, and the photon(γ) are responsible

Fermion	mass	Electric charge	Color charge	spin
quarks				
u c t	Y	$+\frac{2}{3}$	Y	$\frac{1}{2}$
d s b	Y	$-\frac{1}{3}$	Y	$\frac{1}{2}$
leptons				
e μ τ	Y	-1	N	$\frac{1}{2}$
ν_e ν_μ ν_τ	N	0	N	$\frac{1}{2}$

Table 1.1: A summary of the fundamental fermion particles. The interaction between the fermions is mediated by boson exchange. The boson properties are summarized in table 1.2.

Particle	mass	Electric charge	Color charge	spin
W boson	Y	± 1	N	1
Z° boson	Y	0	N	1
γ	N	0	N	1
gluons	N	0	Y	1

Table 1.2: Summary of boson properties. In the Standard Model exchange of these bosons describes the interaction of fundamental properties.

for Electro-Weak interactions. The eight gluons carry the strong force and have color. Thus, gluons interact among themselves via the strong force. One other boson is required in the current version of the Standard Model. This particle is the Higgs boson and is believed to be responsible for the mass of all the other particles. As of yet, the Higgs particle has not been observed. This thesis discusses the production and decay of the Z° boson of the Electro-Weak theory.

1.2 Dilepton Production

Dilepton pairs with large invariant mass are produced through two processes, $q\bar{q} \rightarrow \mathrm{Z}^0 \rightarrow l\bar{l}$, and $q\bar{q} \rightarrow \gamma \rightarrow l\bar{l}$. The Feynmann diagrams for these processes are shown in figure 1.1 The Lagrangian for an arbitrary fermion interacting with a Z^0 boson is given by

$$\mathcal{L}_{nc} = -i\sqrt{2}\left(\frac{G_F M_Z^2}{\sqrt{2}}\right)^{1/2} \bar{\psi}\gamma^\mu (C_V^f - \gamma^5 C_A^f))\psi Z_\mu, \tag{1.1}$$

where the vector and axial vector couplings C_V^f and C_A^f are given by

$$C_V^f = T_3 - 2Q\sin^2\theta_W \qquad C_A^f = T_3,$$

with T_3 being the third component of weak isospin and Q the charge of the fermion. The Fermi constant G_F is given by

$$G_F = \frac{g^2\sqrt{2}}{8M_W^2}.$$

M_Z and M_W are the masses of the Z° and $\mathrm{W}^\pm$ bosons respectively. A fermion interacting with a photon has a Lagrangian given by

$$\mathcal{L}_{em} = -iQ_f\bar{\psi}\gamma^\mu\psi A_\mu. \tag{1.2}$$

Experimentally, the two subprocesses $q\bar{q} \rightarrow \mathrm{Z}^0 \rightarrow l\bar{l}$ and $q\bar{q} \rightarrow \gamma \rightarrow l\bar{l}$ are indistinguishable, since the intermediate state is not directly observed. Therefore, the matrix element for

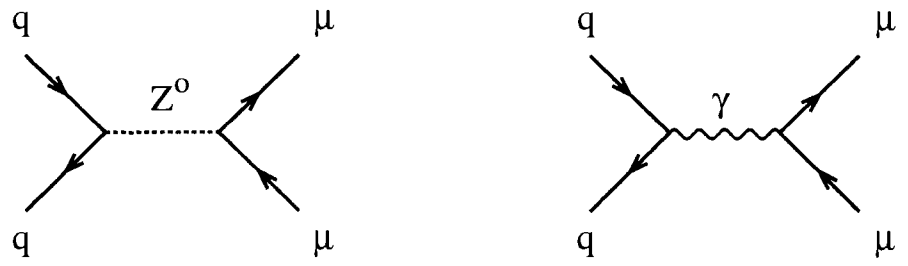

Figure 1.1: The Feynmann diagrams describing boson production and subsequent decay into two muons.

$q\bar{q} \rightarrow l\bar{l}$ is given by the sum of the subprocess matrix elements. Using the Feynmann Rules to insert the vertex factors directly, the overall matrix element is

$$\begin{aligned}\mathcal{M} &= -\left(\frac{2G_F M_Z^2}{\sqrt{2}}\right)\bar{v}_{\bar{q}}\gamma^\mu(C_V^q - \gamma^5 C_A^q)u_q\left(\frac{g_{\mu\nu} - P_\mu P_\nu/M_Z^2}{P^2 - M_Z^2}\right)\bar{u}_l\gamma^\nu(C_V^l - \gamma^5 C_A^l)v_{\bar{l}} \\ &\quad -(Q_q Q_l)\bar{v}_{\bar{q}}\gamma^\alpha u_q\left(\frac{g_{\alpha\beta}}{P^2}\right)\bar{u}_l\gamma^\beta v_{\bar{l}} \qquad (1.3)\end{aligned}$$

Calculating the cross section for the $q\bar{q} \rightarrow \mu^+\mu^-$ yields

$$\begin{aligned}\frac{d\sigma}{d\Omega} &= \frac{\alpha^2 Q_q^2}{4\hat{s}}(1+\cos^2\hat{\theta}) \\ &\quad -\frac{\alpha G_f M_Z^2 Q_q(\hat{s}-M_Z^2)}{4\sqrt{2}\pi[(\hat{s}-M_Z^2)^2 + M_Z^2\Gamma_Z^2]}(C_V^l C_V^q(1+\cos^2\hat{\theta}) + 2C_A^l C_A^q\cos\hat{\theta}) + \\ &\quad \frac{G_f^2 M_Z^4 \hat{s}}{128\pi^2[(\hat{s}-M_z^2)^2 + M_Z^2\Gamma_Z^2]}[(C_R^l C_R^q + C_L^l C_L^q)(1+\cos\hat{\theta})^2 + (C_L^l C_R^q + C_R^l C_L^q)(1-\cos\hat{\theta})^2]\end{aligned}$$

Where Γ_Z is the width of the Z° resonance, $\hat{s}$ is the center of mass collision energy, $\hat{\theta}$ is the scattering angle between the quark and lepton in the center of mass frame and

$$C_R = C_V - C_A \qquad C_L = C_V + C_A.$$

The first term in the cross section is due to the photon propagator (Drell Yan contribution), while the third term is due to the Z^0, and the second term is due to the quantum mechanical interference of the photon and Z^0 propagators.

Since the reaction being studied involves proton anti-proton collisions and not free quark collisions, the parton model is used to calculate the cross section. In the parton model, the proton is composed of 'valence' quarks, 'sea' quarks, and gluons. The 'valence' quarks define the proton's characteristics such as charge. The 'sea' quarks are virtual $q\bar{q}$ pairs created by gluon decay. Gluons are the mediator of the strong force which holds the proton together. Each parton within the proton carries some momentum fraction x_{parton} of the proton's total momentum P and energy E, *i.e.*, $P_{parton} = x_{parton} \times P_{proton}$. The distribution of momenta for the partons in the proton are obtained from deep inelastic scattering usually involving leptons scattering off hadrons.

Most deep inelastic scattering experiments have been fixed target experiments operating at fairly low energy compared to $\sqrt{s} = 1.8$ TeV. Fortunately, the Altarelli-Parisi [6] equations allow us to extrapolate the parton distribution functions from one energy to another energy by making use of QCD rules. These equations express the fact that a low energy quark could have started as a higher energy quark that radiated a gluon. The parton distribution functions of HMRSB[7] are plotted in figure 1.2. Sea distributions dominate at low x, valence distributions become more important at large x. This result is expected, since at low x more particles are needed to carry the proton's momentum. Since the number of valence quarks

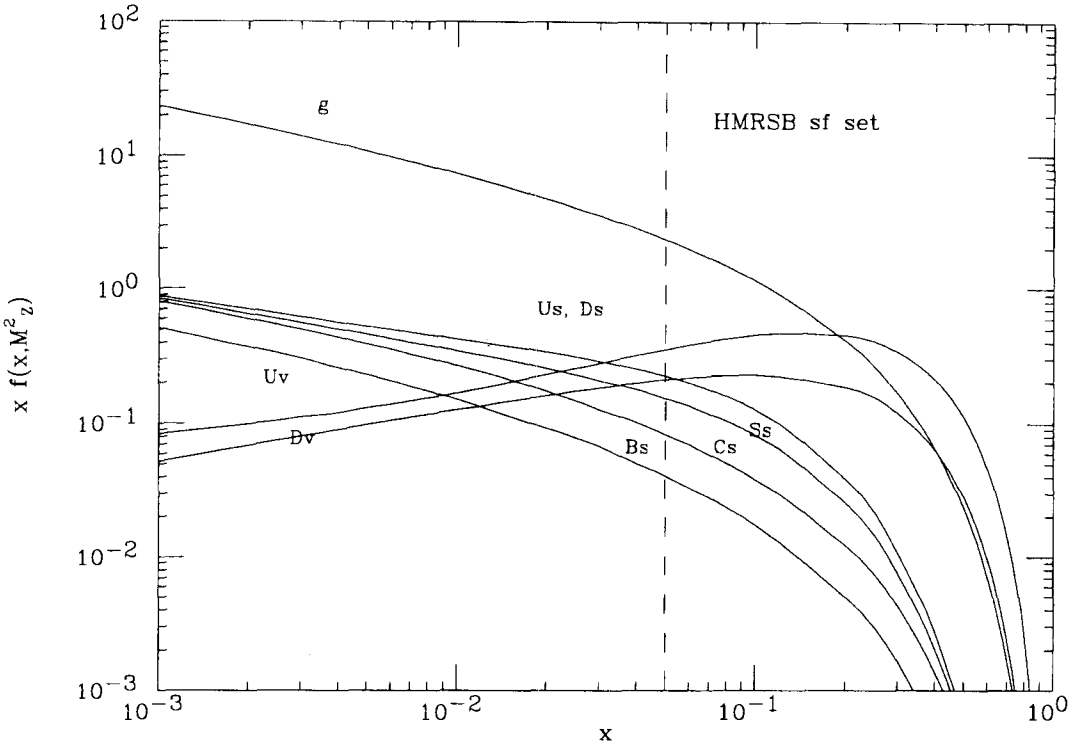

Figure 1.2: The HMRSB parton distribution functions for a proton. The subscripts denote valence (V) or sea (S) quarks. The gluon curve (g) is also shown. The dashed line is the position where Z° bosons will be created on the mass shell. From the value of each curve at the dashed line, the relative contributions for each parton type can be determined.

is fixed, the extra particles must be gluons and sea quarks. It is these functions $f(x)$ that are contained in the final form of the cross section given below.

To calculate the cross section for Z° production, the colors and flavors of quarks must be accounted for. The sum over quark flavors should include all 6 flavors of the Standard Model due to the presence of the sea, though the higher mass of the c,b,t quarks will lower their contribution to the cross section. In terms of these parton distribution functions $f_p(x)$,

the cross section becomes

$$\frac{d\sigma}{d\Omega dQ^2} = \frac{1}{3}\times\frac{1}{3}\times 3\times\frac{1}{Q^2} \times\sum_q\int_0^1 dx_{\bar{q}}\int_0^1 dx_q[f_{\bar{p}}(x_{\bar{q}})f_p(x_q)+f_p(x_{\bar{q}})f_{\bar{p}}(x_q)]\frac{d\sigma}{d\Omega}\delta(1-x_q x_{\bar{q}}\frac{s}{Q^2}) \quad (1.4)$$

where

$$Q^2=(P_q+P_{\bar{q}})^2=\hat{s}, \qquad \hat{s}\simeq x_q x_{\bar{q}} s,$$

and $f_p(x_q)$ is the probability of finding quark q with momentum fraction x_q within the proton. The factors of a third are from the average over incoming quark colors and the factor of three comes from the number of combinations that will give a colorless object. If the number of colors is not three but four, the predicted cross section would be changed by 25%.

1.3 Boson Decay

In the Standard Model, there are 5 possible quark-antiquark pairs open to the decay, since the mass of the top quark is more than $M_Z/2$[8], and 6 lepton-antilepton pairs open to the Z°. Since there are 3 quark colors, there are 21 possible final states. To determine the branching ratio requires the calculation of the partial width of the decay to muons and the total width of the decay taking into account all masses and phase space considerations. The theoretical partial width to massless fermions is $\Gamma(Z^\circ\rightarrow\mu^+\mu^-)=83.5\pm0.1$ MeV and and total width, $\Gamma_{total}(Z^\circ)=2.487\pm0.002$ GeV[9]. Using these numbers the branching ratio becomes 3.37%. The measured values are $B(Z^\circ\rightarrow\mu^+\mu^-)=3.34\pm0.04\%$ and $\Gamma_{total}(Z^\circ)=2.487\pm0.010$

GeV[10]. While this is relatively small branching ratio, the signal for the muon signal is very clean.

1.4 Analysis

Equation 1.4 with the help of parton distribution functions can be used to calculate the total cross section for production of Z° bosons and the branching ratio allows us to determine what fraction of those bosons are expected to decay into two muons. To actually make a measurement of the cross section we must count the number of events seen as dimuon events that came from a Z° boson.

The number of Z° bosons created is simply

$$N_Z^{created} = \sigma(Z^\circ \rightarrow \mu^+\mu^-) \cdot \int \mathcal{L}dt \tag{1.5}$$

where $\sigma(Z^\circ \rightarrow \mu^+\mu^-)$ is the cross section for producing Z°'s which decay into two muons and $\int \mathcal{L}dt$ is the time integrated luminosity. We define luminosity, $\mathcal{L}$, to be the product of incident beam flux, measured in particles per second, with mean target density, measured in particles per unit area. For a process with a cross section given by σ, the rate at which the process proceeds is given by $\sigma \cdot \mathcal{L}$. The luminosity is actually determined at CDF by measuring the rate for a process with a known cross section.

Unfortunately the number of dimuon events seen will contain some amount of non-signal or background events,

$$N_Z^{obs} = N_Z^{sig} + N_Z^{bkg}. \tag{1.6}$$

The number of events observed will depend on the number of bosons created as well as the requirements placed upon the sample and the physical geometry of the muon detectors. To account for this dependance, we introduce two terms, ϵ, the efficiency of the selection criteria and A_Z, the acceptance of the geometry of the detector and the characteristics of the Z° decay into two muons. The number of signal events then becomes

$$N_Z^{sig} = A_Z \cdot \epsilon \cdot N_Z^{created}. \tag{1.7}$$

In reality, the combination of A_Z and ϵ is more complicated than a simple multiplication due to the multiple event topologies for the two muons. This is discussed in more detail in chapter 8. Rewriting equations 1.7 and 1.5, we obtain

$$\sigma(Z^\circ \rightarrow \mu^+\mu^-) = \frac{N_Z^{obs} - N_Z^{bkg}}{A_Z \cdot \epsilon \cdot \int \mathcal{L}dt} = \frac{N_Z^{sig}}{A_Z \cdot \epsilon \cdot \int \mathcal{L}dt}. \tag{1.8}$$

We will use equation 1.8 to guide our analysis of the data taken at the Collider Detector at Fermilab. We will determine the efficiency of event selection using muon data collected at CDF. We will use monte carlo generators that apply equation 1.4 and experimentally determined parton distribution functions to determine our geometrical and kinematic acceptance.

We will then determine the number of background events contained in the observed sample. These values will be combined together to determine the value of $\sigma(Z^\circ \rightarrow \mu^+\mu^-)$.

Chapter 2

Detector

The CDF detector is a multi-purpose detector designed to study $p\bar{p}$ collisions at the Fermi National Accelerator Laboratory's Tevatron accelerator. The detector features near 4-π coverage and is both azimuthally and forward-backward symmetric. Event analysis is based on particles' charge and momentum measurements, tracking information and energy deposition in a calorimeter. A side view of the CDF detector is shown in Figure 2.1. Particles from $p\bar{p}$ collisions move outward from the interaction point in a 1.4 T magnetic field, through the beam pipe and into the CDF detector. First, particles from the collision enter a charged particle tracking chamber, then pass through sampling electromagnetic and hadronic calorimeters and finally, the muon chambers. To describe all the details of the CDF detector would be beyond the scope of this paper, but the complete CDF detector is described in *The Collider Detector at Fermilab*[11]. Instead, we will concentrate on the relevant subsystems of the CDF detector used in the analysis and detection of $Z^{\circ} \rightarrow \mu^{+}\mu^{-}$ events.

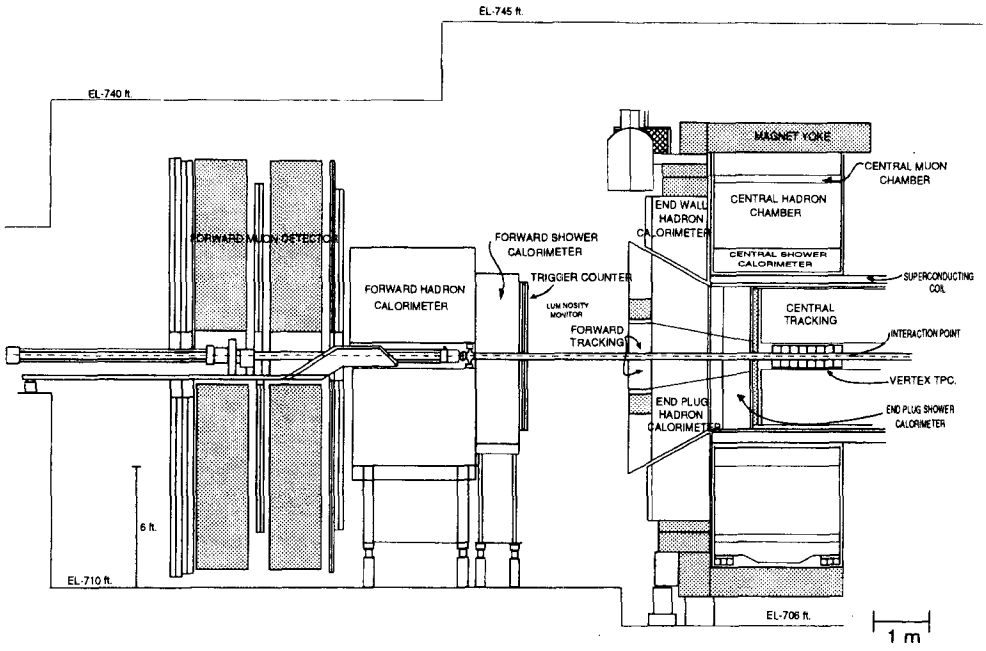

Figure 2.1: Cross section of one half of the CDF detector. The detector is symmetric about the midplane ($\eta = 0$) and roughly symmetric around the beam axis

2.1 Tracking Chambers

Two systems compose the tracking system at CDF, the Vertex Time Projection Chamber (VTPC) and the Central Tracking Chamber (CTC).

The VTPC surrounds the beam pipe and is 30 cm in radius. The VTPC provides track position measurements down to very small angles (polar angles of 8 to 172 degrees), but does not give any momentum information. The VTPC is also used to determine the Z position of the interaction point with a resolution better than 1.1mm in Z[12].

Physically, the Central Tracking Chamber (CTC) is cylindrical and has a 0.3 meter inner radius, a 1.3 meter outer radius, and is 3.2 meters long. This cylinder surrounds the VTPC in a 1.4 Tesla solenoidal magnetic field. The Central Tracking Chamber (CTC) is used to reconstruct the paths or tracks of charged particles traversing the detector. The CTC consists of 84 layers of sense wires, grouped into alternating layers of axial and stereo superlayers. The axial layers contain 12 wires and each stereo layer has 6 wires. The stereo wires are tilted at an angle of 3^o to the beam direction to obtain information on the polar angle of the track, while the axial wires are parallel to the beam direction. The Central Tracking Chamber provides precise momentum and position measurements of tracks for $|\eta|$[1] ≤ 1.0, where the CTC is highly efficient at finding tracks[13]. The efficiency of finding tracks and the resolution of the resulting tracks falls off as the polar angle increases and less of the 84 wires are traversed by the track. Requiring the track to originate at the beam position effectively lengthens the track, resulting in increased resolution. A beam's eye view of the

[1] η is defined by $\eta = -ln(\tan(\theta/2))$, and θ is the polar angle.

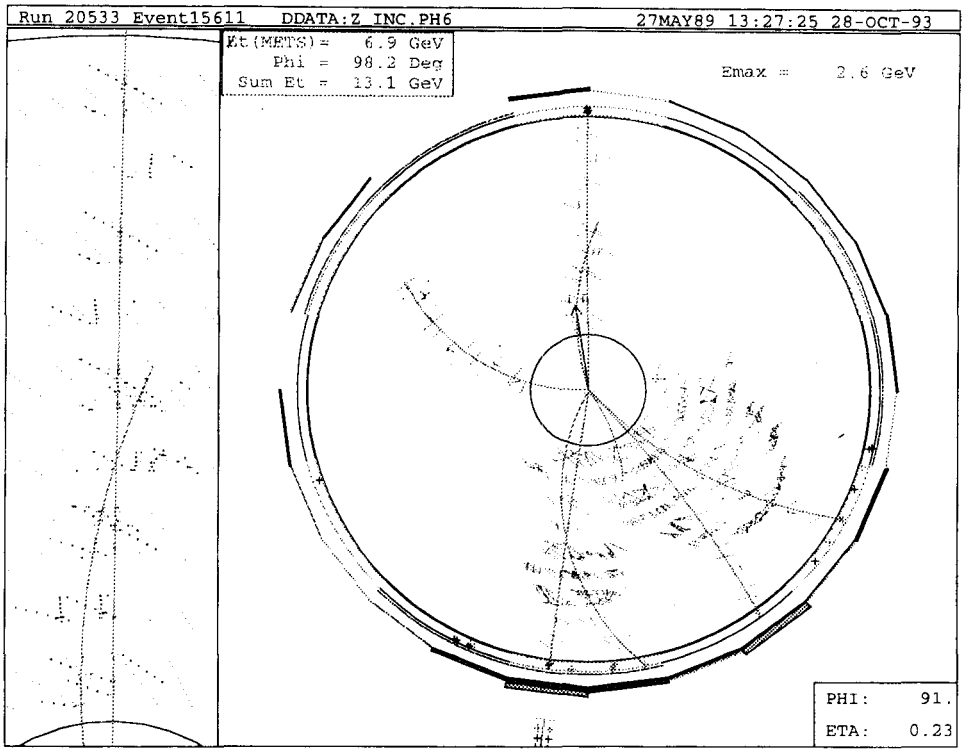

Figure 2.2: Event Display of Central Tracking Chamber with close up on two found tracks showing the stereo and axial wire positions.

Central Tracking Chamber is shown in an event display, figure 2.2. On the right of figure 2.2, we see the Central Tracking Chamber. The lines emanating out of the center circle, where the VTPC would rest, represent reconstructed tracks found in the Central Tracking Chamber. On the left side of figure 2.2, a close up of the two tracks found at the top of the main figure is shown. The shorter track is at large η and leaves the tracking chamber before reaching the outer wires. The second longer track passes past all 84 layers. In the close up, the axial and stereo wires can be seen.

2.2 Central Calorimeters

While the CDF calorimeters covers the range of 2^o to 178^o in polar angle, the detection of $Z^o \rightarrow \mu^+\mu^-$ events uses only the Central Calorimeter, which covers the region of $|\eta| \leq 1.1$ and 2π azimuthally. The central calorimetry is divided longitudinally at $\eta = 0.0$, the midpoint of the detector. Each side is composed of 24 wedges with each wedge covering 15 degrees of azimuthal angle. These 48 wedges also enclose the Central Muon System to be described later.

The central calorimeter is divided into two sections, the Central Electromagnetic calorimeter (CEM) and the Central Hadronic calorimeter (CHA). Both calorimeters are segmented into projective towers that point toward the beam's interaction point. These towers are approximately 0.1 in η and 15^o in ϕ in size. The projective design of the calorimeter can be seen in a event display of a Z° candidate shown in figure 2.3. This figure also shows the relationship of the Central Tracking Chamber and the central calorimetry. The other calorimeters locations are shown but not of particular interest to us. The CEM is composed of alternating layers of lead and polystyrene scintillator. The CEM has 18 radiation lengths of material and is equivalent to almost 1 pion absorbtion length of material. [14]. The CEM detector also has a shower detector located behind 6 radiation lengths of material to determine shower shape and position. The ability to measure showers is not used in this analysis. The CHA is of a similar design as the CEM but uses layers of steel and acrylic scintillators. The CHA has about 4.5 pion absorbtion lengths of materials.[15]

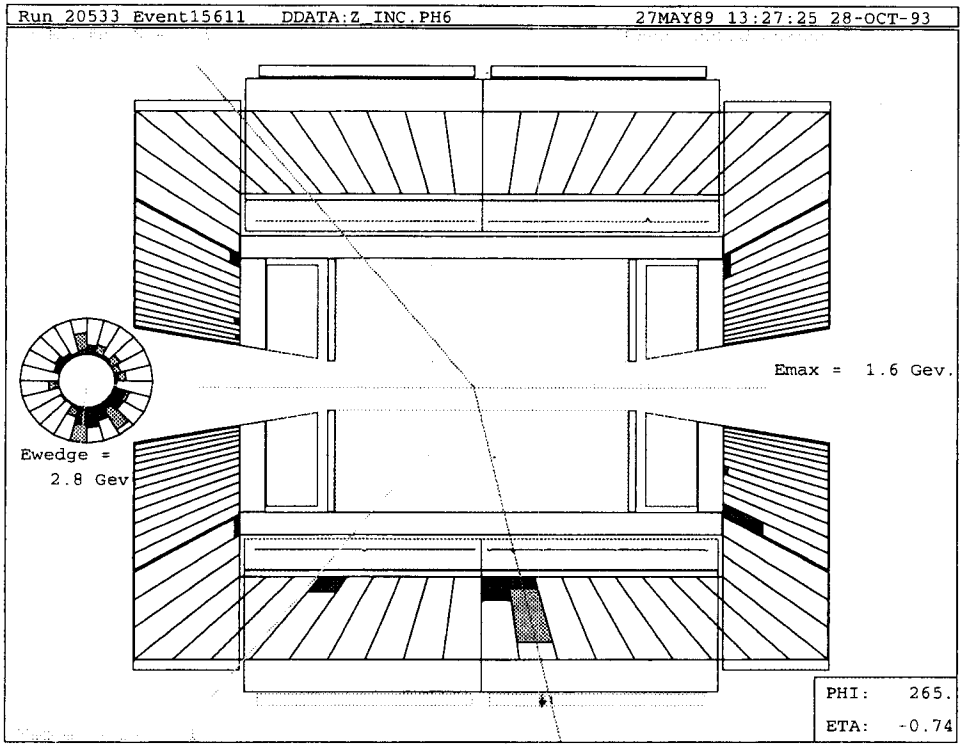

Figure 2.3: The event display shows the projective design of the calorimeters, and the relations between the three main detectors used in this analysis. In the very middle, tracks in the Central Tracking Chamber are shown. These tracks are shown pointing through the central calorimeter. Places where energy was deposited in electromagnetic calorimeters are shown as dark grey, hadronic energy deposition is shown as light grey. The amount of shaded area is proportional to the energy deposited. At the very top and bottom, an outline of the Central Muon Chambers are shown. The bottom track points towards hits in the muon chambers. At the top, a second track points into a region without muon detectors.

2.3 Central Muon System

The Central Muon System (CMU) is located beyond the tracking chambers, solenoid and central calorimetry at a distance of 3.48 meters from the beam axis. There are approximately 5 absorption lengths of material between the beam axis and the CMU detector. The CMU system is split into 48 identical subsystems each contained within one of the calorimeter wedges described earlier. Each subsystem is made of three smaller chambers to allow installation inside the wedge. Once inside the wedge, the three separate chambers are bolted together. Each of the smaller chambers has 16 cells, 4 layers deep and 4 towers wide. To save on the number of readout electronics needed, wires of alternate towers on each layer are ganged together. These ganged towers are used in the Level 1 and Level 2 Muon trigger. The sense wires for these cells lie on a radial line projecting from the beam axis. Since only the drift time is measured, a left-right ambiguity exists since the particle could have passed through the detector on either side of the wire. Wires for alternate layers are offset from the this radial line by 2mm to resolve this ambiguity of hits in the chamber.[16] An end view of one CMU chamber is shown in figure 2.4. The 2mm offset can be seen as the distance of the center dots representing the sense wires from the dashed radial line. One set of wires falls on the dashed line while the other pair is offset. The CMU position in the calorimeter wedge and its relative position to the rest of the detector is shown in figure 2.5, also visible are the gaps around the chambers.

For the data readout, each ganged pair of the CMU uses one time to voltage converter and two charge to voltage converters. The time to voltage converter measures drift times

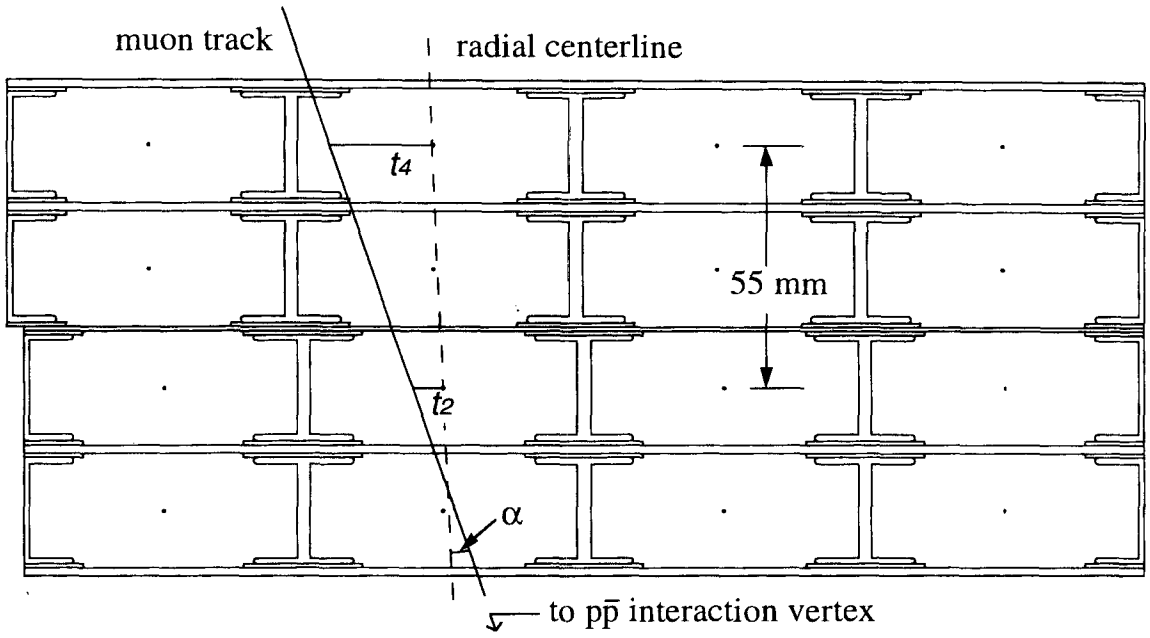

Figure 2.4: Edge View of CMU Chambers, showing the 2 mm offset in wire pairs. Also shown is the cell spacing and the timing information used in the trigger.

for each cell, shown as t_4, t_2 in figure 2.4. The timing information for the remaining two wire pairs is also used to measure drift time. These times are used to determine the X-Y position of the particle's path through the CMU chamber. Both ends of the wire pair are read out using the charge to voltage converters. By comparing the charge on each end, charge division, the particle's position in the Z direction can be determined. The timing difference between the alternating layers $(t_4 - t_2, t_3 - t_1)$ determines the angle, α, of the particle's path through the muon chamber. This angle, α, is used by the trigger which is described later in section 3.2.

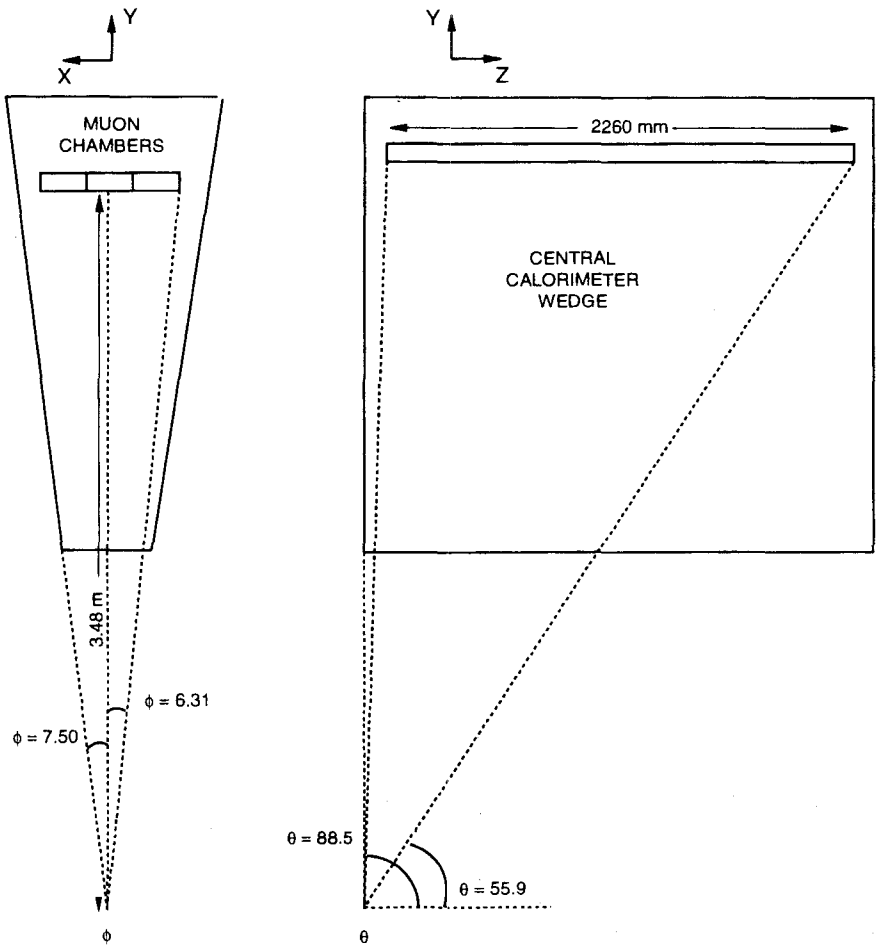

Figure 2.5: The Central Muon Chamber's position within a wedge is shown. The Central Muon Chamber position sits at a point 3.48 meters from the beam axis. The gaps caused by the chambers placement inside the calorimeter wedges are readily seen.

2.4 Luminosity Monitors

CDF uses scintillator planes located 5.8 meters from the nominal interaction point on either side of the detector. The planes known as Beam Beam Counters (BBC) have good timing resolution (<200ps) and provide the best measurement on the time of the interaction. The counters are used in coincidence to signal inelastic collisions for the trigger. These counters are also used to measure the small angle total cross section which provides CDF with a total luminosity measurement[17]. We get measure the luminosity from coincidence rate of the Beam Beam Counter's. Combining information from the Beam Beam Counters with other accelerator information yields an uncertainty in the luminosity measurement of 6.8%[18].

2.5 Data Acquisition

The data acquisition system used at CDF consists of several parts, the readout electronics which convert the individual detector components' analog signals into digital values, the trigger which determines which events are written to tape, and the event management system which gathers together all the components of a single event. A block diagram of the CDF data path is shown in figure 2.6.

The readout electronics are divided into two types, the RABBIT (Redundant Analog Bus Based Information Transfer) system and FASTBUS. The RABBIT system was designed by the Fermilab Particle Information Group and is used by the Central Muon Chambers and all of the CDF calorimetry systems [19]. FASTBUS is a commercially available data

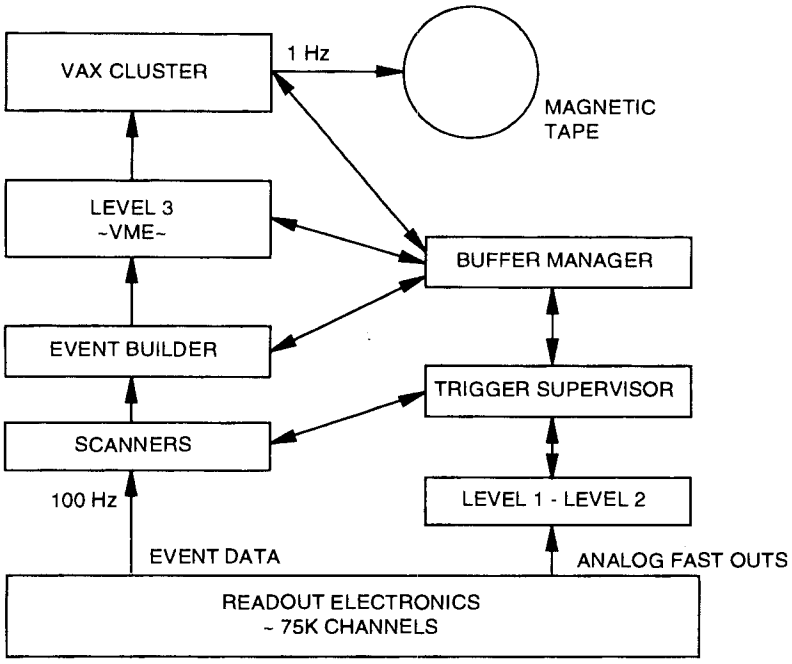

Figure 2.6: Block diagram showing the data acquisition path and connections.

acquisition system used at CDF to readout the tracking chambers and the trigger logic [20]. Management of the data taking was handled by the FASTBUS system in combination with a DEC VAX cluster. The FASTBUS components of the data taking system were the trigger supervisor, the buffer manager, and the event builder. The trigger supervisor assigned an event number to each event and signaled the other components in the system when all the detectors components were finished digitizing. The event builder took all the digitized signals for one event and gathered them up into individual detector banks. The buffer manager kept track of where all the data for each event is stored until it reaches final output to tape. The buffer manager also checked the format of the data. The FASTBUS system was directly connected to the DEC VAX cluster which wrote the data to tape.

Chapter 3

The Trigger

The trigger system at CDF during the 1988-89 run consisted of four levels. Each level, 0 through 3, had increasingly tighter requirements to select specific types of physics events out of the sea of interactions. The various levels and requirements of the trigger used in this analysis are described in this chapter. The efficiencies for the trigger will be discussed in Chapter 5.

3.1 Level 0 Trigger

The lowest level of the CDF trigger system was the Level 0 Trigger and was required for all higher level triggers. This trigger required a coincidence of hits in the two Beam-Beam Counters(BBC). This coincidence of hits was required to come within a 15 ns window centered on a 20ns delay after the expected $p\bar{p}$ interaction time [17]. This 20 ns delay allows for particles to reach the BBC counters from the interaction point. This trigger helped determine that

the event was from a real $p\bar{p}$ interaction and not from background events like cosmic rays. These same Beam Beam Counters were used in conjunction with accelerator parameters to calculate the luminosity delivered to the experiment.

3.2 Level 1 Muon Trigger

The next requirement to be satisfied is the Level 1 trigger. In this analysis, the Level 1 High-p_T Muon trigger was used. The trigger, at this level, required only information from the muon chambers. The Level 1 trigger decision is made in less than 7 microseconds. If the trigger is not satisfied, the electronics are reset so the detector is ready for another beam crossing.

The trigger uses the time difference from alternating layers of hits within a muon tower. This time difference is related to the angle of the muons path through the chambers. This angle, α, is related to the transverse momentum, p_T, of the particle by

$$\alpha \approx sin(\alpha) = eL^2B/2Dp_T$$

where L is the solenoid's radius, B is the magnetic field strength, D is the radius at the muon chambers, and p_T is the transverse momentum of the muon. This angular relationship is shown in figure 3.1. Then, the relationship between α and the time difference δt is then

$$\delta t = H\alpha/v$$

where H is 55.0mm, the separation between alternate wire layers, and v, is the drift velocity of the ionized electrons(50 μm/nS). The relation of α and $t_4 - t_2$ is seen in figure 2.4. Since muons are affected by multiple scattering, this relationship between angle and momentum is not exact [21].

The trigger checks the minimum time difference between alternate layers and compares it to the trigger threshold which is preset in the Muon Level 1 Trigger card. If the measured minimum time difference is less than the preset threshold,

$$MIN(t_4 - t_2, t_3 - t_1) \leq threshold$$

the Level 1 Muon trigger is satisfied.

During the 1988-89 run, there were two Level 1 muon trigger thresholds used, a 3 GeV/c and a 5 GeV/c p_T threshold [22]. While there were two Level 1 thresholds, this does not affect this cross-section measurement since the events selected for this analysis are far above threshold and well into the plateau region of the trigger efficiency.

3.3 Level 2 Muon Trigger

The Level 2 Muon trigger required that a track in the Central Tracking Chamber match the Level 1 Muon trigger tower within 15° in phi. To allow for trigger decisions to be made quickly online and to reduce deadtime from extraneous triggers, two-dimensional track finding was done by the Central Fast Tracker (CFT). These decisions were typically made

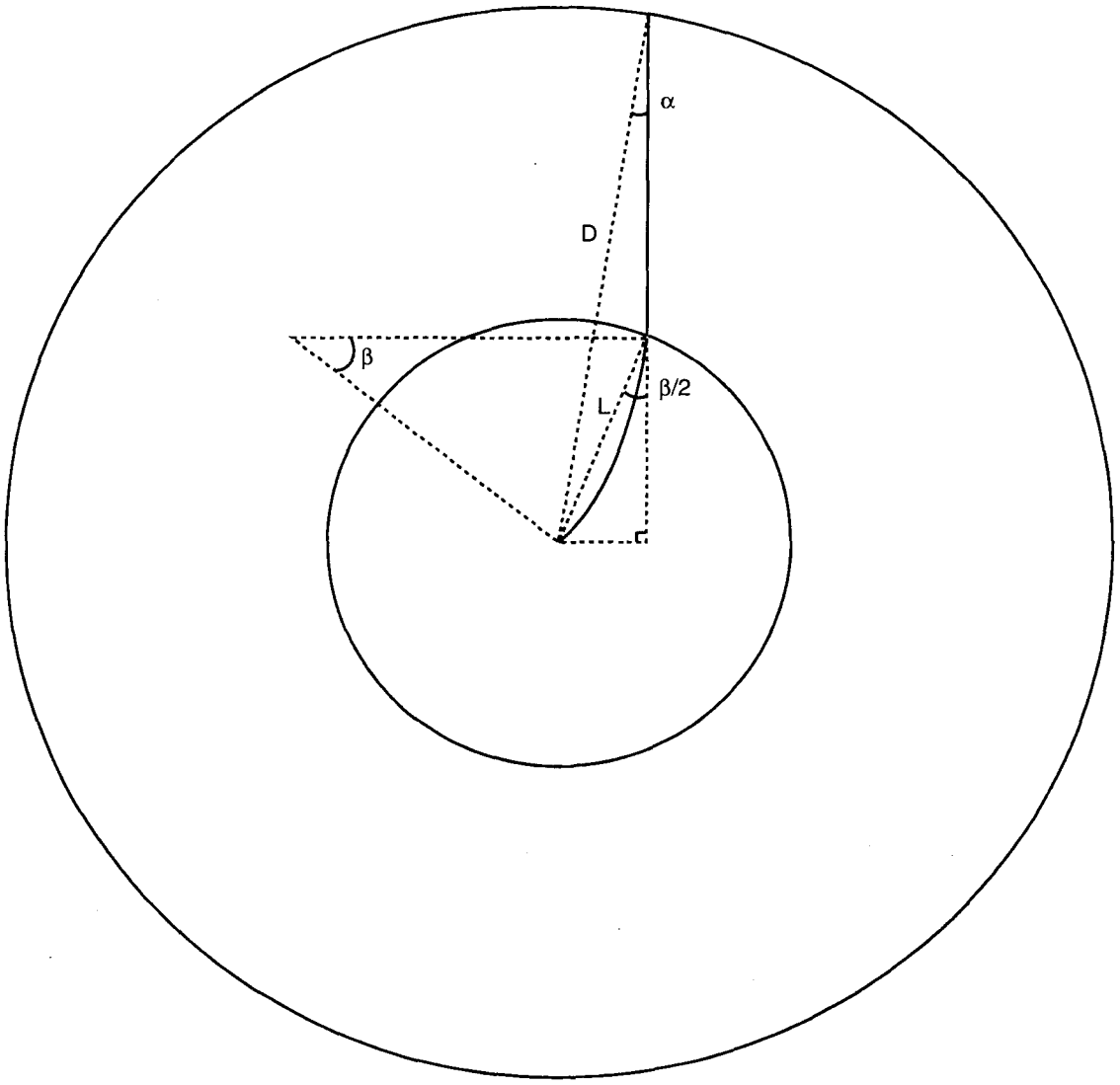

Figure 3.1: Shown is the relationship between a particle's p_T and the angle α. The relationship is not exact due to multiple scattering of the particle and the presence of a small magnetic return field.

in 10 microseconds [23]. The CFT had premapped hits stored according to several pt bins. Thus, the CFT would compare hits in the CTC with those predicted for a given p_T bin. The p_T bin required in the Level 2 Muon trigger was 90% efficient for a 9.2 GeV/c transverse momentum track [24].

3.4 Level 3 Muon Trigger

The Level 3 Muon trigger, the final stage of the muon trigger system, was a software program used to confirm the existence of a high p_T track from the CFT. The Level 3 code would use data from the Central Tracking Chamber to perform fast two dimensional tracking online. The code would then require a reconstructed track of $p_T \geq 11$ GeV/c to match a Level 1 muon trigger. An extrapolated track had to match the muon wire position associated with the Level 1 Trigger within 10 cm in the R-phi plane. Since two wires were paired together, a trigger could have occurred in either of the 2 cells causing an ambiguity in the path of the particle. Since both ends are read out, through the use of charge division, it is possible to distinguish which cell the particle passed through. In these cases, the track had to match the specific wire within 10 cm [25].

Chapter 4

Event Selection

The collider at CDF created large amount of data to be analysed. Even after the weeding done by the hardware physics trigger requirements, there are still several million events to be analysed. The raw data was not very amenable to simple physics analysis, because the data for each event had not been organized or reconstructed into objects that can be used to study the physics in each event.

4.1 Production/Reconstruction

The data from the various detector components are combined together to form potential physics objects such as muons, electrons and jets using a computer program called **PRODUCTION_V5_1**[26]. **PRODUCTION_V5_1** generates these objects in several steps, starting with detector elements and finishing with the physics objects. Detector elements are usually individual pieces of data for one detector subsystem. Detector elements are then

combined into detector segments using the information in the geometric and calibration databases. Each subsystem creates these detector segments in its own way. For example, tracks are identified in the central tracking chamber with the use of pattern recognition code and track fitting algorithms that link individual pieces of CTC wire data into complete tracks. The muon segment reconstruction algorithm is similar to the tracking algorithm in that it combines individual hits within a single muon chamber into a track segment called a stub(CMUS). These different detector elements are then combined to form the physics objects.

For this analysis, the reconstruction of central muon objects (CMUO) is of the most interest. In order to make these CMUO data elements, it is required that there be a central muon segment(CMUS) or stub as well as a central tracking chamber segment(CTCS). To limit the number of false CTCS-CMUS matches, the CTCS track must extrapolate to the CMU stub and the agreement between the CMU stub position and the extrapolated track(δX) must be within 17.0 cm in the $R-\phi$ plane. This requirement as we will see later is very loose for real muons. While the track is being extrapolated, information about the calorimeter towers that the "muon " has traversed is also collected. If the CTCS-CMUO match is acceptable, the muon candidate is put into its own data bank containing the relevant calorimeter and tracking information. If there were more than one possible muon in a single event, each muon receives its own CMUO data bank filled with the appropriate information[27].

Another type of physics object of interest in this analysis is a central minimum ionizing object(CMIO). This physics object is formed when a CTCS track has a transverse momen-

tum, $p_T \geq 10$ GeV/c but does not have a CMU stub associated with the track segment. This track is then extrapolated through the detector and the relevant calorimeter information around this track is recorded. This physics object is used to find muons in the regions where there are no muon detectors (i.e., the cracks between wedges), but there is good tracking and calorimeter information available. In figure 2.3, the track shown at the top is a CMIO muon.

4.1.1 Production Output

Once these physics objects are created, a general filter is used to break the complete data set into various output streams. This is useful since different physics analyses require different types of events. There were several output streams, but only the inclusive muon output stream is of interest in this analysis. Any event containing at least one CMUO data bank is included in this stream. Before final output of this stream to tape, several loose selection cuts are made to try and eliminate signals of fake muons. The routine that does this filtering of background events is called GMUFLT[28]. GMUFLT makes two cuts that the data must pass in order to make it through the filter. These cuts are:

- The match between the CTCS track's extrapolated position and muon stub(CMUS) position be less than 10 cm in magnitude in the $R - \phi$ plane.

- The muon must pass a trigger dependent p_T cut. For this analysis using the high p_T single muon trigger, the requirement was a muon with $p_T \geq 9.0$ GeV/c. The p_T is determined from the CTCS track information.

Any event that contained a CMUO bank that passes the above two cuts is included in the inclusive muon data stream. The 1988-89 collider run produced approximately 600,000 events of inclusive muon data on 150 8mm data tapes.

A sample of high p_T CMUO events was selected from these 150 tapes of muon data. Events were selected by the large transverse momentum of the muon and energy deposition consistent with that of a minimum ionizing particle traversing the calorimeter. First, we require events that had a CMUO bank with a transverse momentum, $p_T \geq 18.0$ GeV/c, energy deposition in the electromagnetic calorimeter in the tower, $E_{EM} \leq 2.0$ GeV, and energy deposition in the hadronic calorimeter in the tower, $E_{HAD} \leq 6.0$ GeV. We also require at this stage a match between the extrapolated CTCS track and the CMU stub(δX) in the $R - \phi$ plane of 10 cm or less. The δX requirement was used earlier in the creation of the inclusive muon data stream. This selection criteria left 11485 events. Later, a trigger requirement will be imposed to make a determination of the initial data selection acceptance possible. The trigger we used required data from the Central Muon Chamber along with a matching track. Since the required trigger should form a CMUO bank, a CMUO bank was required in the high p_T data selection [29].

This data was then retracked using information from accelerator monitors that gives the beam position in the X-Y plane as a function of the Z position within the ring[30]. The previous tracks are then constrained to come from the beam position. This step increased the effective length of the CTCS track from about 1m to about 1.3 m. To show the effect of the beam constraint, the mass distribution of the final Z° sample is shown as non-beam-

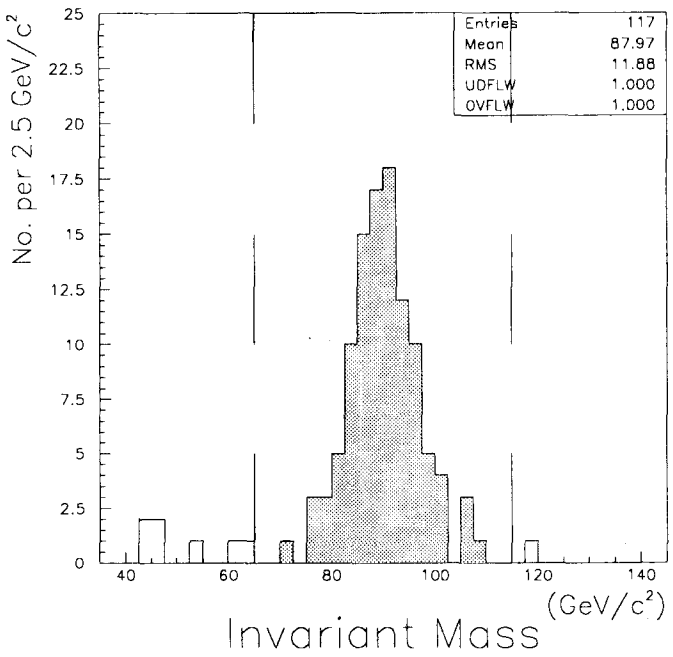

Figure 4.1: Invariant Mass of the Z° sample, without using the beam-constraint.

constrained in figure 4.1 and beam-constrained in figure 4.2. The Z° peak in the beam-constrained events is sharper than in the non-beam-constrained events. Another benefit to the beam-constraint was the elimination of backgrounds to the Z sample. The constraint that the track originate at the beam helps eliminate cosmic ray events and secondary decay products since these tracks do not come from the origin. The elimination of background events is the main reason for using the beam-constraint in this analysis.

4.2 Overall Selection

To create the final Z sample, many general cuts were placed on the events. These cuts were necessary to allow for acceptance, efficiencies, and backgrounds to be understood or

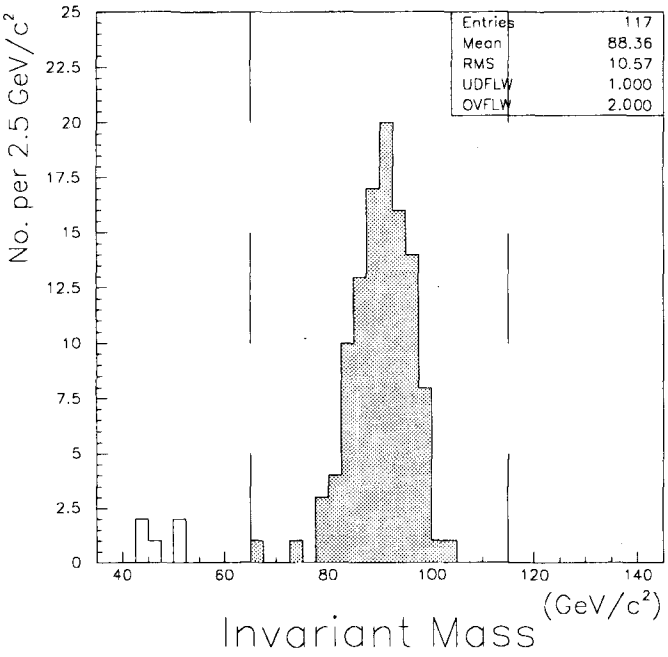

Figure 4.2: Invariant Mass of the Z° sample, using the beam-constraint.

calculated. Several of the requirements below are related to hardware problems that would cause confusion in the understanding of the data selection. These cuts included that the

- Runs with bad data be removed.
- Events flagged as a cosmic ray be removed. This is done with a FORTRAN routine that will be described later in the efficiency and background sections.
- Events with the Z position of the event vertex greater than 60 cm from the detector origin be removed, $|Z_{vtx}| \leq 60.0$ cm.
- All four levels of the muon trigger must be satisfied.
- Events where the L1-L2 muon trigger was in a chamber experiencing hardware problems be removed.

Runs where the muon trigger was not working properly or the calorimeter response was not acting as expected, were not used for this analysis[22]. The integrated luminosity is corrected for these lost runs. While over 4 pb^{-1} of data was collected to tape, this analysis only uses $3.54pb^{-1}$ of the data. Requiring the Z vertex to be within $\pm$ 60 cm of the nominal interaction point keeps the muons centrally located in the detector and retains use of the projective design of the detector. This vertex requirement was treated as part of the acceptance calculation and not as an efficiency. The p_T cut was also handled as part of the acceptance and not as an efficiency. Disallowing the trigger in certain chambers based on hardware problems encountered during the run causes a loss in acceptance for the detector. This loss is dealt with in the acceptance calculation. Cosmic ray removal was done by a FORTRAN program called CMUCOS [31]. The program was slightly over-efficient on real Z^0 events and slightly under-efficient on cosmic rays. The efficiencies and acceptance will be discussed later.

4.3 Muon Selection

After the general event cuts above, requirements on the individual muon candidates are made to reduce background. One of the principle backgrounds to be eliminated comes from punch-through pions. These pions are typically surrounded by many particles that do not reach the muon chambers. For this reason, we define an isolation variable ISO, that looks at the energy deposition around the muon. Since one muon in each Z event can have information from tracking with no information from the CMU system(CMIO banks), there

are different requirements placed on each of the two muons. One set of cuts was called the Silver requirements. The Silver requirements are defined as:

- The presence of a CMUO or CMIO bank with
- $E_{EM} \leq 2$ GeV, Electromagnetic Energy Deposition,
- $E_{HAD} \leq 6$ GeV, Hadronic Energy Deposition,
- non-beam-constrained $p_T \geq 18$ GeV/c,
- beam-constrained $p_T \geq 20$ GeV/c,
- the associated CTCS track attaches to a vertex with a $|Z_{vtx}$ position $| \leq 60$ cm,
- the associated CTCS track passes through outer layer of the CTC,
- the associated CTCS track must pass standard track quality cuts.

A set of tighter cuts were called Gold cuts, were defined as:

- Pass the Silver cuts above,
- It must be a CMUO bank, (there must be information in the CMU detector),
- It must match to an associated CTCS track in the $R - \phi$ plane, $\delta X| \leq 10$ cm,
- The CMUO object must be in the good fiducial volume of the CMU system as defined by the routine FIDCMU [32] [1],

[1]This program is described in Appendix A.

- The muon is isolated in the calorimeter, $ISO \leq 0.1$, where

$$ISO = \frac{\Sigma_{0.4}\mathrm{E_T} - \mathrm{E_T^{\mu}}}{\mathrm{p_T^{\mu}}}$$

  and $\Sigma_{0.4}\mathrm{E_T}$ is the transverse energy in a cone of $\delta R = \sqrt{\delta\phi^2 + \delta\eta^2} < 0.4$ around the muon, $\mathrm{E_T^{\mu}}$ is the transverse energy deposited in the tower traversed by the muon and $\mathrm{p_T^{\mu}}$ is the beam constrained transverse momentum of the muon track.

- The muon stub must not be in the chambers experiencing hardware problems.

4.4 Z° sample

A Z° candidate was any event that passed the global selection of section 4.2 and had one Gold muon and at least one additional Silver muon as defined in the previous section. Since there are several definitions of muons in this analysis, Silver, Gold, CMUO and CMIO, they must be analysed in different ways. To simplify the calculation of the cross section, if the second or Silver muon in a Z° event projects to the CMU fiducial region, it was required to have a muon stub matched to it. There was only one event in the signal region where the second leg projected to the CMU but where a stub was not created. This event was removed from the sample. The mass distribution of these events are shown in figure 4.2. There were 117 Z° events left after the selection process. Last, a cut is made on the invariant mass of the dimuon pair, $65 \leq Mass_{\mu\mu} \leq 115$ GeV/c^2. This window at first glance may seem to very large since the intrinsic width of the Z° is about 2.5 GeV/c^2, but the measured width

including tracking resolution is about 10 GeV/c^2 as can be seen from figure 4.2. Including tracking resolution, the 50 GeV/c^2 window is about 2.5 widths and should contain most of the Z° signal. In this mass region, 65-115 GeV/c^2, there are 108 events. These 108 events compose the Z° data set from which the cross section will be measured.

Chapter 5

Efficiencies

To measure the cross section, the efficiency of the data selection process must be understood. In this chapter, the efficiencies of the cuts imposed to create the final sample of 108 $Z^{\circ} \rightarrow \mu^{+}\mu^{-}$ candidates will be discussed. Data to study the efficiencies came mainly from three sources,

- Cosmic rays taken during special runs,
- muons from J/ψ decays,
- and second muons in Z events.

5.1 Data Sets

The study of efficiencies requires event selection that will not bias the results of the study. To study the efficiency of the several cuts, several basic data sets were created. More specific

cuts were made later depending on the variable being studied. In this section, I will describe the basic cuts on the J/ψ sample, the Z° sample, and the cosmic ray sample. In the following sections, I will only describe the additional cuts made on the basic sample for the various efficiency studies.

5.1.1 J/ψ Data

The J/ψ data was selected from the inclusive muon stream and includes all runs from 18614AA on.

1. Kept events were required to have:
   (a) DIMUON_CENTRAL_3 trigger
   (b) ≥ 2 CMUO banks
2. Cuts applied to every muon in each event:
   (a) Matching in XY plane of ≤ 20.0 cm
   (b) Matching in XY slope of ≤ 1.0 radian
3. All combinations of CMUO objects (after cuts) were checked. An event was kept if at least one combination of two CMUO's were of opposite sign with
   2.7 GeV $\leq$ Invariant Mass $\leq$ 3.5 GeV.
4. Runs with hardware problems removed. Similar to the runs removed in section 4.2.

After this selection, the ψ sample was beam-constrained. The beam constrained data was used in all of the following studies [33].

5.1.2 Cosmic Ray Data

The cosmic ray sample was taken during a special run during June 1989. The requirement on this data was a trigger based on a triple coincidence between the hits in the first two axial layers of the Central Tracking Chamber(CTC) and the Central Drift Tubes(CDT). No Level 1 Trigger was required, but the Level 1 Muon response was recorded. Data was taken with both the 3 GeV and 5 GeV single muon triggers. For data to be accepted and written to tape, the Level 2 and Level 3 trigger requirements must also be met. For this special cosmic run, the Level 2 requirement was a Central Fast track in PT bin 0 (90% efficient at 3.0 GeV/c). Since we are interested in the effects at $p_T \geq 20$ GeV/c, this requirement should not affect us. The Level 3 requirement was a 2.5 GeV/c track found in the Level 3 tracking code. Again we are interested in large p_T tracks so this requirement should have no effect on our measurements [34].

5.1.3 Z Data

The Z sample used to study the efficiencies is the same as that described in the section 4.4.

5.2 Trigger Efficiency - ϵ_T

The first efficiency to be discussed will be that of the muon trigger. This trigger, as discussed earlier, is a four stage trigger and its efficiency was studied 1 stage at a time. The Level 0 efficiency is actually accounted for in the luminosity measurement and so we will start by looking at the Level 1 Muon trigger. There were two different thresholds for the single muon trigger during the 1988-89 run, but for large p_T muons the different thresholds did not affect the final overall efficiency of the trigger.

5.2.1 Level 1 Muon Trigger Efficiency

To measure the L1 muon trigger efficiency for large p_T muons, first a sample of unbiased high p_T muons must be selected. We can get this sample from three different sets of data, we can use *volunteer* muons that have come in on a trigger other than the muon trigger, or we can use the second leg of central-central muon Z's, or finally, we can use muons from cosmic ray data taken during June 1989.

5.2.1.1 Level 1 Efficiency from Volunteers

Volunteer muons after a proper selection, to limit non-muon signals, would be a very good way to study the Level 1 Muon trigger efficiency. Unfortunately, there was only a very small number of large p_T muons. Of 2491 good *volunteer* muons only 13 have a p_T greater than 15 GeV/c. This low number is not unexpected as most of the physics processes that produce

a high p_T muon produce very little else to trigger the event besides the muon. Of these 13 muons, 12 pass the Level 1 Trigger [35].

5.2.1.2 Level 1 Efficiency from Z Data

Another source of unbiased muons, to measure the trigger efficiency, would be the second leg of central-central Z candidates. There are 35 central central Z muon candidates in the final Z sample. If we look at the first leg of each event and it has a muon trigger, we can then look at the second leg to check for trigger efficiency. For events where both legs trigger, we can look at both legs to calculate the trigger efficiency. Thirty of the 35 central central events have triggers on both legs, this gives us 65 muons to study the trigger efficiency. The selection of Z events would would include 1 gold muon, and a second central muon with all of the Gold cuts except the trigger requirement. The results were 60/65 muons have a trigger for an efficiency of $92.3^{+3.3}_{-4.9}\%$.

5.2.1.3 Level 1 Efficiency from Cosmic Rays

Cosmic Ray data gives the best statistics to study the trigger, but have a slightly different timing than $p\bar{p}$ data. Because of this timing difference, the cosmic ray data must then be reconstructed using a slightly different tracking algorithm than what was used on the $p\bar{p}$ data. Another modification to the reconstruction code allowed tracks that were farther away from the beam pipe to be accepted to make CMUO banks. This cut was widened from the 1 cm cut in **PRODUCTION_5_1** code to 10 cm to increase the statistics. There was a concern that loosening this cut would alter the efficiency obtained, but a plot of efficiency

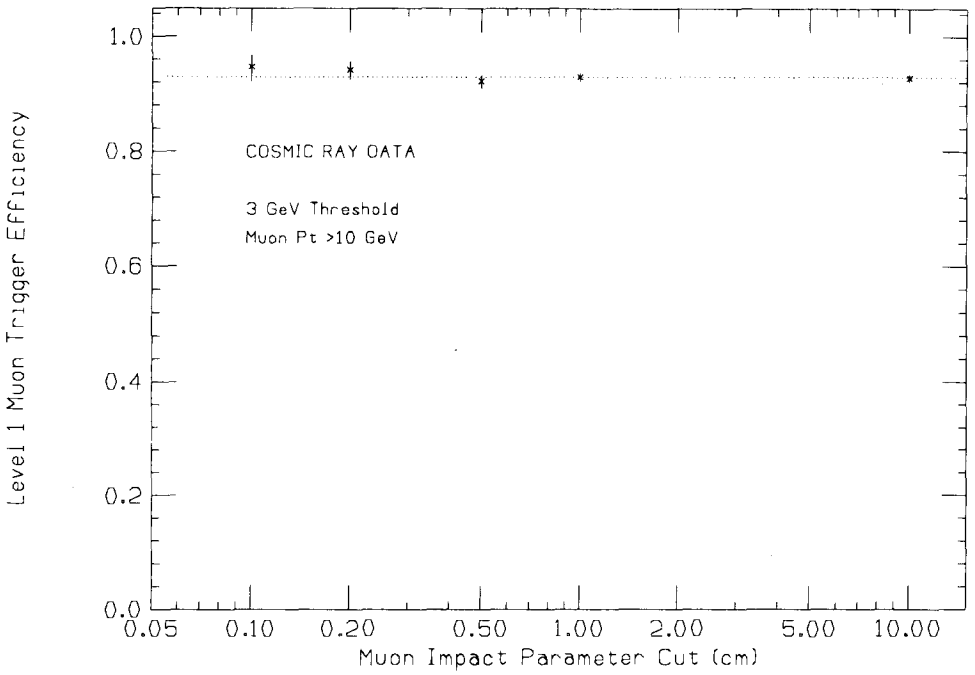

Figure 5.1: Impact parameter dependence on the Level 1 trigger efficiency from cosmic ray data. The data was taken with a 3 GeV/c Level 1 Muon trigger threshold.

versus this variable, called impact parameter (D0) cut shows no dependency of the Level 1 trigger efficiency on this cut. This plot is shown in figure 5.1.

Since cosmic rays are almost exclusively muons, no specific identification type cuts were made on the data. All reconstructed muons were used in this efficiency. For muons with $p_T >$ 15 GeV/c the average efficiency of the Level 1 Muon Trigger was 0.923 ± 0.005. Individual results for data taken with the two thresholds were 0.931 ± 0.007 for the 3 GeV/c threshold and 0.914 ± 0.008 for the 5 GeV/c threshold [35]. The uncertainty is statistical only. A plot of efficiency versus the muon p_T for the combined 3 GeV/c trigger is shown in figure 5.2. A plateau is reached between 10 and 15 GeV/c. Also shown in the plot is the predicted

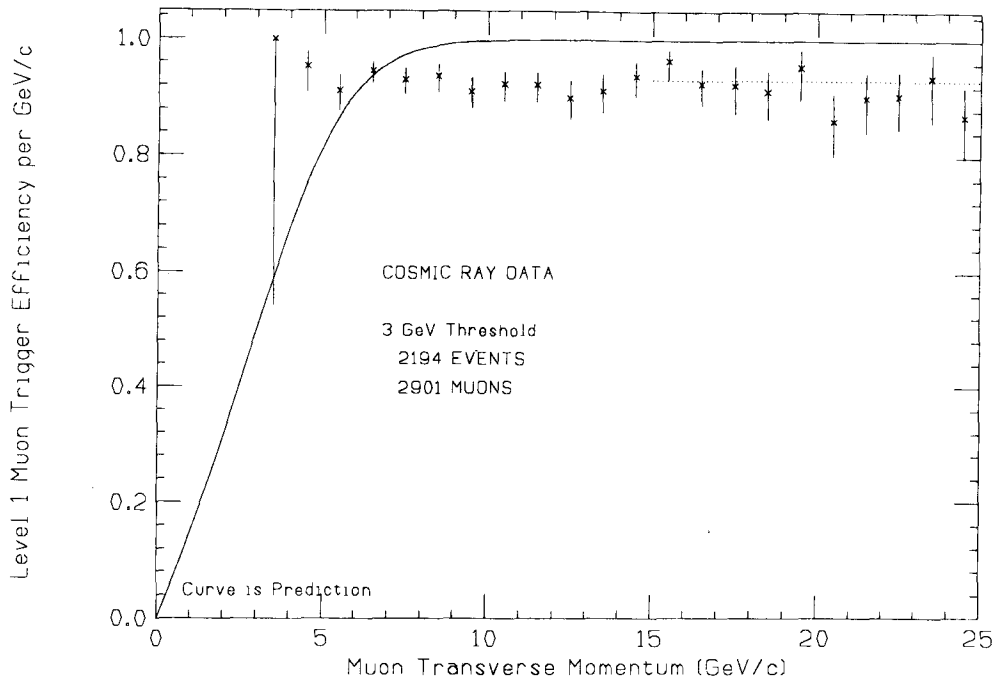

Figure 5.2: Level 1 Muon trigger efficiency for cosmic rays taken with the 3 GeV/c threshold. The dotted line shows the average efficiency (0.931) for muon with $p_T > 15$ GeV/c.

efficiency curve for the 3 GeV/c trigger. The 5 GeV/c trigger while not shown is similar to the 3 GeV/c plot shown in 5.2. Most $p\bar{p}$ data was taken with the 3 GeV/c threshold.

5.2.1.4 Other Effects on L1 Trigger Efficiency

The Level 1 Muon trigger uses timing information to determine a slope of a particle's path through the muon chamber. Since the chamber has edges due its construction, muons coming in near these edges may act differently due to warped field lines. In the actual Z° data sample, a cut was placed to eliminate muons near the edge of the chambers. This requirement actually raises the Level 1 Muon trigger efficiency slightly. In figure 5.3, the efficiency of the L1 trigger is plotted versus the minimum distance from a chamber end in Z. The efficiency rises as we

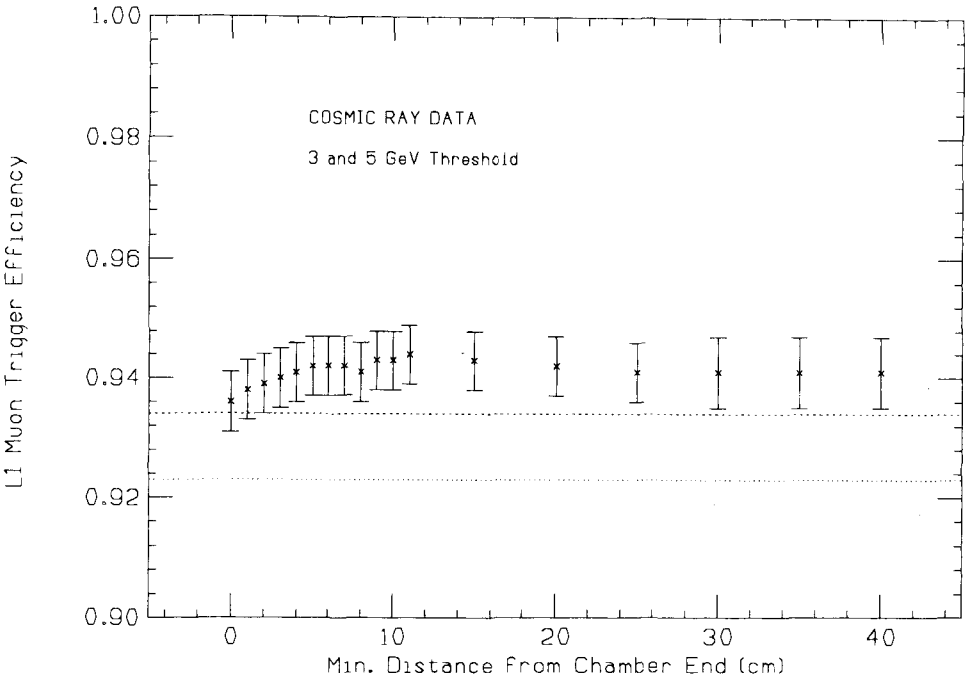

Figure 5.3: Level 1 trigger efficiency as a function of a cut from the end of muon chambers for cosmic rays. The dotted line is the average from cosmic rays without this cut (0.923). The dashed line shows the average of data with the fiducial requirement placed on the muon(0.934). The data in this plot comes from cosmic rays with $p_T > 15$ GeV/c and includes data from both the 3 and 5 Gev/c trigger thresholds.

get farther from the chamber ends. Making a fiducial cut in the cosmic ray sample, the measurement of the Level 1 efficiency is raised to 93.4 $\pm$ 0.5% from 92.3%.

Figure 5.3 shows a plateau in the efficiency at 94%, or 1.7% higher than the value quoted in section 5.2.1.3. The 94% is still above the 93.4% quoted in the the previous paragraph. Since the determination of the Z position requires both channels of the readouts, any event that had overflows were dropped and were not plotted in figure 5.3. These overflows can be caused by knock-on electrons from the walls of the muon chamber, or from leakage from the nearby jets. Leakage should be negligible in this analysis since the muons are usually isolated in Z° decays. From cosmic rays, we find that 4% of the muon candidates have overflows in

the readout, the rate of overflows in $p\bar{p}$ data varies with the cuts applied but varies from 2% to 7%. This could affect our trigger efficiency by a half to one percent, which due to the large statistical uncertainty is negligible. We assign a systematic uncertainty of 0.5% to the trigger efficiency [36].

5.2.1.5 Level 1 Trigger Result

From the above studies we decide to use the results from cosmic ray data and find a Level 1 trigger efficiency of 0.934 $\pm$0.005$\pm$ 0.005 for fiducial muons. We see that the results from Z° data and volunteers are consistent with above result.

5.2.2 Level 2 Muon Trigger Efficiency

The next stage of the trigger efficiency is Level 2. The Level 2 Muon trigger requires a Level 1 Muon trigger and a match to a CFT track. During the 1988-89 run, the CFT requirement for the Level 2 Muon trigger was set to p_T bin 4, which is 90% efficient at 9.2 GeV/c. Since the CFT will behave differently for cosmic rays due to timing, events from $p\bar{p}$ data must be used. Again we need to select an unbiased muon sample, so we use events that were selected by triggers that do not rely on the CFT, mainly jet and photon triggers.

Volunteer events were selected by trigger type. Then, muon identification cuts are used to eliminate backgrounds. The identification cuts include:

- $0.01 < E_{EM} < 0.7$ GeV
- $0.01 < E_{HAD} < 3.1$ GeV

		Total	Level 1 Threshold	
			5 GeV/c	3 GeV/c
	Total Events	67875	13019	54856
Muons[a]	Total	82556	15801	66755
	Isolated[b]	6952	1202	5750
	With Level 1 Trigger	4358	505	3853

[a] Only the highest p_T muon in a wedge is counted.
[b] With the cuts defined by equations 1-4 above.

Table 5.1: Description of Final L2 Volunteer Sample

- Calorimeter Energy in cone of 0.4 around muon < 10.0 GeV
- $|\delta X| < 10$ cm

The calorimeter cuts are quite severe and should yield a relatively clean muon sample. A minimum energy cut was required since a bug in the production code, would sometimes assign a energy deposition of 0.0 GeV to a muon. For these events, the energy cuts would be useless to remove background so all these events were thrown out to minimize the problem this would cause. After the events were selected by the identification cuts above, a Level 1 Muon Trigger was required, since the Level 2 Muon trigger requires a Level 1 muon trigger to fire. This eliminates the effect of the Level 1 Muon Trigger on the Level 2 efficiency and allows us to use one Level 2 Efficiency result for both Level 1 thresholds. The results for these cuts are shown in Table 5.1. There were 4358 muons to study the level 2 efficiency. These events were selected from $2.57 pb^{-1}$ of data.

The analysis consisted of plotting the p_T of passing muons in one histogram, and the p_T of all good muons in the sample. The histograms are then divided bin by bin to get an

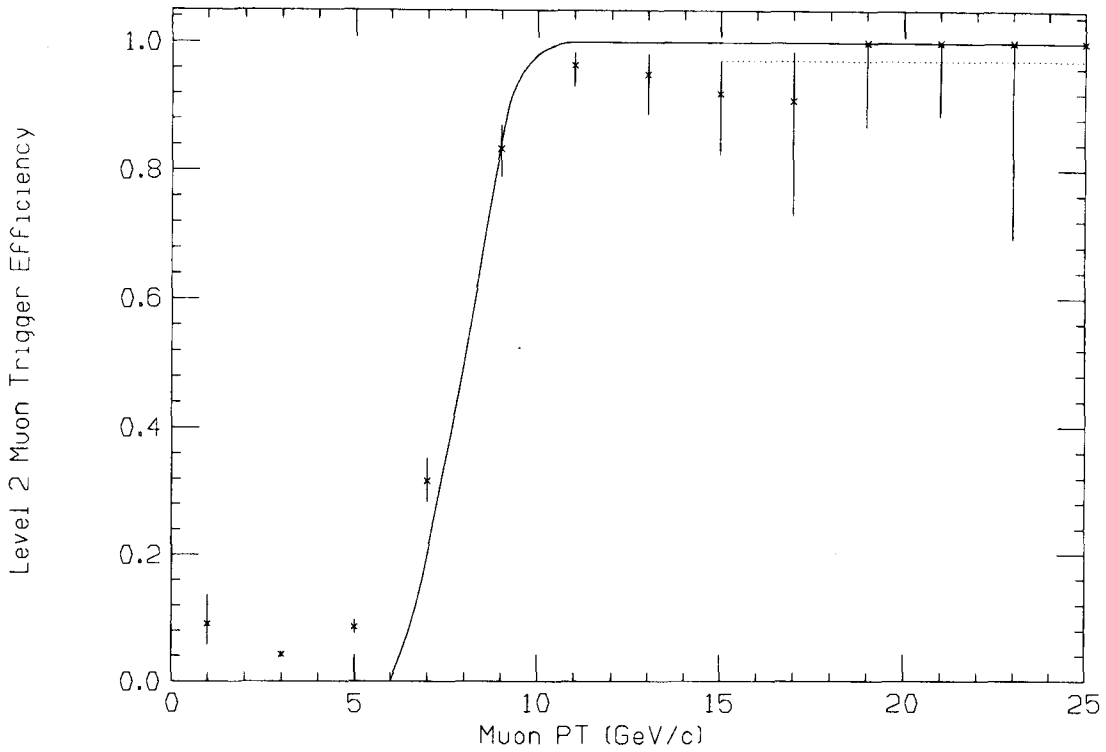

Figure 5.4: Level 2 Muon Trigger efficiency versus muon p_T. The solid curve is the Central Fast Tracker efficiency, while the dotted line is the average efficiency(0.972) for muons with $p_T > 15$ GeV/c.

efficiency as a function of p_T. If two muons pointed to the same wedge only the highest p_T muon was plotted, assuming this should be the muon causing the trigger. The resulting efficiency curve vs p_T is shown in figure 5.4. For muons with $p_T \geq 15$ GeV/c the resulting efficiency was $0.972^{+0.015}_{-0.027}$[24]. The uncertainties are statistical only.

5.2.3 Level 3 Muon Trigger Efficiency

The Level 3 Muon trigger consisted of a FORTRAN program. The program required a match of a DF(Fast two dimensional tracking program) track with p_T above 11 GeV/c. The track had to match in ϕ with a central muon stub. The match requirement was $\pm$ 10 cm around

the central wire position in either of the 2 cells associated with a Level 1 muon trigger tower. If the tower ambiguity was resolvable through charge division, the match was required to be within 10 cm of the actual trigger cell.

At the trigger level a muon stub is just a Level 1 trigger. Another requirement was that the Level 2 muon candidate have a p_T above the Level 2 p_T threshold, CFT bin 4. These two requirements are equivalent to both Level 1 and Level 2 triggers being satisfied.

The data sample used to study Level 3 was the same as that used to study the Level 2 trigger efficiency. Since we want to select events independently of the Level 3 muon trigger, a non muon Level 3 trigger of some sort must be present.

Due to the nature of the Level 3 information kept, Level 3 was only a global 'YES' or 'NO', therefore we can only unambiguously measure the efficiency of the Level 3 Muon trigger for events where there is only one muon. Therefore the data used to study this trigger required:

- One and only one CMUO bank
- Require the wedge with the CMUO bank to have a valid Level 2 Muon Trigger. This insures that the level 2 trigger is associated with the CMUO.
- Only one Level 1 trigger tower present.

Since Level 3 had a implicit requirement for a Level 2 trigger which in turn had an implicit requirement for a Level 1 trigger, the effects of Level 1 and Level 2 are removed by only studying events with a Level 2 trigger.

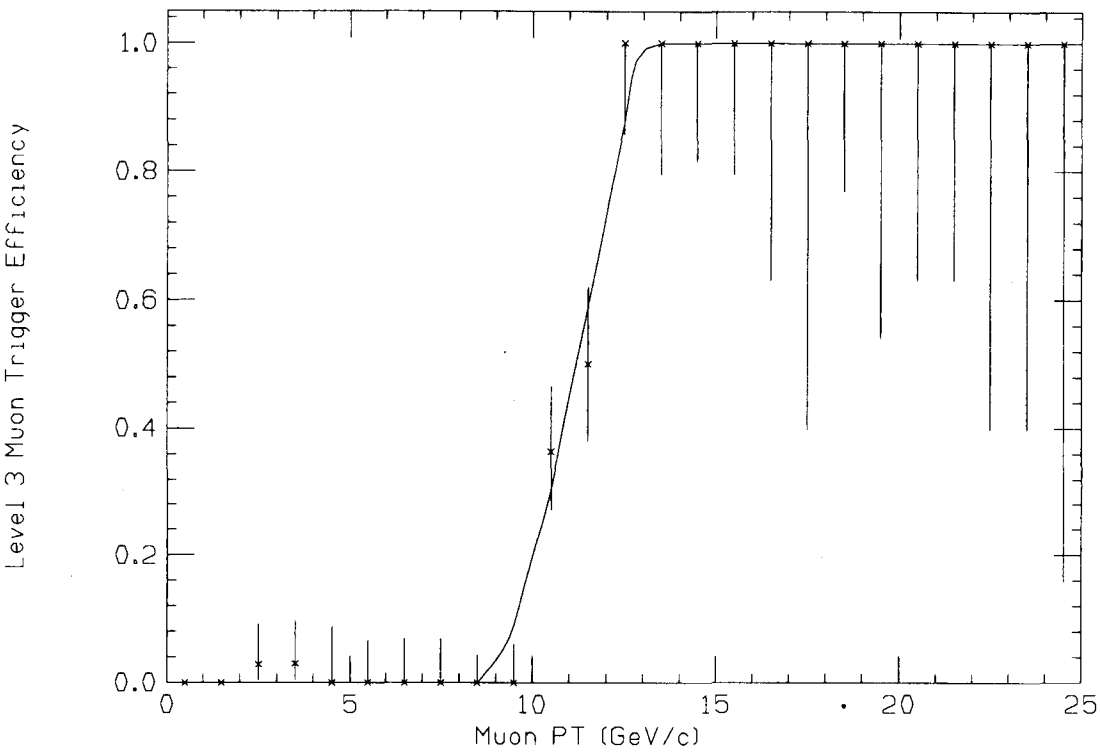

Figure 5.5: Level 3 Muon Trigger efficiency versus muon p_T for the 11 GeV/c threshold. The solid curve is a fit to the histogram. Above 15 GeV/c, Level 3 is 100% efficient.

After all these requirements, there were 389 CMUO events which could be used for determining the Level 3 efficiency. A p_T dependent efficiency was calculated in the same manner as used previously in section 5.2.1. The results of this are shown in figure 5.5. For the 65 muons with $p_T \geq 15$ GeV/c, all 65 pass Level 3 for an efficiency of $1.00^{+0.000}_{-0.028}[25]$. The efficiency of the Level 3 trigger as a function of p_T is shown in Figure 5.5.

5.2.4 Combined Trigger Efficiency

We are most interested in the combined result of the trigger efficiency. To get a Level 3 Trigger, both Level 1 and Level 2 must be satisfied. To set the Level 2 Trigger, the Level

1 trigger must be set. So to get a event wide trigger we need the L1·L2·L3 efficiency. The combined efficiency is L1·L2·L3 = $91^{+1.6}_{-4.1} \pm 0.5\%$. To obtain the uncertainties from the asymmetric uncertainties in each measurement, we added the upper uncertainties in quadrature for the upper bound, and added lower uncertainties in quadrature for the lower bound. While this is not the most correct way to do this, the uncertainties in the total measurement is dominated by the 6.8% uncertainty in the luminosity and the 10% statistical uncertainty on the number of events.

5.3 CTC-CMU Matching Cut Efficiency - $\epsilon_{\delta X}$

In the study of high p_T muons it is useful to check the difference in the $R - \phi$ plane between the stub position measured in the CMU chambers and the extrapolated position of the corresponding CTC track. A cut on this difference is useful in reducing backgrounds from hadronic punchthrough. The matching distribution for muons is expected to be roughly gaussian with a width of $\sigma \approx 12\text{cm}/p_T$. For a 20 GeV/c muon, 10 cm is almost 17 σ. We expect this cut to be almost 100% efficient. Small inefficiencies would be due to events in the tail of the distribution caused by large scatters or by knock-on electrons in the muon chambers. Knock-on electrons could affect the timing information used in the calculation of the stub position measurement. In this analysis, the δX cut is placed at ± 10 cm. This cut is implicit on at least one muon in each event due to the earlier requirements in **PRODUCTION_V5_1** and the Level 3 Muon Trigger.

To study the efficiency of the matching cut, we must look at dimuon events. The reason for needing dimuon events is the matching cut implicit in muon output stream. Two sources of dimuon events are the Z° sample and J/ψ data. We first select Z dimuon events that have passed the requirements: cuts that were imposed in section 4.4. plus the further requirementsthat 2 CMUO banks are present with:

- all Gold cuts present on both legs except the δX cut is not made on the muon being studied, and muons in the bad chambers are allowed if it is not the muon being studied. This should allow us slightly greater statistics, even though we can not use that event in the cross section because the trigger and matching efficiencies are not known.

- The two muons must have opposite charge.

- The invariant mass of the two muon must be near the Z° mass,
  $65.0 \leq \text{Mass}_{\mu\mu} \leq 115.0$ GeV/c^2.

- One muon must have a L1 and L2 trigger associated with it.

There were 35 CMUO-CMUO or Central-Central Z° events. The remaining 73 events are events where only one muon has information in the CMU chambers. These events can not be used to study the δX cut because of the previous matching cut placed on the sample in **PRODUCTION_V5_1**. To study the matching cut, we look at the first muon in the event. If it passes the δX cut imposed in the production code, we go on to look at the second muon's δX value. If both muons pass the 10 cm cut, we can look at both muons in the event. All 70 of the muons in the 35 Z events pass the δX cut. This is an efficiency

of $1.00^{+0.00}_{-0.03}$. If we tighten the trigger requirement, such that the muon being studied must have the L1-L2 muon trigger, we have 65 muons, all of which pass, to study the matching efficiency. The efficiency is unchanged.

Another source of dimuon events would be J/ψ events. J/ψ events were selected by the criteria listed in section 5.1.1 along with the addition requirements:

- Both muons have a Level 1 Muon trigger.
- The muon not being studied must pass the $|\delta X| \leq 10$ cm requirement.
- The muons studied must be oppositely charged.
- The muons must be in the fiducial region of the CMU.
- The muon being studied must not be in bad chambers.
- The muon must have energy deposition in the calorimeters consistent with a minimum ionizing particle.($E_{EM} \leq 2GeV, E_{HAD} \leq 6GeV$)
- The vertex must be within $|Z| < 60$cm.
- The energy in the calorimeter surrounding the muons must be small (< 3 GeV)
- The invariant mass of the pair must be in the range 3.05-3.15 GeV/c^2.

Four distributions from the J/ψ data are shown in figures 5.6-5.9. These distributions are the J/ψ mass, the matching distribution and the p_T distributions for both passing and failing muons. For the J/ψ data, no muon above a p_T of 6 GeV/c failed the 10cm matching

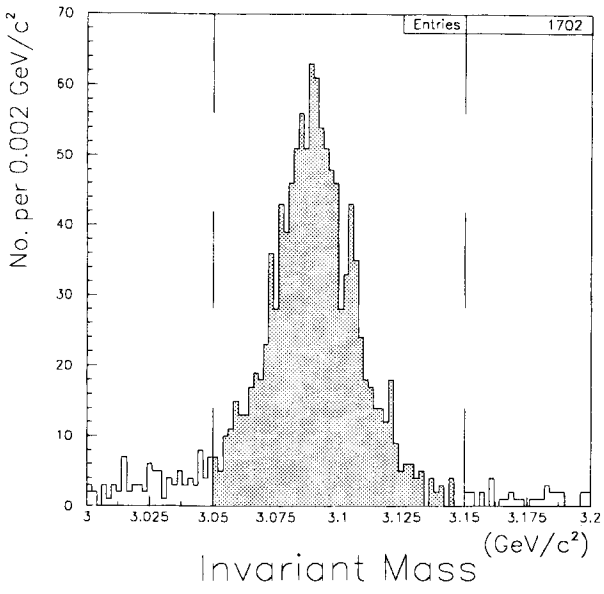

Figure 5.6: Mass Distribution of the J/ψ sample used for the δX efficiency measurement.

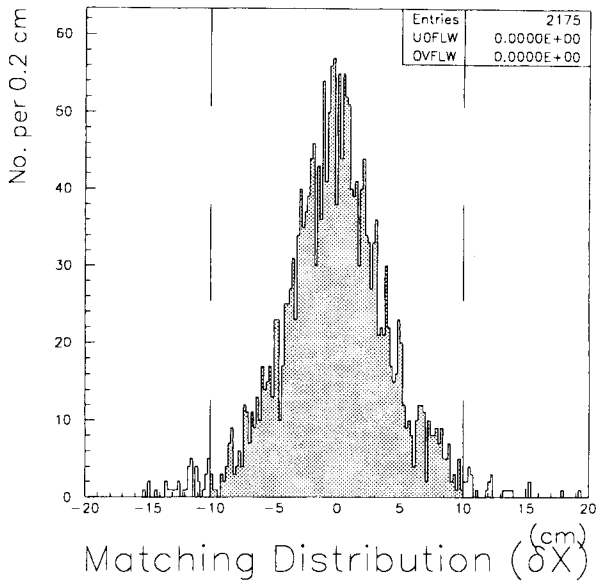

Figure 5.7: Matching Distribution (δX), of J/ψ data. There are 64 events outside of the region of ± 10 cm all with p_T less than 6 GeV/c as seen in figures 5.8 and 5.9.

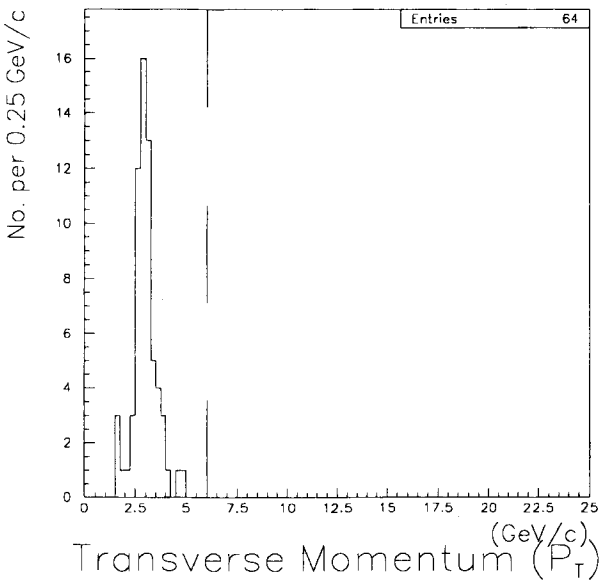

Figure 5.8: p_T Distribution of muons failing δX requirement in the J/ψ sample.

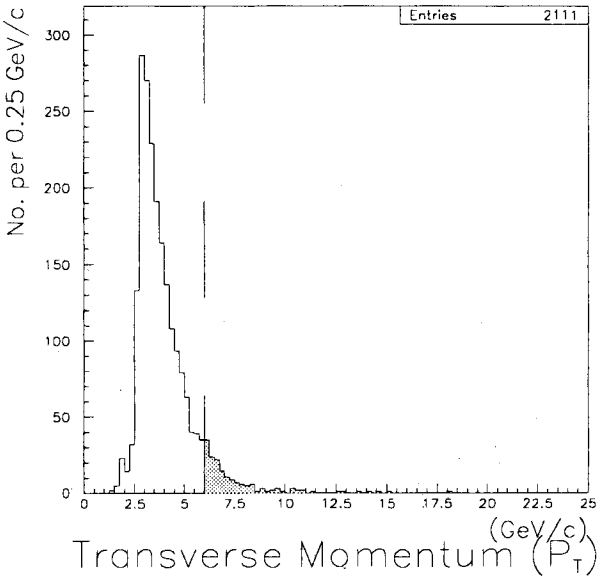

Figure 5.9: p_T Distribution of muons passing δX requirement in the J/ψ sample.

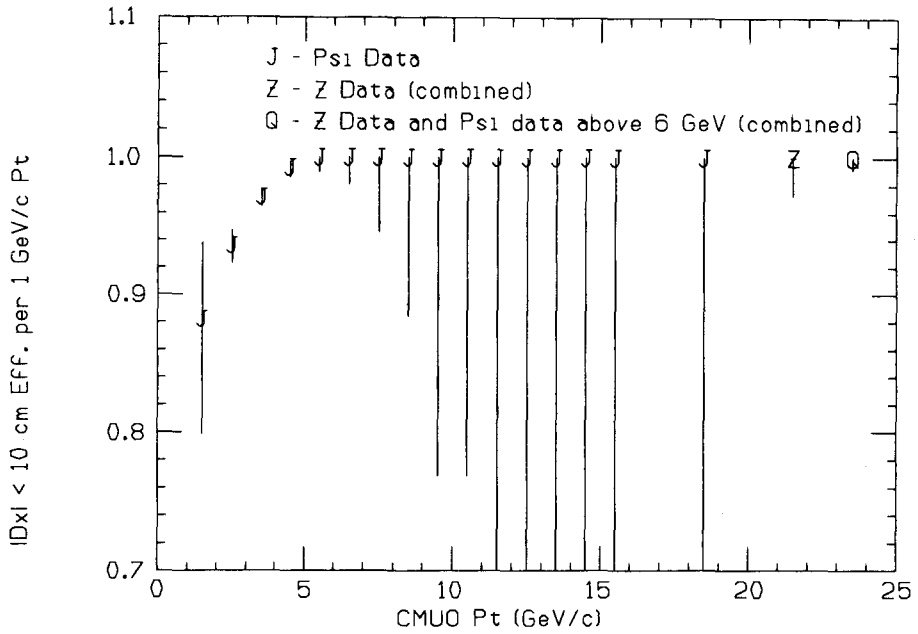

Figure 5.10: A plot of the $|\delta X| \leq 10$ cm cut efficiency for J/ψ and Z° events, as a function of muon p_T. Above 6 GeV/c, the efficiency is flat at 100 %

cut. Combining the J/ψ data above 6 GeV/c with the Z data , we get an efficiency for the matching cut of $1.00^{+0.00}_{0.01}$. It must be noted that there was an initial 20 cm matching cut placed on the two muons in the J/ψ data before the above cuts were made. This is not expected to affect the quoted results, since for muons with p_T above 6 GeV/c there was no data in the 10-20 cm matching region. This 20 cm cut may have some small effect on the matching efficiency for muons with p_T below 6 GeV/c. The efficiency of the 10 cm matching cut as a function of p_T is shown in figure 5.10. This plot also contains an entry for the Z° data and the combined Z° and J/ψ data[37]. The matching distribution for the final Z sample is shown in figure 5.11. This plot would include any events that would have failed the δX cut.

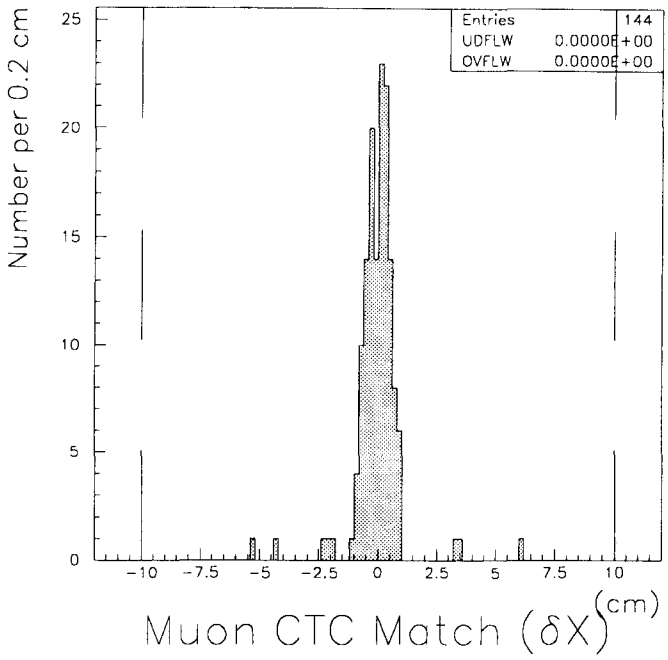

Figure 5.11: A plot of the δX distribution for the Z sample. No events are found that would have failed the δX cut.

5.4 Calorimeter Energy Cut Efficiency - ϵ_{CAL}

The calorimeter energy was a very powerful selection cut. The calorimeter energy cuts allowed for a muon selection, while rejecting a large fraction of background events. The calorimeter energy also allowed us to look for muons in regions where there was no specific muon chambers present, of course in these regions tracking information is very important.

Since the energy deposition of muons in the calorimeter is characteristic of a minimum ionizing particle, making a cut on both the Hadronic and Electromagnetic energy deposition is like cutting on the same quantity twice for real muons. Both cuts still need to be made to eliminate backgrounds to muons, for example, if we only selected on hadronic energy, many electrons would be kept as muons especially in regions where we rely on tracking and the

calorimeter energy without the aid of a muon detector. On the other hand, if we just selected on electromagnetic energy, many pions would be selected. Since both cuts are needed and for real muons the cut is essentially duplicated, the Electromagnetic energy cut and the Hadronic energy cut are made at the same time. These cuts are studied as one cut to try and eliminate correlations.

To measure this efficiency of these cuts, three data samples were used, the cosmic ray sample, the J/ψ data, and the second muon in Z events. Each sample has its problems for this study. The cosmic ray data while all muons, does not have any of the underlying event from the $p\bar{p}$ collisions. The J/ψ data has muons with lower p_T than the 20 GeV/c for muons Z°. The Z° data is limited in statistics.

5.4.1 Calorimeter Efficiency from J/ψ Events

Since J/ψ's can be produced directly or from B decays. The muons from direct production and subsequent decay of the J/ψ will look very similar those from Z°'s except for the muon's momentum. First looking at the J/ψ data, we will make cuts to make the sample as similar to that of the Z° sample. To do this, in addition to the selection in section 5.1.1, we require the following selection criteria:

- Both muons must be CMUO type muons.
- Both muons must have a δX match $\leq$ 10.0 cm
- The vertex of the pair must be with $\pm$60cm of Z=0.

- The two muons must have opposite charges.
- The two muons must be in the good fiducial region of the muon detector.
- The invariant mass of the pair must be in the range 3.0-3.2 GeV/c^2.
- The energy deposition(ENEI) around one of the muons must be $\leq$ 5 GeV.

There were 1448 ψ's passing the above cuts, yielding 2896 muons to study. Figures 5.12-5.15 show four various distributions for the J/ψ data, electromagnetic energy, hadronic energy, hadronic vs electromagnetic energy, and surrounding energy (ENEI) distributions. Of the 2896 muons in this sample, only 37 muons fail the combined Electromagnetc and Hadronic energy cut. This is an efficiency of $0.987^{+0.0023}_{-0.0026}$ [38]. Varying the cut on surrounding energy (ENEI) changes the efficiency slightly, lowering the cut from 5 GeV to 3 GeV raised the efficiency to $0.989^{+0.0021}_{-0.0023}$, while raising the to 7 GeV lowered the efficiency to $0.986^{+0.0020}_{-0.0024}$. Errors are statistical only.

5.4.2 Calorimeter Efficiency from Cosmic Rays

Cosmic ray data was also used to study the calorimeter cut efficiency. Since Cosmic rays are almost exclusively muons, the selection criteria are much simpler than for the J/ψ's. The only cuts made were to keep the cosmic ray data's fiducial region similar to that from $p\bar{p}$ data. These included :

- The Z position of the track be within $\pm$60 cm of Z=0.
- $|\eta|$ of the track $\leq$ 1.1.

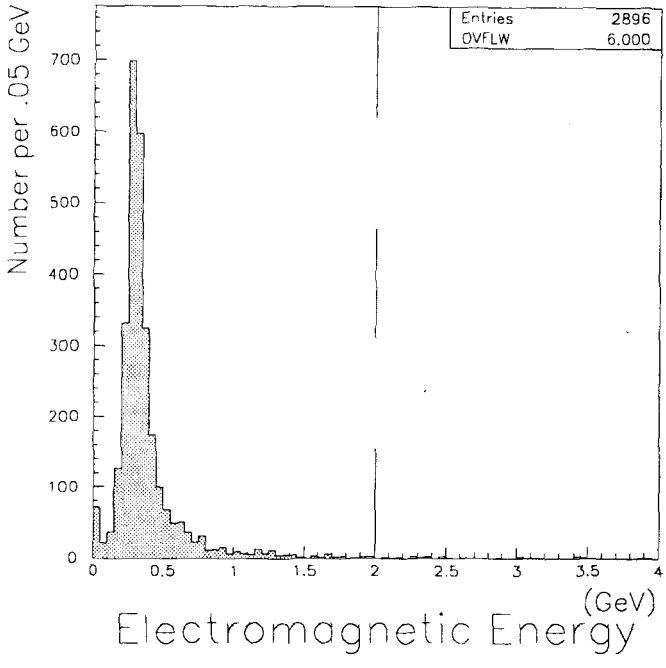

Figure 5.12: Electromagnetic Energy (E_{EM}) distribution of J/ψ events used for calorimeter efficiency study.

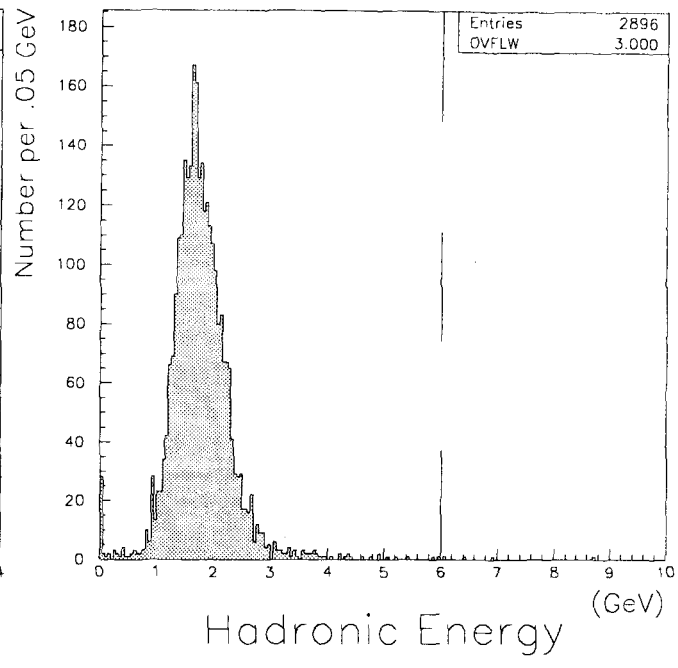

Figure 5.13: Hadronic Energy (E_{HAD}) distribution of J/ψ events used for the calorimeter efficiency study.

- |Impact parameter of the track| $\leq$ 10 cm.

The cosmic ray data was broken into two sets, data that went through the Central Muon systems(CMUO type data) and CMIO type data. Remember, CMIO type data only requires that a track with $p_T \geq 10$ GeV/c to be found. In cosmic rays, the CMIO's are found mostly at higher η because the CMU system covers most of the region at lower η. There were 2944 CMUO type muons and 448 CMIO type muons to study the calorimeter cuts. The CMUO sample had 2904 muons passing the combined calorimeter cuts for an efficiency of 0.986 ± 0.002, while the CMIO efficiency was 441 passing out of the 448 or $0.984^{+0.006}_{-0.008}$. Combining the two results together gives a combined efficiency of 0.986 ± 0.002. The results from the cosmic rays give very good agreement with the J/ψ results. Again errors

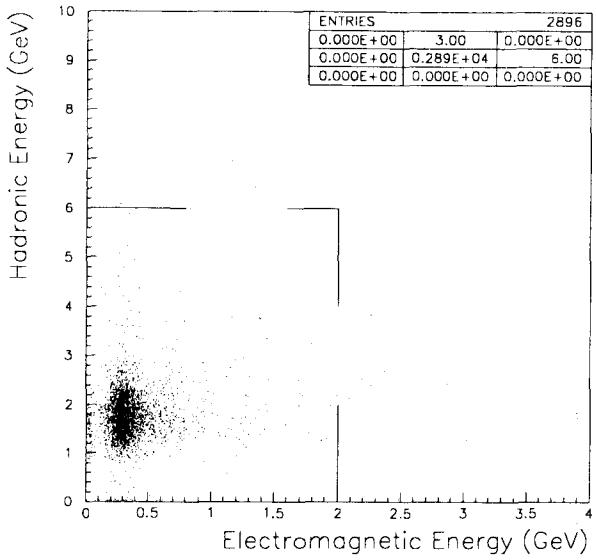

Figure 5.14: Hadronic Energy (E_{HAD}) versus Electromagnetic Energy (E_{EM}) distribution of J/ψ events used for calorimeter efficiency study. The Hadronic energy and Electromagnetic energy tend to clump together in one spot, we do notice that the when one energy deposition is large, the other tends to remain consistent with a minimum ionizing particle.

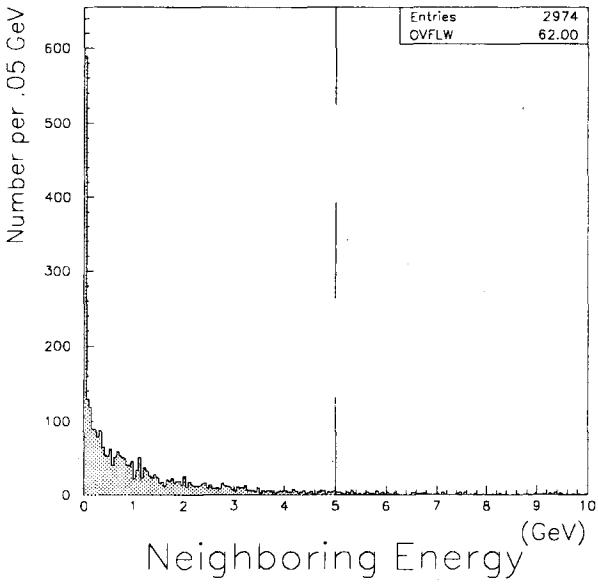

Figure 5.15: Energy surrounding the J/ψ muons in a cone or R = 0.4. We see that an isolation cut at 5 GeV is already fairly far out on the tail of the distribution.

are statistical only. One possible concern about using cosmic rays for the calorimeter cut efficiency is that one leg of the cosmic ray is traversing the calorimeter backwards compared to a muon from real $p\bar{p}$ data. This is not expected to affect the result of the efficiency since the integration time of the calorimeter is long compared to the time of flight. In fact looking at all the cosmic ray data (no cuts), the efficiency of the calorimeter cuts was .986, while looking at cosmics that were in the phi region of π to 2π, also had an efficiency of .986. Another possible problem with using cosmics is the lack of underlying event in the calorimeter. The underlying event has a small effect on this efficiency as can be seen by the variation in the efficiency as the neighboring energy cut was varied. The variation can be seen in figures 5.16 and 5.17. These plots show the normalized distributions of the J/ψ data and the Cosmic ray data superimposed. The peaks of the cosmic ray data are slightly higher than for the ψ data. This difference is small and since the cuts are so loose, the slight shift in the peak has a negligible effect on the efficiency.

5.4.3 Calorimeter Efficiency from Z Data

The Z data was used as a cross check on the J/ψ and Cosmic ray results. The Z sample used for this study is the same as that described in section 4.4. The extra cuts made were:

- First muon must be a CMUO type with
  - $|\delta X| \leq 2$ cm
  - ISO $\leq .1$
  - $E_{EM} \leq 2$ GeV

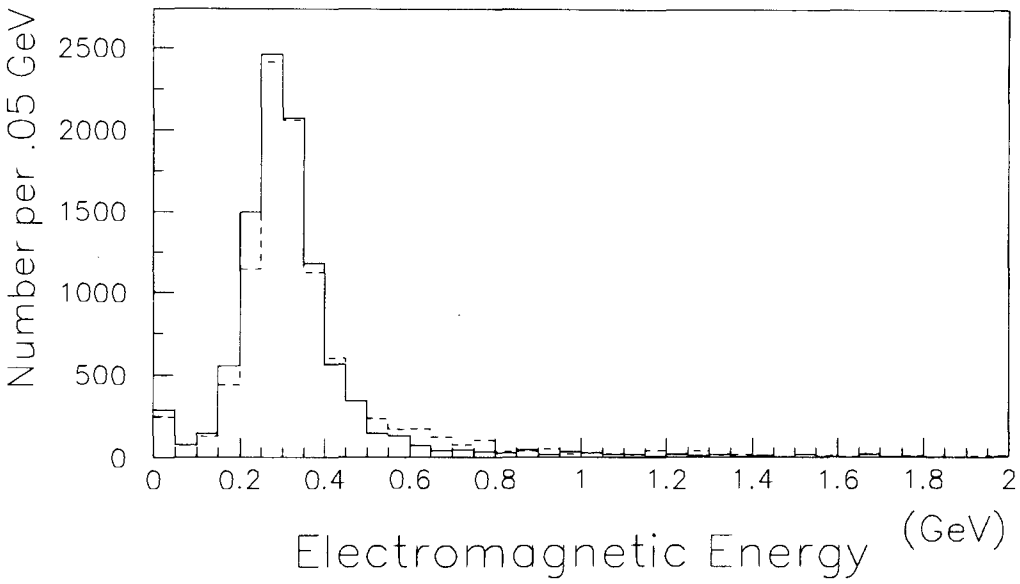

Figure 5.16: The Electromagnetic Energy (E_{EM}) distributions for both cosmic rays and J/ψ data. Cosmic rays are the solid line while the J/ψ data is the dashed line. The two distributions show good agreement.

- $\square$ $E_{HAD} \leq 6$ GeV
- $\square$ Muon be in fiducial region of CMU.

- second muon
  - $\square$ $p_T \geq 20$ GeV/c.
  - $\square$ $|\eta$ of track$| \leq 1.1$
  - $\square$ $ISO \leq .2$
  - $\square$ Opposite charge of the first muon
  - $\square$ have a Z position of track within 6 cm of first muon.

- The pair should have an invariant mass between 75 and 105 GeV/c^2.

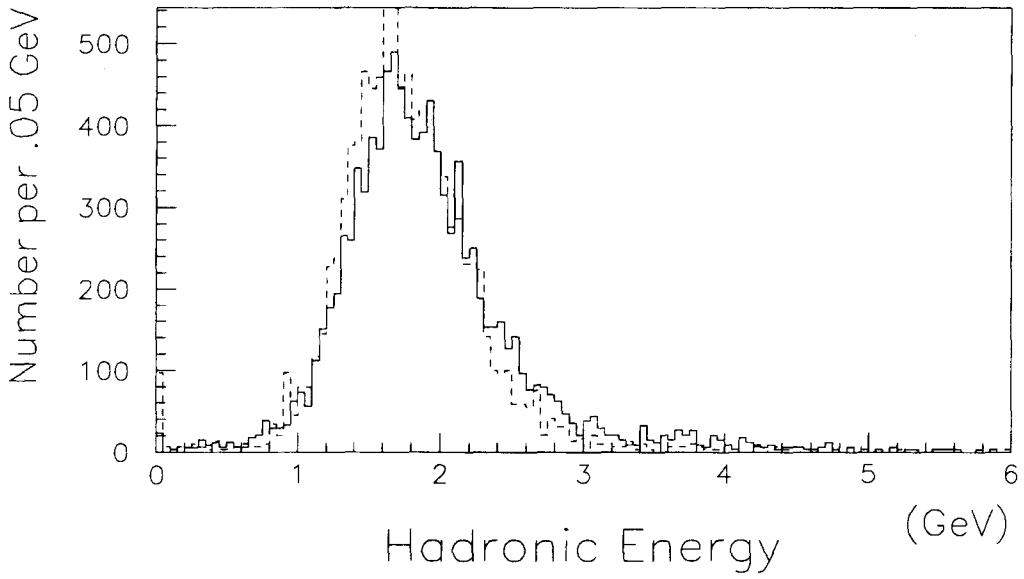

Figure 5.17: The Hadronic Energy (E_{HAD}) distributions for both cosmic rays and J/ψ data. Cosmic rays are the solid line while the J/ψ data is the dashed line. The two distributions show good agreement though peak in the cosmic rays is shifted a little higher. Since the cut is far on the tail of the distribution, this small shift has a negligible effect on the measured efficiency.

- The Vertex of the pair should be within $\pm$60cm of Z=0.

With the above cuts there were 46 CMUO-CMUO type events and 71 CMUO-CMIO type events. Of the 46 CMUO-CMUO type events, 30 events have 2 legs that pass the tight cuts on the first leg. This yields 76 CMUO legs and 71 CMIO legs to look at the calorimeter efficiency. Of the CMUO legs, 73 pass the calorimeter cuts, of the CMIO legs 67 pass the calorimeter cut. This gives a CMUO efficiency of $0.960^{+0.021}_{-0.037}$, a CMIO efficiency of $0.944^{+0.027}_{-0.042}$, and a combined efficiency of $0.952^{+0.017}_{-0.025}$. These efficiencies while lower than the cosmic and J/ψ data results are still consistent with them because of the large statistical uncertainty due to the low statistics in the Z sample.

The electromagnetic and hadronic energy distributions for the Z° sample are shown in figures 5.18 and 5.19. The distributions include all events near the Z° mass that pass all the cuts of sections 4.3 and 4.4 except the minimum ionizing cuts.

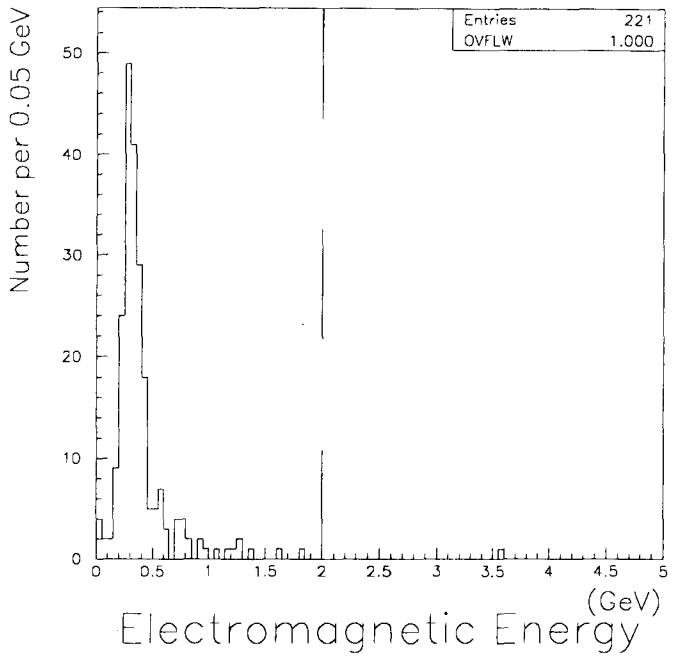

Figure 5.18: Electromagnetic energy distribution for the Z° sample. Included are events that would be in the final sample except that they fail one of the minimum ionizing cuts.

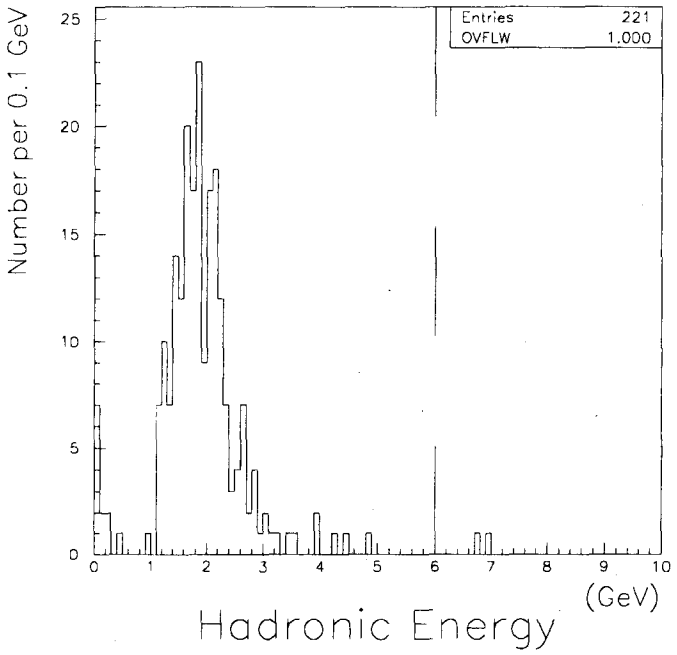

Figure 5.19: Hadronic energy distribution for the Z° sample. Included are events that would be in the final sample except that they fail one of the minimum ionizing cuts.

Data	No. of Muons	No. failed Muons	Efficiency (%)	Error (%)
J/ψ w/ENEI ≤ 3.0	2830	30	98.9	$\pm^{.21}_{.23}$
J/ψ w/ENEI ≤ 5.0	2896	37	98.7	$\pm^{.23}_{.26}$
J/ψ w/ENEI ≤ 7.0	2928	41	98.6	$\pm^{.20}_{.24}$
Cosmic Ray CMUO	2944	40	98.6	$\pm^{0.21}_{0.25}$
Cosmic Ray CMIO	448	7	98.4	$\pm^{0.57}_{0.83}$
Cosmic Ray CMUO+CMIO	3392	47	98.6	$\pm^{0.20}_{0.23}$
Z CMUO	76	3	96.0	$\pm^{2.2}_{3.7}$
Z CMIO	71	4	94.4	$\pm^{2.7}_{4.2}$
Z CMUO+CMIO	147	7	95.2	$\pm^{1.7}_{2.5}$

Table 5.2: Summary of results for $E_{EM} \cdot E_{HAD}$ Cuts

5.4.4 Calorimeter Efficiency Results

The results for the Calorimeter cut efficiency is summarized in Table 5.2. Since within the statistical uncertainties of the measurements all the results agree fairly well, we choose to use the J/ψ results because they have large statistics and come from $p\bar{p}$ data unlike the cosmic rays. The final result for the calorimeter cut efficiency is $0.987 \pm 0.003 \pm 0.002$, where the first error is statistic only and the second is systematic.

5.5 Cosmic Ray Removal-ϵ_{CR}

Cosmic rays were removed from the data sets by the use of a FORTRAN routine that looked for properties associated with a cosmic ray travelling through the detector. These properties include back to back tracksin both η and ϕ, tracks not associated with the primary event vertex, lower occupancy in tracking chambers due to timing, event timing, the particle direction and time of flight.

The algorithm would flag events as a cosmic ray if any of the following were satisfied

- Muon not attached to a vertex, i.e., $|z_{vtx}| > 60$ cm.
- Muon not from a primary vertex, i.e., $|D0| > 0.5$ cm and $\delta z = |z_{vtx} - Z_{track}| > 5$cm.
- Presence of a "bad" track with $p_T > 10$ GeV/c within 2° of back to back in ϕ, where bad means
  - Not a three-dimensional track, or
  - $|D_0| > 0.5$ cm, or $\delta z > 5$cm, or
  - low fraction of possible hits, or
  - too few track segments.
- There is a good track back to back in ϕ, but the tracks are also back to back in η, $(|\eta_\mu + \eta_{track}| < 0.2)$, and the velocity for the track made from these two combined has a velocity greater than 0.5c. This speed is determined from the use of CTC wire timing. A cosmic ray will be one track going from one side of the detector to the other and will give a velocity close to c, while a pair of particles coming from the center will give a velocity of near 0c, since the two particles reach the edge of the detector at about the same time.

The filter may be slightly over efficient at removing events from $p\bar{p}$ interactions. To check this efficiency, we looked at the 4521 events selected with a high p_T central muon candidates. After passing these events through the cosmic filter 129 were identified as coming from cosmic rays, leaving 4392 events.

All 129 of these events were hand scanned and found that 4 muon candidates from $p\bar{p}$ collisions looked consistant with a $p\bar{p}$ interaction. Also in this sample of 129 flagged events were three others that were borderline events, that is, they may be cosmic rays or they maybe from real interactions. From this we gather that in the best case, the cosmic ray filter has an efficiency of 4392/(4392+4) = 99.9%, and in the worst case an efficiency of 4392/(4392+4+3) = 99.8% for keeping $p\bar{p}$ interaction events[31].

5.5.1 Cosmic Ray Background

The filter while very efficient at leaving real interactions in the sample, may be horribly inefficient at removing cosmic rays. To check to see what amount of cosmic ray background remains 1000 of the high p_T muon candidates were handscanned to look for cosmic rays. After going through these 1000 events, 2 events looked like cosmic rays while 3 other events were also identified as possible cosmic rays, but were again borderline cases. We conclude then that the filtered sample contains less than 3/1000 +2/1000 = 0.5% cosmic ray background.

5.6 Tracking Efficiency-ϵ_{TRK}

In **PRODUCTION_V5_1**, the tracking is done by use of two different algorithms to maintain a high efficiency. The first algorithm emphasizes precision, by obtaining the sets of hits that give the best fits. The second algorithm tends to reject kinked tracks and decays in flight. The data was first run through with one set of tracking and then reprocessed using

the second version. Each tracking routine is approximately 99% efficient at finding tracks, so the combined efficiency of the two versions is very close to 100%.

Since this data was retracked to make use of the beam constraint, we retracked using second version of the tracking code because this data was used for the $W^{\pm}$ data sample also, which has a higher background rate than the Z°'s. This retracking results in a small loss of efficiency. We studied this efficiency by looking at tracks in the Z° electron data set. In the electron sample, there were 237 electrons with tracks to study, of these 237 only 3 were lost due to retracking. This gives an efficiency, $\epsilon_{trk} = 0.987 \pm 0.01$ [36].

We also checked to make sure the tracking efficiency was uniform over the acceptance region used in this study. Again electrons from Z°'s were used, this time though no track requirement was made on the second electron. We then looked to see if how often a track was found pointing at the electron calorimeter cluster. The results of this study are shown in Figure 5.20.

5.7 Chamber and Reconstruction Efficiency-ϵ_{CMUO}

There is some small inefficiency in the CMU chamber response and in the pattern recognition code used to form CMUO banks in **PRODUCTION_V5_1**. Since these two efficiencies are somewhat related, we study them together. Also added to this efficiency is a small effect for muons that are predicted to hit the muon chamber in the monte carlo, but actually scatter out in $p\bar{p}$ data.

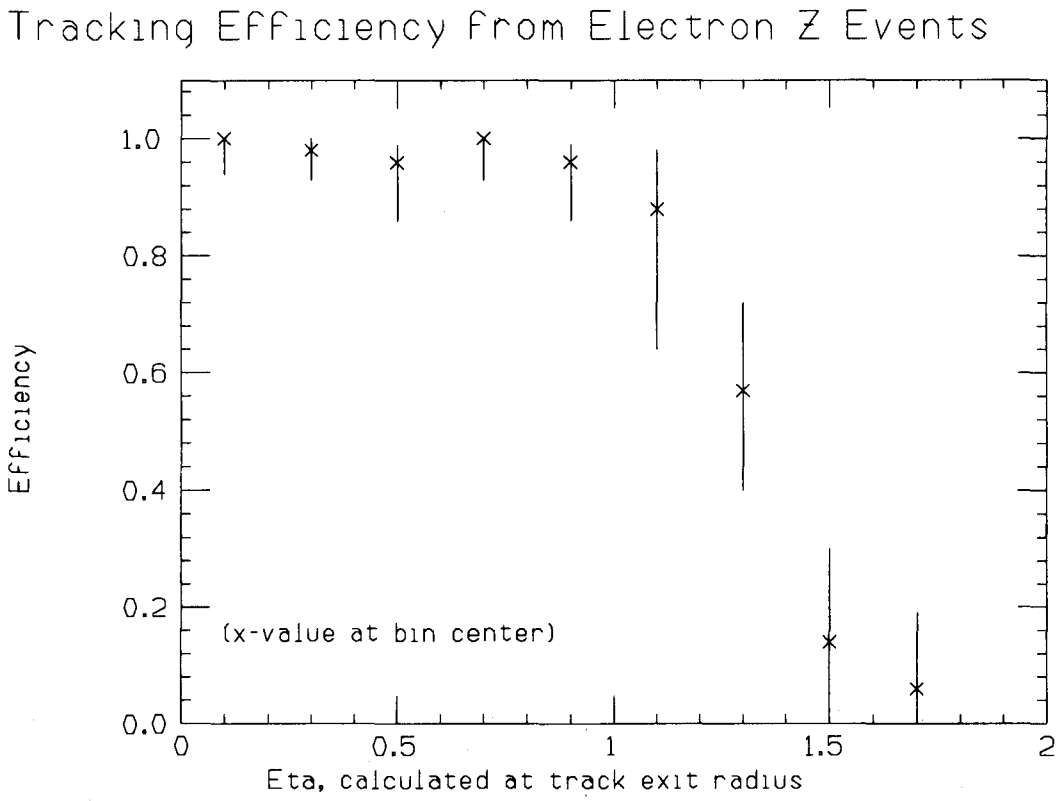

Figure 5.20: Tracking efficiency as a function of exit radius η_e, using the second electron from $Z^\circ \rightarrow e^+e^-$ events.

The individual cells were studied using cosmic rays by means of a test stand in Urbana. In this setup, 3 muon chambers were stacked above each other. The top and bottom chambers were used to detect cosmic rays and predict which towers in the middle chamber should be hit. In this study individual cells were found to be about 99% efficient. Since two cells must be hit for a CMUO bank to be reconstructed, the efficiency would be .99 x.99 = .98, but fortunately the muon system has two chances to fire, because of the double stacked pairs in each tower. This gives an estimated chamber efficiency of 0.98 +(1-0.98)x0.98 = 0.999. While this number is quite high, it may not necessarily describe the efficiency of the chambers in the much noisier environment of the $p\bar{p}$ collider.

The combined efficiency of the reconstruction code, chamber efficiency and scatter out was tested at CDF using cosmic ray data. Using the same 2056 cosmic ray events used in the trigger studies of section 5.2.1.3, we counted the number of cosmic rays that were predicted to hit the CMU chambers but failed to be reconstructed as CMUO data banks. Of the 2056 tracks available for study, 70 were not reconstructed, implying a $\epsilon_{CMUO} = 0.966 \pm 0.004$ These 70 events were than scanned by hand, at most 8 of these 70 events were cases where the muon scattered away from the CMU chambers, the rest were clear cases of the stub failing a quality cut in the reconstruction code.

Unfortunately, timing in cosmic ray events is somewhat different than in $p\bar{p}$ data and it is unclear if the stub reconstruction failure rate is due to this timing difference. For this reason, we decided to use the second leg of Z's to find ϵ_{CMUO}. Looking at the 35 Z° events where both muons extrapolate to the CMU chambers, only 69 are usable to study ϵ_{CMUO}. Of these

69 tracks, only one failed to reconstruct as a CMUO data bank, giving $\epsilon_{CMUO} = 0.99^{+0.01}_{-0.03}$. The one failing track passed through the CMU chambers, hits were present but no CMUO was found. This result is in statistical agreement with the cosmic ray result.

We choose to use the Z result since the only problem with this result is statistical, where the cosmic ray result may have systematic problems from timing differences.

5.8 Isolation Efficiency-ϵ_{ISO}

Isolation, the ratio of transverse energy around the leg of a Z° to the transverse momentum of the muon, was used to eliminate backgrounds to the Z° sample that would have come from jet events. Quarks rarely decay to a single particle, but rather to a multitude of particles or a jet, if one particle in a jet had a large transverse momentum or its p_T was mismeasured, it would not be isolated but would tend to have energy surrounding the track in the calorimeter. To try and remove these events, we select events that have an isolation, $ISO \leq 0.1$ where isolation is defined as the transverse energy in a cone of R = 0.4 around the "muon" less the transverse energy of the muon divided by the "muon's" p_T as measured by the CTC.

To measure the efficiency of this cut, we must use the Z° sample. Cosmic rays are of no use since we are looking for energy due to the underlying event and there is no underlying event in cosmic rays. The J/ψ data is also of little use in determining the efficiency of this cut, since the p_T spectrum of muons from J/ψ decays is vastly different than the spectrum from Z° decays. We can use the Z° sample in two ways to get the efficiency, we can look at the second leg of Z° decays, the second method is to randomly throw cones in the Z° event.

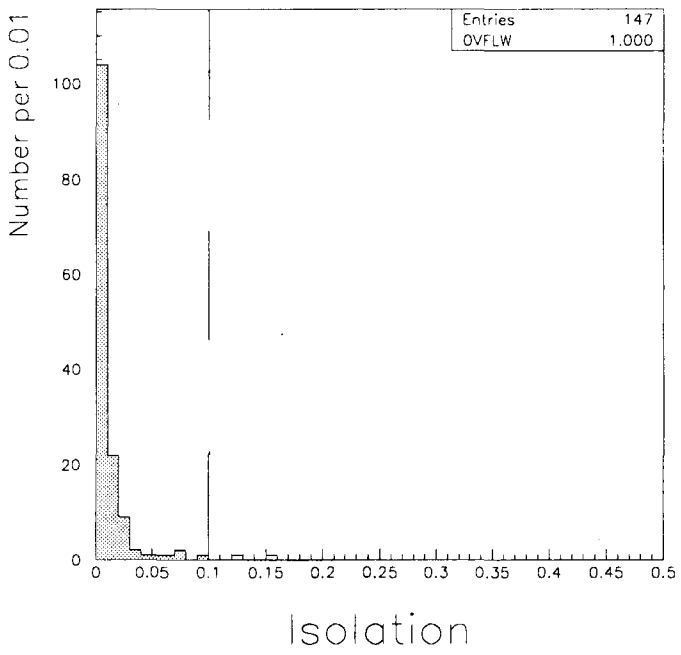

Figure 5.21: Isolation distribution from second legs in Z° events.

If we then divide this energy by the muon p_T, we can use this value of ISO to measure the efficiency of the isolation cut.

From the second leg of Z°'s, there are 139 muons to test the isolation efficiency. Of these 139 muons, 136 pass for an efficiency of $97.8^{+1.2}_{-2.1}\%$. To increase statistics for this measure we take the Z° events and throw 7 cones at the same η as each of the Z° legs but at $\phi = \phi_{mu} + (2\pi/7) + i$, for each i, $1 \leq i \leq 7$. To calculate the isolation, the p_T of the muon at that η is used. We eliminate any cones that overlap a muon. The isolation distribution for the random cones is shown in figure 5.22. The isolation distribution for the second leg of Z°'s is shown in figure 5.21. From this method of throwing cones, we find that there are 1355 cones that do not overlap other muon cones. Of these 1355 random cones, 1318 have an ISO value less than 0.1. The efficiency is $97.3 \pm 0.5\%$.

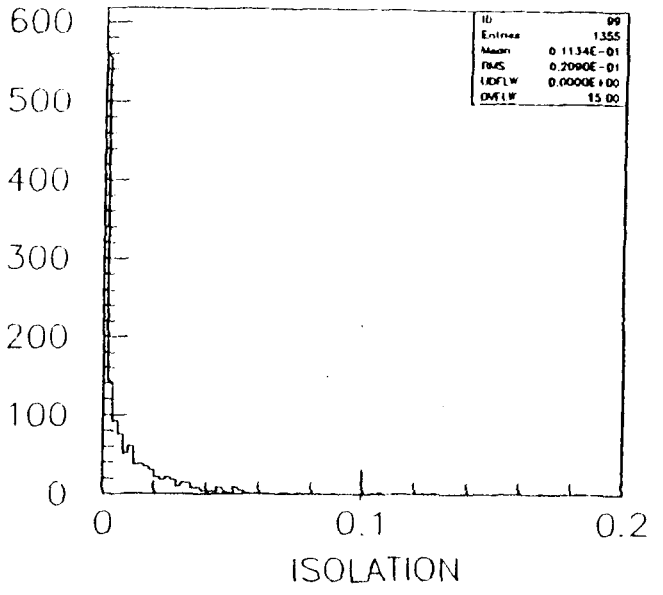

Figure 5.22: Isolation distribution from random cones in Z° events. Energy from cones that overlap the other muon in each event are removed.

Another way of checking this result is to take the a W boson muon sample and take a distribution of energy in a randomly thrown cones and convolute with a p_T spectrum from the Z° data. In figure 5.23, we see the energy spectrum in random cones from both W and Z° data. From this figure, the two spectra look nearly identical. We choose to use a W sample because there are more W events to throw cones. The efficiency measured from the W sample is 98.6% [36]. The slightly higher efficiency is the result of eliminating events that are back to back of the boson p_T. We expect that, opposite the boson p_T, a recoiling jet will be present depositing more energy there than elsewhere.

From these methods, we choose to average these two efficiencies and use half the spread as a systematic uncertainty. The efficiency of the isolation cut is $\epsilon_{ISO} = 98.0 \pm 0.5 \pm 0.6\%$, where the first uncertainty is statistical and the second is systematic.

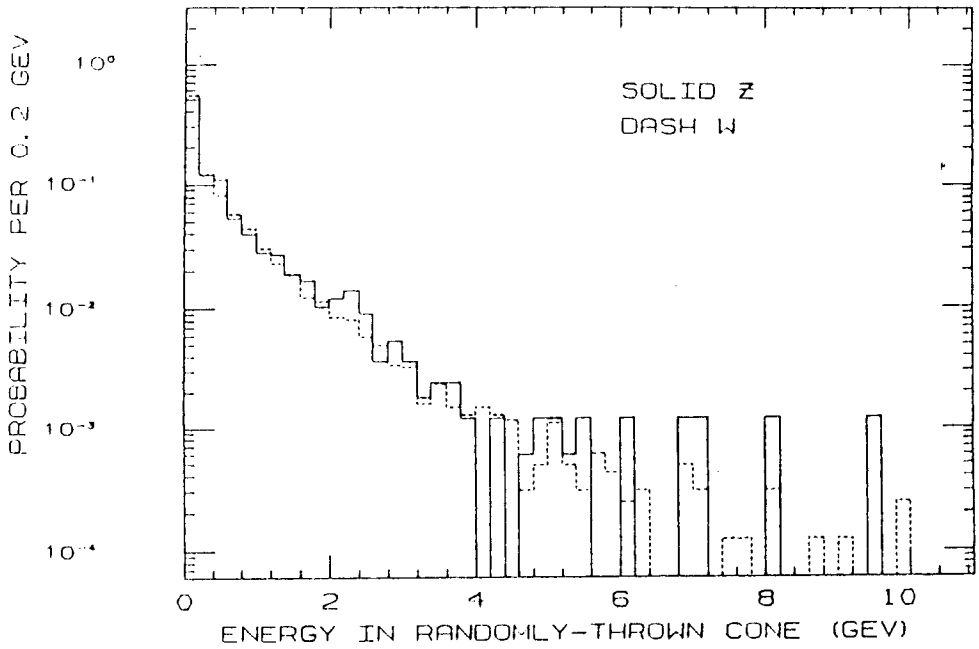

Figure 5.23: Energy spectra from random cones in both W and Z° events. The W spectra was then convoluted with the p_T spectrum of muons from Z° events.

5.9 Correlations

When combining the determining the various efficiencies, care must be taken that correlations between various measurements are not large. We attempted to be minimize correlations by requiring the other selection criteria before the testing the variable being studied. The possible correlations have been studied in reference [39]. This reference is given in Appendix B. The results of this reference are that while slight correlations between variables are present, the effect of taking this correlation into account is nil. The reason for this negligible effect is that most of the cuts are highly efficient to start with. The effect is usually like making a 4 sigma cut becoming a 4.2 sigma cut. Based on [39], we combine efficiencies as if they were uncorrelated.

Cut Description	Measured Efficiency
Minimum Ionizing Calorimeter Cut	$\epsilon_{CAL} = 98.7 \pm 0.3 \pm 0.2\%$
Retracking	$\epsilon_{TRK} = 98.7 \pm 1.0\%$
CTC-CMU Matching	$\epsilon_{\delta X} = 100^{+0.0}_{-1.0}\%$
Isolation	$\epsilon_{ISO} = 98.0 \pm 0.5 \pm 0.6\%$
Muon Reconstruction	$\epsilon_{CMUO} = 99^{+1}_{-3}\%$
Cosmic Ray Removal	$\epsilon_{CR} = 99.9 \pm 0.01 \pm 0.01\%$
Muon Trigger	$\epsilon_{T} = 91^{+1.6}_{-4.1} \pm 0.5\%$
Combined Gold Efficiency	$\epsilon_G = \epsilon_{CAL}\epsilon_{TRK}\epsilon_{\delta X}\epsilon_{ISO}\epsilon_{CMUO} = 94.1^{+1.5}_{-3.5} \pm 0.6\%$
Combined Silver Efficiency	$\epsilon_S = \epsilon_{CAL}\epsilon_{TRK} = 97.4 \pm 0.3 \pm 0.2\%$

Table 5.3: Table showing the various cut efficiencies with their uncertainties. Also listed are the combined efficiencies for Silver and Gold muons.

5.10 Combining the Efficiencies

Once all the efficiencies have been determined, they must now be combined together for Gold and Silver muons. The Gold muon efficiency includes the matching cut, ($\epsilon_{\delta X}$) the isolation cut, (ϵ_{ISO}) the muon reconstruction efficiency, (ϵ_{CMUO}) and the calorimeter cut efficiency, (ϵ_{CAL}). We could also include the trigger efficiency in the total Gold efficiency but choose to leave it separate. The combined Gold efficiency is $\epsilon_G = 94.1^{+1.5}_{-3.5} \pm 0.6\%$, where the first uncertainty is statistical and the second systematic. To obtain the upper asymmetric uncertainties, upper uncertainties were added in quadrature. The Silver efficiency, which only contains the calorimeter efficiency, (ϵ_{CAL}) and the tracking efficiency, (ϵ_{TRK}) is $\epsilon_S = 97.4 \pm 0.3 \pm 0.2\%$. These values as well as the values that go into making them are shown in table 5.3.

Chapter 6

Acceptance

One of the key components to measuring the cross section is determining the acceptance as shown by equation 1.8. The acceptance is defined by the geometry of the detector and the kinematics of the production process. For Z° decays, the kinematics of the decay yield high transverse momentum muons in the central region of the detector. Due to the the monte carlo method of calculating the acceptance, we were forced to move some of selection criteria into the acceptance calculation, namely, the transverse momentum requirements and mass window requirements.

6.1 Monte Carlo Generators

The acceptance is calculated with the use of a monte carlo generator, which simulates the production and subsequent decay of the Z particle into two muons. The muons' trajectories

are then simulated going through the detector and a determination is made as to whether they would be detected by the tracking chamber and/or the muon chambers.

The monte carlo used in this analysis is a fast Leading Order Monte Carlo (LOMC) generator which uses only the tree level diagram $p\bar{p} \rightarrow Z^{\circ} \rightarrow ll$ to create the four vectors of the leptons resulting from the boson decay. The monte carlo uses a relativistic Breit-Wigner for the shape of the Z° mass. The distribution extends to $\pm$ 25 widths around the Z° mass. The generator also includes the polarization effects and the correct matrix elements for the $Z^{\circ} \rightarrow \mu^{+}\mu^{-}$ decays[40]. Not explicitly included, are the Drell-Yan diagrams for $p\bar{p} \rightarrow \gamma \rightarrow ll$. The Drell-Yan decay products can not be distinguished from the Z° decay products and therefore the Drell-Yan diagram will effect our measurement of the cross section. We will discuss the correction for the Drell-Yan contribution later.

6.1.1 Parton Distribution Functions

In using the monte carlo, we must choose a parton distribution function to be used in equation 1.4. The parton distribution function describes the internal quark makeup of the proton and anti-proton, which varies with the Q^2, or energy transfer, of the process The parton distribution functions are created from the results of several experiments. The final results depend on the fitting procedure and the exact data used. We had a choice of several parton distribution functions to use, all of which typically fit the data to a reasonable degree. We chose to use the HMRSB[7] parton distribution functions because it was derived from collider experiments and is widely used. The choice of the HMRSB parton distribution

function allows comparison of this result to other CDF results as well as UA1 and UA2 results. Comparisons of the monte carlo results using HMRSB will be compared to results using other parton distribution functions to determine any systematic uncertainty created by this choice.

6.1.2 Detector Simulation

The detector model used was a simple one. The momentum of muons from the monte carlo generator are used to give the direction and p_T of each muon. In real $p\bar{p}$ interactions, the beam interaction point is centered at Z=0 and is gaussian in shape with a width of 30 cm, thus the generator creates a gaussian distribution in Z with width of 30 cm. Any event with a interaction point greater than $|Z_{vtx}| \geq 60$ cm is dropped as was done in the data to remove cosmic rays.

Since the monte carlo generator we used creates the Z° at rest, we must artificially boost the Z°'s transverse momentum to match the data. The corrected Z° p_T was measured at CDF and the distribution is shown in figure 6.1. To match the measured p_T distribution, the p_T of the muons is boosted using a Z° p_T taken randomly from the distribution. Further corrections to the acceptance for higher-order effects are discussed later.

The monte carlo program generates tracks with a definite momentum whereas the Central Tracking Chamber actually measures the curvature of the track, not the momentum; the curvature measurement has a gaussian distribution. The relationship between muon p_T and the curvature is given by $C = \frac{B \times c}{2 \times 10^9 p_T}$, where p_T is given in GeV/c, B is the magnetic field

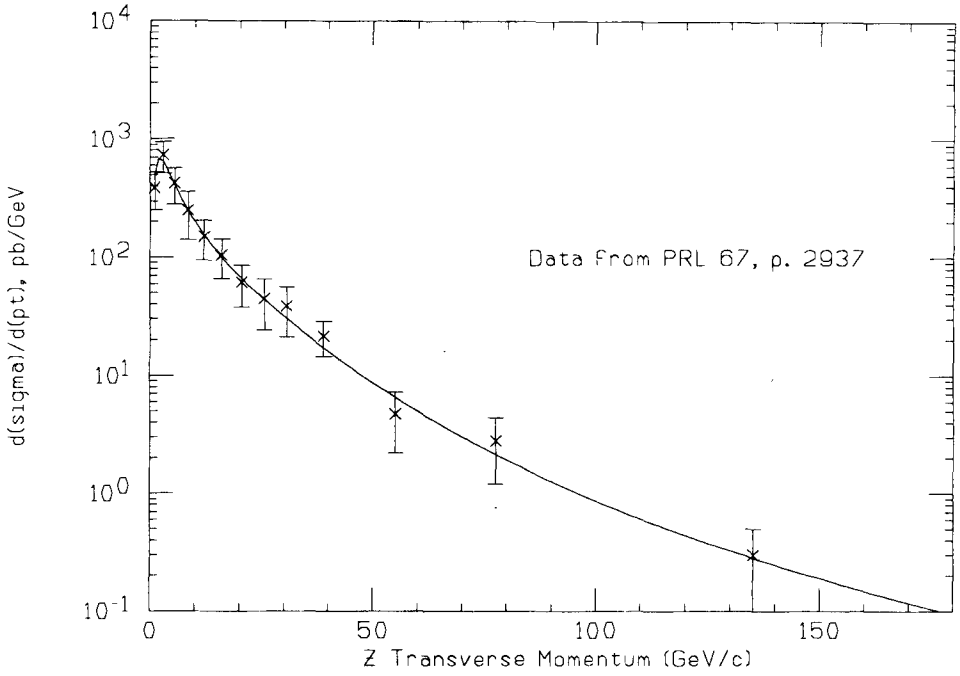

Figure 6.1: The Z° boson p_T spectrum that was used in the monte carlo. Results were taken from CDF $d\sigma/dp_T$ analysis [48].

strength in tesla, c is the speed of light in centimeters/second, the 10^9 is a conversion factor from Gev to eV, and the factor of 2 is a conversion from radius of curvature to curvature, $\rho(cm) = \frac{1}{2C}$. The boosted muon p_T from the Monte Carlo generator is converted to curvature and is then smeared by adding a random value from a gaussian distribution with the observed resolution for the beam constrained data sample, $\sigma_c = 0.0021$ cm^{-1}. We then convert the curvature back to p_T and test for both muons having boosted $p_T \geq 20.0$ GeV/c. Any muon with $p_T < 20.0$ GeV/c is not seen by the rest of the simulation.

We must now count events that are seen by the muon detector or seen just as a track in the Central Tracking Chamber. A complication arises when counting these events, because of the several flavors of Z events. If both decay products are observed in the Central Muon

Chambers, both muons can possibly satisfy a L1·L2 trigger, while if only one muon reaches the muon chambers, there is only one chance for a trigger. These two different topographical events will have different overall detection efficiencies, thus we tally these different type of events separately.

To determine if the particle will be detected by the muon chambers, the leptons are extrapolated using the smeared p_T. We use the smeared pt because this what is used in real data to extrapolate to the muon chambers. Each muon is flagged as to whether it is in the fiducial region of the CMU, in the good region of the CTC or in neither. If both muons are detected, the invariant mass of the pair is calculated, again using the smeared momentum. If the mass does not satisfy $65 \leq M_{\mu\mu} \leq 115$, the event is dropped. This same mass requirement was required of real $p\bar{p}$ data.

After this initial flagging, the Z° event must be counted according to the type of event it is. There are four classes or topologies for Z° events depending how or if the muons are detected. These classes are muon-muon, muon-track-only, muon-unseen, and unseen-unseen or completely undetected. Events where both muons are seen in the muon detector are counted as $N_{m\cdot m}$, and other Z° events where only one muon is seen in the chambers and the other is seen as a track only are counted as $N_{m\cdot t}$. All other types are rejected since they will not show up in the Z° sample. An event with either two tracks or a track-unseen is considered undetected because of the Gold muon selection criteria for actual data. Each event is classified according the fiducial class of the two muons. Table 6.1 shows the Z event classifications.

	muon	track	Unseen
muon	$N_{m\cdot m}$	$N_{m\cdot t}$	rejected
track	$N_{m\cdot t}$	rejected	rejected
Unseen	rejected	rejected	rejected

Table 6.1: A table showing event classifications for Z events. The classification is determined whether the muon propagates to muon chambers or is only seen as a 20 GeV/c track.

We then define the acceptance for each type of Z° event as

$$A_{m\cdot m} = \frac{N_{m\cdot m}}{N_{total}}, \qquad A_{m\cdot t} = \frac{N_{m\cdot t}}{N_{total}},$$

where N_{total} is the total number of events generated. The acceptance as defined here includes the effects of the mass cut, vertex cut, and p_T cut as well as the geometry of the detector. In the data, as well as in the monte carlo, $N_{m\cdot m}$ events comprise approximately 1/3 of the observed Z° sample. The remaining Z events only have one muon seen in the muon chambers. To check if the monte carlo results agreed with the data, the ratio of $N_{m\cdot t}/N_{m\cdot m}$ was plotted in figure 6.2 as a function of an η cut placed on the second muon. The data and monte carlo agree well until $\eta > 1.0$, where the tracking efficiency starts to fall off. The real $p\bar{p}$ data was corrected for detection efficiency. We choose at this point to define

$$A_Z = A_{m\cdot m} + A_{m\cdot t} \qquad f_{mm} = \frac{A_{m\cdot m}}{A_Z},$$

where A_Z is the total acceptance for Z° events and f_{mm} is the fraction where both muons are seen in the muon chambers.

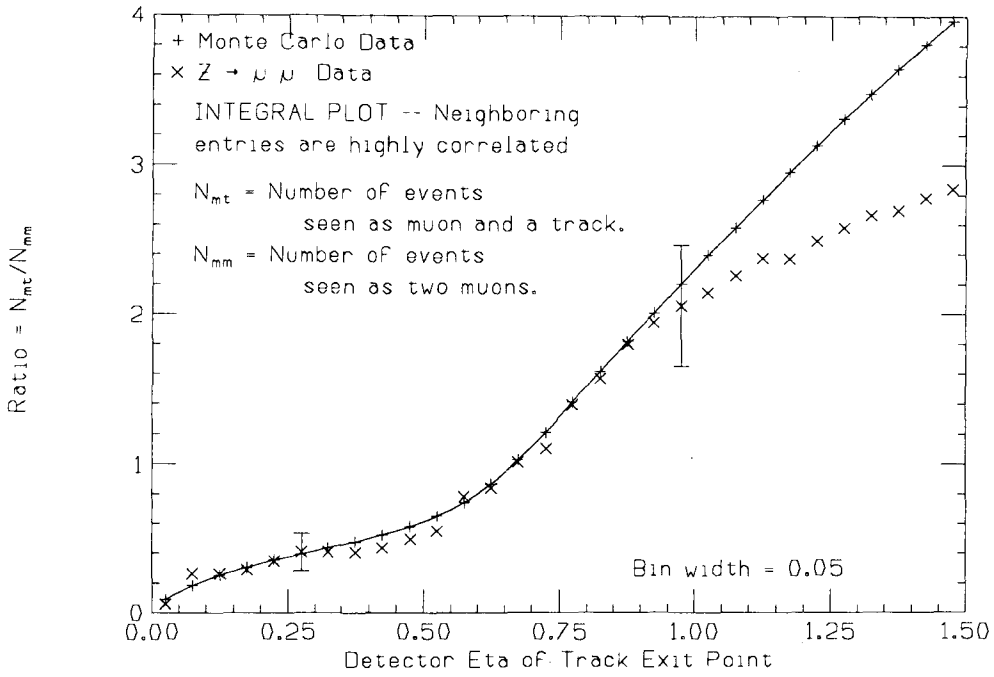

Figure 6.2: A comparison of the $N_{m\cdot t}/A_{m\cdot m}$ for $p\bar{p}$ data and monte carlo results as a function of η cut placed on the second leg. There is good agreement between the two until approximately $\eta = 1$, where tracking inefficiencies become large.

6.2 Higher Order Corrections

What has been used so far to calculate the acceptance has been the zeroth order or Born term of the cross section. It turns out that the Born term alone gives a good approximation of the cross section accurate to within 20 %. The lowest order term does not adequately describe the cross section because it assumes only two particles in the final state and that these two are back to back in the rest frame of the boson. Phase space dictates that there are never any bosons with exactly 0 p_T. This causes a paradox for how can something that never occurs describe the process correctly 80 % of the time.

This paradox is explained by including higher order terms in the cross section. These higher order terms arise from virtual corrections and higher order diagrams where radiated gluons are very soft(little p_T) or are collinear to the leptons. These n-particle states are included because they are indistinguishable from the 2-particle final state. If we now sum over all these diagrams, we obtain a series in powers of $\alpha_s * [\ln(M_W^2/E_{res}^2)]$ which can be rewritten as a multiplicative factor $\exp(-\alpha_s * [\ln(M_W^2/E_{res}^2)])$ to the Born cross section. In these expressions E_{res} is the energy below which the gluons can not be resolved and M_W is the W boson mass. This summation was first done by Sudakov, thus the correction is called the Sudakov form factor. Its use was extended to QCD by Collins, Sen and Soper [41]. We see that if we lower E_{res} to 0, forcing the cross section to the two particle state, the cross section is exponentially damped and there are no bosons with zero p_T. On the other hand if we observe all the bosons regardless of their p_T, we are essentially replacing the E_{res} with

an average p_T of the boson, which is on the order M_W. Therefore, the correction term is small and the Born term alone gives roughly the correct answer.

Including the three particle final states (Next to Leading Order, NLO) diagrams gives the leading contribution to the correction, and is a good approximation to the shape of the boson p_T spectrum for large p_T. This spectrum behaves like a power of $1/p_T$, due to the presence of the boson propagator in the denominator. At low p_T, the Sudakov suppression becomes important and the NLO diagrams no longer give a good estimate of the cross section. To account for the higher terms, we run the zeroth order Monte Carlo and impose the boson p_T spectrum from data. We use the results of this to calculate the acceptance shown in table 6.3. This is a very good approximation for the low Boson p_T [41].

For the higher boson p_T, we use a monte carlo that uses the the Next to Leading Order diagrams. The monte carlo we used was Papageno [42] with 1 Jet. We then determine our acceptance using

$$A = fA0 + (1 - f)A1,$$

where A0 is the acceptance from the zeroth order monte carlo, A1 is the acceptance from Papageno with 1 jet and f is the fraction of our data that comes from bosons with low p_T. To determine f, the boson p_T from data was compared to the Papageno p_T spectrum. The curves were compared to find the p_T beyond which the two spectra have the same shape and f was the fraction of events in the data below that p_T. This technique is valid as long as A0 and A1 are only weakly dependent on p_T. Due to the low statistics in the Z° sample, a sample of W events was used to determine the fraction f. The p_T distributions are shown in

Lower $W - p_T$ cut (GeV/c)	8	10	12	14	16
f (Event Fraction below p_T cut)	0.45	0.55	0.62	0.68	0.73

Table 6.2: Fraction of Events from Leading Order Diagram versus p_T cut.

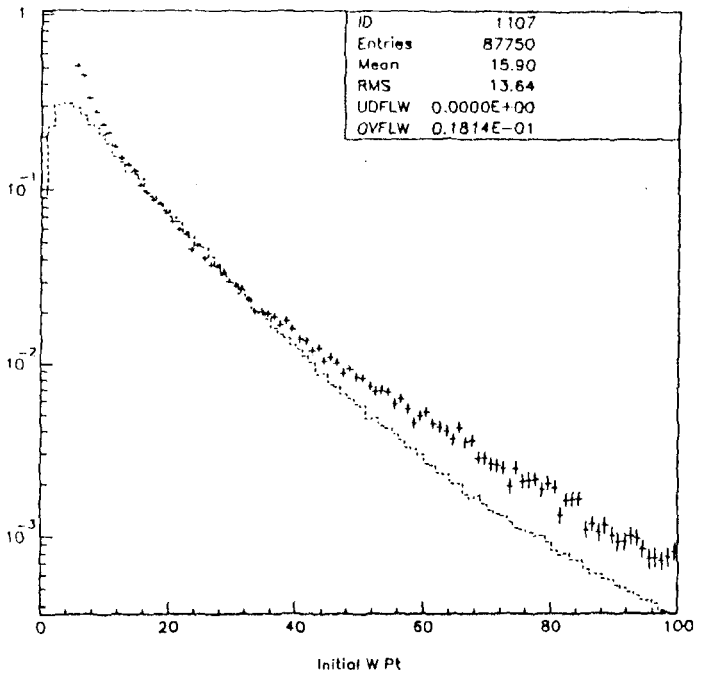

Figure 6.3: The measured W p_T spectrum from [47](dashed) overlaid with the spectrum obtained from the Papageno + 1 Jet monte carlo(crosses). The disagreement above 40 GeV/c is not a concern since there is almost no data in this region causing large statistical uncertainty.

figure 6.3. At very large boson p_T, the statistical uncertainty in the data become large. We thus try to match below the region of p_T = 20 GeV/c. The two curves diverge around a p_T of 12 GeV/c in accordance with the theoretical predictions. We use a value of f = 0.62(p_T = 12 GeV/c) and vary it from 0.55 to 0.80. Different values of f are given for various cuts on the boson p_T in table 6.2 This correction is small (< 1%).

Acceptance Term	Leading Order M.C.	Papageno + 1 Jet	Combined
Total Z Acceptance	14.9 $\pm$0.1%	16.2 $\pm$0.1%	15.40 $\pm$0.1%
f_{mm}	31.0 $\pm$0.2%	31.0 $\pm$0.2%	31.0 $\pm$0.2%

Table 6.3: Acceptance results with statistical uncertainty only

6.2.1 Acceptance Results

The zeroth order monte carlo yields the results in the first column of table 6.3. These numbers include the small corrections to acceptance due to bad chambers. The higher order monte carlo results(Papageno + 1 Jet) are in the second column and the combined result are in the last column. The zeroth order results only include the $p_{T_{boson}} < 12$ GeV/c. The table shows only statistical uncertainty.

6.3 Systematic Studies

The total uncertainty in the acceptance measurement comes from ambiguities in the Monte Carlo inputs. These include

- contributions from Higher Order diagrams,
- parton distribution functions,
- boson p_T spectrum,
- tracking resolution,
- the Drell Yan correction.

6.3.1 Systematics from Higher-Order Diagrams

The correction for higher order diagrams was discussed previously and the results are found in table 6.3. The zeroth order entries are for boson $p_T < 12$ GeV/c, to see the magnitude of the correction we must compare to the zeroth order results using the entire p_T spectrum. These results are for Z° acceptance and muon muon fraction,

$$A_Z = 15.20\%, \qquad f_{mm} = 31.00\%.$$

The higher order diagrams give a systematic shift of 0.2%.

6.3.2 Uncertainty Due to Choice of Parton Distribution Functions

We chose HMRSB parton distribution functions as our nominal choice because they are both understood and widely used. To understand how other choices would affect our results we recalculated the acceptance using five other parton distribution functions. The five sets are DFLM1, DFLM2, DFLM3 [43], MT-B1, MT-B2[44]. The results for these sets and the results for HMRSB are shown in table 6.4. The systematic uncertainty is chosen as half the spread of the results for the five different parton distribution functions.

Parton Distribution	A_Z	f_{mm}
HMRSB	15.2 $\pm$0.1%	31.0 $\pm$0.2%
DFLM1	14.4 $\pm$0.1%	30.8 $\pm$0.2%
DFLM2	14.4 $\pm$0.1%	30.8 $\pm$0.2%
DFLM3	14.3 $\pm$0.1%	30.5 $\pm$0.2%
MT-B1	14.2 $\pm$0.1%	30.7 $\pm$0.2%
MT-B2	13.5 $\pm$0.1%	30.2 $\pm$0.2%
δ_{sf}	0.9 %	0.4 %

Table 6.4: Parton Distribution Function Dependence of Acceptance

6.3.3 Effects of p_T Resolution on Acceptance

The tracking resolution may make a small effect in the acceptance results; the tracking resolution was varied from a width of 0.0011 to 0.0021 cm^{-1} and no effect greater than the statistical uncertainty was seen in the acceptance.

6.3.4 Systematics Due to the Uncertainty in the Standard Model Parameters

The boson polarization and thus the angular distributions of the decay products of the Z° depend on the value of $\sin^2\theta_W$ as seen in equation 1.3. The measured LEP value, $\sin^2\theta_W = 0.2327 \pm 0.00085$ [45], contains effects of higher order radiative corrections and should be suitable for our use. When the original monte carlo was run, an older value, $\sin^2\theta_W = 0.2272 \pm 0.004$ was used. We studied the systematics by replacing $\sin^2\theta_W$ with values of 0.2232 and 0.2336 the extreme range of the two values. The monte carlo results for A_Z change by by 0.20%.

Z Acceptance term	Soft p_T spectrum	Hard p_T spectrum	δ_{p_T} = 1/2 range
A_Z	15.08%	15.44 %	0.18 %
f_{mm}	30.8 %	30.4 %	0.2 %

Table 6.5: Acceptance dependence on boson p_T spectrum and the resulting systematics

6.3.5 Uncertainty Due to Boson-p_T

The W boson p_T spectrum was parameterized in [46, 47] by

$$\frac{d\sigma}{dp_T} = \frac{2p_T(p_T^2 - D)^{(c-1)}}{B[(Ep_T)^F + 1]}$$

where the best fit results were B = 1.434E-04, C =-0.07, D =-50.0, E=0.0342, and F= 3.09. The W boson p_T spectrum is used instead of the Z° spectrum because the spectrum of W's and Z°'s are very similar in shape and the W sample offers higher statistics especially at higher p_T. We found that we could fit a slightly stiffer p_T spectrum and a slightly softer spectrum to the data. These spectra are shown in figure 6.4. The acceptance was then recalculated using the two new spectrum. These results are given in table 6.5, the uncertainty due to the boson p_T is half the range of the hard and soft results, $\delta_{p_T} = 0.18\%$.

6.4 Drell Yan Correction

The monte carlo generator only included the Z° portions of the cross section, since most of the data near the Z° peak is due to the resonance. Unfortunately, there is a small amount of data in mass region studied due to Drell Yan production. In the original monte carlo runs,

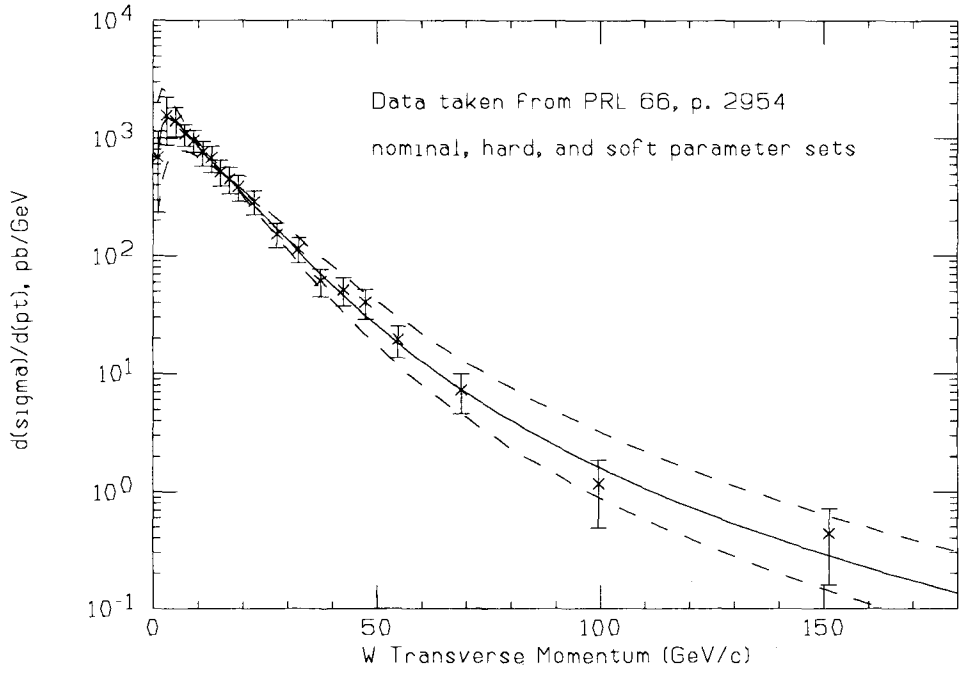

Figure 6.4: The hard and soft parameterizations of the W boson p_T superimposed on the nominal W spectrum. The hard and soft spectrum were used to study systematics due to uncertainities in the boson p_T spectrum.

bosons were created in the region of 26 to 156 GeV/c^2 so that effects of p_T smearing would be understood.

To handle the Drell Yan portion of the cross section, we use the monte carlo to generate the cross section for the Z° terms only and for the complete matrix element with the photon terms. We call this factor

$$DY = \int_{65}^{115} Z^2 dM / \int_{65}^{115} (Z^2 + \gamma Z + \gamma^2) dM = 0.97$$

We use both ISAJET and the fast monte carlo and find this factor to be 0.97. We choose to correct the cross section by multiplying the final result by 0.97. This essentially states that approximately 3 Drell Yan events are seen in the mass region. We will give an uncertainty of 0.01 to this correction factor.

6.5 Final Acceptance and Uncertainties

The final acceptance numbers and the assorted uncertainties are gathered together in table 6.6. The final result is $A_Z = 15.4 \pm 1.0\%$ where the uncertainty is statistical and systematic uncertainty combined. The result for the fraction of events in which both muons are seen in the muon chambers is $f_{mm} = 31.0 \pm 0.5\%$. where the uncertainty is again the combined statistical and systematic uncertainties.

	$A_Z(\%)$	$f_{mm}(\%)$
Systematic uncertainties		
Higher-order Corrections	0.1	0.2
Parton Distribution Functions	0.9	0.4
Boson p_T	0.2	0.2
$sin^2\theta_W$	0.2	0.1
Total Systematic Uncertainty	1.0	0.5
Statistical Uncertainty	0.05	0.2
Total Uncertainty	1.0	0.5
Final Corrected Acceptance	15.40	31.0

Table 6.6: Summary of Acceptance Results.

Chapter 7

Backgrounds

Our observed distribution of events contains both signal events and backgrounds. We devise selection criteria trying to maximize signal events and minimize background events. No attempt to eliminate the backgrounds will be perfect because events on tails of distributions will pass selection cuts and background events may mimic the signal, as such they are indistinguishable from the signal.

Backgrounds to the $Z^\circ \rightarrow \mu^+\mu^-$ signal, will need to have two high p_T muon like objects. Other physics processes that could create two muon like objects are:

- $Z^\circ \rightarrow \tau\tau$ where the τ's decay to muons.
- $W^\pm$ +jet where the jet and $W^\pm$ decay to look like muons
- QCD events that fluctuate to look like two muons
- Cosmic rays that are not filtered out.

Type Of Background	Events
$Z^\circ \rightarrow \tau\tau$	0^{+1}_{-0}
W+jet	0^{+1}_{-0}
QCD	0^{+1}_{-0}
Cosmics	1 ± 1
Total Background (N_B)	1 ± 1

Table 7.1: Summary of Background Results

While we expect each of these backgrounds to be small, each background will be discussed and an estimate of the amount of background given. The backgrounds are summarized in table 7.1.

7.1 $Z^\circ \rightarrow \tau\tau$

Starting with the $Z^\circ \rightarrow \tau\tau$ decay with a subsequent decay to muons, we expect this background to be small for two reasons. The probability of a τ decaying to a muon and two neutrinos is on the order of 17%. For both τ's to decay to muons would be around 3%. If lepton universality holds, there would be approximately 120 $Z^\circ \rightarrow \tau\tau$ events with the τ's in the fiducial region of the CMU. Approximately four of these τ events would have both τ's decay into two muons. The actual number of $Z^\circ \rightarrow \tau\tau$ events we expect as a background would be smaller yet because the kinematics of the final muons is different. Since the Z° has a mass of 91 GeV/c^2, we expect the p_T of the decay products to be approximately 45 GeV/c. For the subsequent decay of a τ to a muon and two neutrinos, we would expect the p_T of the muon to be around 15 GeV/c. While the distribution around 15 GeV/c would

allow some of the events above the 20 GeV/c p_T cut, we would need both τ's to be above 20 GeV/c.

To estimate the background due to $Z^\circ \rightarrow \tau\tau$ decays, we used the ISAJET Monte Carlo to generate $Z^\circ \rightarrow \tau\tau \rightarrow \mu\mu$ events. We then calculated an acceptance, for the $Z^\circ \rightarrow \tau\tau \rightarrow \mu\mu$ events in the similar manner as for A_Z and f_{mm} in section 6.3. The generator created $Z^\circ \rightarrow \tau\tau$ events, the τ's were then allowed to decay into any of the allowed states. The sample was then searched for high p_T objects that would look like muons. Of 4008 generated $Z^\circ \rightarrow \tau\tau$ events, only one could look like a $Z^\circ \rightarrow \mu^+\mu^-$ event in our sample. The acceptance for a $Z^\circ \rightarrow \tau\tau$ event to look like a $Z^\circ \rightarrow \mu^+\mu^-$ event is .025%, compared to a 15% acceptance for real muons. From this we conclude a $Z^\circ \rightarrow \tau\tau$ background of 0^{+1}_{-0} events.

7.2 W+jet and QCD backgrounds

The background from W + jet decays and QCD events are similar. The background from a $W \rightarrow \mu\nu$ decay comes from the recoiling jet fluctuating to look like a sole muon. The QCD background comes from dijet events where both jets fluctuate to look like muons. A jet that fluctuates to look like a single muon would be expected to have large energy deposition around the muon from uncharged particles in the jet. If we look in the data, we see no events with a large energy around the second muon. The jet muon should have a random charge with respect to the muon from the W decay, thus we would expect to see same charge dimuon events. There are no same sign events in the data sample confirming a small background.

Another study was done looking at the high-*pt* data set described in chapter 2. We look for events with one Gold muon and a second CTCS track with $p_T \geq 20.0$ GeV/c that fails the calorimeter cuts, i.e., $E_{EM} > 2$ GeV or $E_{HAD} > 6$ GeV. The idea here is that the second track that fails the minimum ionizing cuts is a pion. We then use the punchthrough probability to estimate how many of these pions could fake a muon. The non-interacting punchthrough probability is less than 1/50 [49, 50]. This selection gives 34 events, 16 of which are opposite charge pairs. Twelve of these 16 events are in the mass region of interest, 65-115 GeV/c^2. If we also require the track to fail the calorimeter cuts by a significant amount say EM energy + Hadronic energy 10 GeV, there are only 8 events in the mass window. Multiplying by the conservative estimate of 1 in 50, we get a background consistent with zero. Therefore we conclude a QCD background of 0^{+1}_{-0} events .

7.3 Cosmic Rays

The cosmic ray background was discussed in section 5.5.1. The result found there was a limit of 0.5% background. For 108 events, this corresponds to a .5 event background. We will be conservative and use a background estimate of $1\pm$ 1 event.

Chapter 8

Results

After having determined all the necessary pieces, all that remains is to actually calculate the cross section. First we must calculate the acceptance times the efficiency for the Z° events of equation 1.8. This calculation is not so simple since there are several topologies to the Z° events. To account for these different topologies two terms are present and they are

$$A \cdot \epsilon = A_Z \cdot f_{mm} \cdot \epsilon_{CMUO} \cdot \epsilon_T(2 - \epsilon_T)\epsilon_G(2\epsilon_S - \epsilon_G) \cdot \epsilon_{CR} \tag{8.1}$$

$$A_Z \cdot (1 - f_{mm} \cdot \epsilon_T \cdot \epsilon_G \cdot \epsilon_S \cdot \epsilon_{CR}) \tag{8.2}$$

The various coefficients and their numerical value are shown in table 8.1. The first term, equation 8.1, counts events where both tracks project to the muon chambers and both have a reconstructed muon found in the chambers(CMUO bank). The second term, 8.2, counts

	$Z^\circ \rightarrow \mu^+\mu^-$
Candidates	108
Background	$B_Z = 1 \pm 1$
Signal	$N_Z = 108 \pm 10 \pm 1$
Acceptance	$A_Z = 15.4 \pm 0.1 \pm 0.9\%$
	$f_{mm} = 31.0 \pm 0.2 \pm 0.5\%$
Gold Muon Efficiency	$\epsilon_G = 94.1^{+1.5}_{-3.5} \pm 0.6\%$
Silver Muon Efficiency	$\epsilon_S = 97.4 \pm 0.3 \pm 0.2\%$
Cosmic Ray Removal	$\epsilon_{CR} = 99.9 \pm 0.01 \pm 0.01\%$
Muon Trigger	$\epsilon_T = 90.8^{+1.6}_{-3.0} \pm 0.5\%$
Reconstruction Efficiency	$\epsilon_{CMUO} = 99^{+1}_{-3}$
Drell Yan correction	$DY = 0.97 \pm 0.01$
Integrated Luminosity	$\int \mathcal{L}dt = 3.54 \pm 0.24 pb^{-1}$
Cross Section	$228 \pm 22 \pm 19 pb$

Table 8.1: Summary of results necessary for the calculation of Z° cross section

events that have one track projecting to the muon chambers and the second track projecting to gaps in the muon coverage.

Combining equations 8.1 and 8.2 with 1.8 we see that the equation for the cross section times branching ratio becomes

$$\sigma \cdot B(Z^\circ \rightarrow \mu^+\mu^-) = \frac{(N_Z - N_B)}{(\epsilon_G \epsilon_{CR} \epsilon_T A_Z)[f_{mm}\epsilon_{CMUO}(2-\epsilon_T)(2\epsilon_S - \epsilon_G) + (1-f_{mm})\epsilon_S] \int \mathcal{L}dt}. \tag{8.3}$$

We must make one last correction for the Drell-Yan contribution. We make this last correction by multiplying equation 8.3 by the correction factor DY of Section 6.4. With the above equation and the results summarized in table 8.1 we can determine the cross section.

We obtain

$$\sigma \cdot B(Z^\circ \rightarrow \mu^+\mu^-) = 228 \pm 22(statistical) \pm 19(systematic) \text{ pb}$$

The systematic uncertainty includes the systematic uncertainty in the acceptance, efficiencies, and integrated luminosity. The largest systematic uncertainty comes from the integrated luminosity.

8.1 Comparison to Theory and Other Measurements

Previous measurements of $\sigma \cdot B$ for Z decays from hadronic production have been primarily at lower energies at CERN. The UA1 collaboration has results for both $\mu^+\mu^-$ and e^+e^- decays. The UA2 collaboration did not have muon coverage, but did have electron data. Assuming lepton universality, $Z \rightarrow ee$ would give results identical as the $\mu\mu$ case. At CDF, the predicted production cross section is larger than at CERN. CDF has previously published results for $\sigma \cdot Z \rightarrow ee$. These results along with the UA1 and UA2 results are given in table 8.2. The $Z^\circ \rightarrow \mu^+\mu^-$ results agree with the $Z^\circ \rightarrow e^+e^-$ results at $\sqrt{s} = 1.8$ TeV.

The theoretical prediction of the Z° cross section from [55] is shown in figure 8.1. Theoretical predictions agree very well with the results of this analysis. The Standard Model is alive and well.

Experiment	Beam Energy $\sqrt{s}$ (GeV)	Results (nb)	Error		Number of Events	Luminosity (pb^{-1})
			Statistical	Systematic		
UA1[51] $\sigma \cdot B^Z_{ee}$	546	0.039	$\pm^{0.033}_{0.020}$	0.004	4	.148
UA1[52] $\sigma \cdot B^Z_{\mu\mu}$	630	0.0586	0.078	0.084	58	4.66
UA2[53] $\sigma \cdot B^Z_{ee}$	630	0.0656	0.004	0.0038	269	13.0
CDF [54] $\sigma \cdot B^Z_{ee}$	1800	0.209	0.013	0.017	243	4.05
CDF $\sigma \cdot B^Z_{uu}$	1800	0.228	0.023	0.019	108	3.54

Table 8.2: Summary of previous results for $\sigma \cdot B^Z$

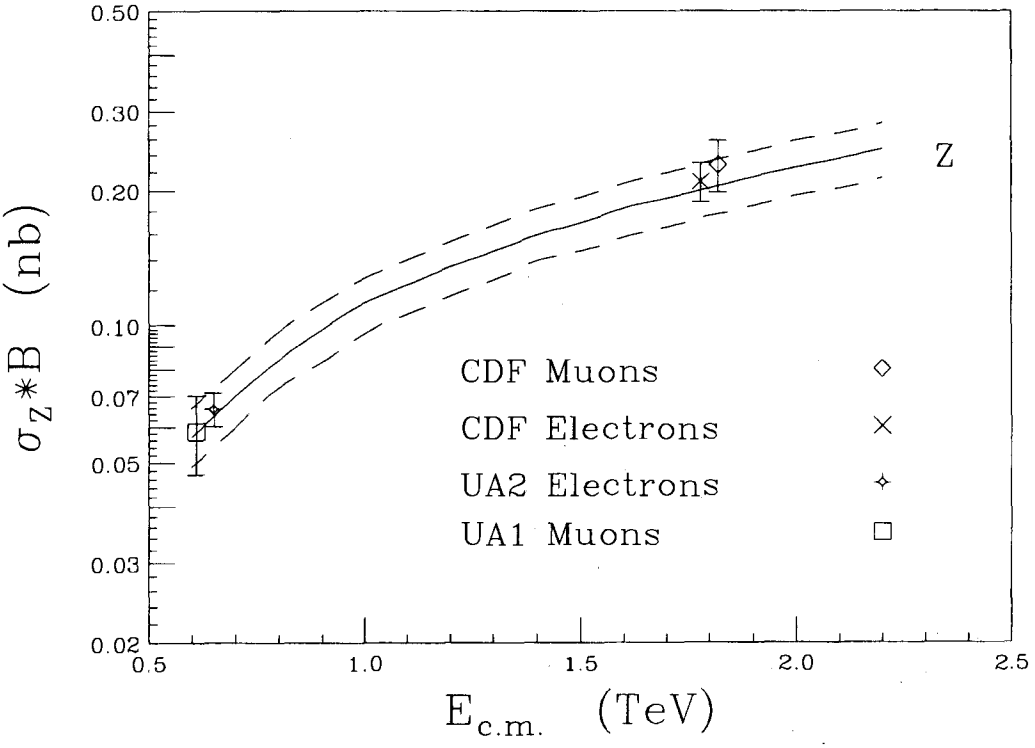

Figure 8.1: The theoretical and experimental results are shown. The dashed lines are the 1 σ limits on the theoretical prediction from [55].

Bibliography

[1] S. Weinberg, Phys. Rev. Lett. **19**, 1264 (1967);

A. Salam, in *Elementary Particle Theory*, edited by N. Svartholm

(Almquist and Wiskell, Stockholm, 1969), p.367;

S. L. Glashow, J. Iliopoulos, and L. Maiani, Phys. Rev. **D 2**, 1285 (1970).

[2] G. Arinson, *et al.*,(UA1 Collaboration), Phys. Lett.,**122B**, 103 (1983).

[3] M. Banner, *et al.*,(UA2 Collaboration), Phys. Lett.,**122B**, 476 (1983).

[4] G. Arinson, *et al.*,(UA1 Collaboration), Phys. Lett.,**126B**, 398 (1983).

[5] P. Bagnaia, *et al.*,(UA2 Collaboration), Phys. Lett.,**129B**, 130 (1983).

[6] G. Altarelli and G. Parisi, Nuclear Physics, **B126**,298(1977).

[7] P.N.Harriman, A.D. Martin, R.G, Roberts, W.J. Stirling, Phys. Rev. D42:798-810 (1990).

[8] F. Abe et al.,Phys. Rev. Lett. **64**,147(1990).

[9] *Review of Particle Properties*, Phys. Rev. **45D**:III, 61-62 (1992).

[10] *Review of Particle Properties*, Phys. Rev. **45D**:II, 1 (1992).

[11] F.Abe, *et al.*, *Nuclear Instuments and Methods in Physics Research*, **A271** 387 (1988).

[12] F.Snider, *et al.*, *Nuclear Instuments and Methods in Physics Research*, **A268**, 75 (1988).

[13] F. Bedeschi, *et al.*, *Nuclear Instuments and Methods in Physics Research*, **A268**, 50 (1988).

[14] L. Balka,*et al.*, *Nuclear Instuments and Methods in Physics Research* **A267**, 272 (1988).

[15] S. Bertolucci,*et al.*, *Nuclear Instuments and Methods in Physics Research* **A267**, 301 (1988).

[16] G. Ascoli, *et al, Nuclear Instuments and Methods in Physics Research* **A268**, 33 (1988).

[17] T.M. Liss, *Luminosity Monitoring and Beam-Beam Counter Performance*, **CDF-552**.

[18] C. Grosso-Pilcher and S. White, *CDF Luminosity Calibration*, **CDF-1202**.

[19] G. Drake *et al., Nuclear Instuments and Methods in Physics Research* **A269**, 68 (1988).

[20] E. Barsotti, *et al., Nuclear Instuments and Methods in Physics Research* **A269**, 82 (1988).

[21] T.K. Westhusing, PhD. Thesis, University of Illinois at Urbana-Champaign, 1989.

[22] A. Gauthier, *Milestones of the Central Muon Trigger*, **CDF-1029**.

[23] G.W. Foster, *et al., Nuclear Instruments and Methods in Physics Research* **A269**, 93 (1988).

[24] A. Gauthier and D. Kardelis, *Efficiency of the Level 2 Central Muon Trigger*, **CDF-1106**.

[25] A. Gauthier, *Efficiency of the Level 3 Central Muon Trigger*, **CDF-1145**.

[26] D. Baden *et al.*, *The V5.1 Production Package*, **CDF-955**.

[27] T.K. Westhusing, *The Central Muon Ananlysis Code*, **CDF-737**.

[28] T. Liss, *GMUFLT: The Muon Filter in Production*, **CDF-1080**.

[29] A. Byon, *et al., A Standard Data Sample for* $W \rightarrow \mu\nu$ *and* $Z^{\circ} \rightarrow \mu^{+}\mu^{-}$ *Analysis*, **CDF-1263**.

[30] R. Swartz and D. Kardelis, *The Making of a Muon Sample*, **CDF-1220**.

[31] D.Smith, *et al.*, *Cosmic Filtering of Central Muon Events*, **CDF-1260**.

[32] R.Swartz, *et al.*, *Fiducial Volume of the Central Muon Chambers*, **CDF-1259**.

[33] T. Rohaly, personal communication.

[34] A. Gauthier, *CTC Tracking Studies with Cosmic Rays*, **CDF-965**.

[35] A. Gauthier, *Efficiency of the Level 1 Central Muon Trigger*, **CDF-937**.

[36] S. Eno *et al., W/Z Cross Sections in the Muon Channel*, **CDF-1349**.

[37] D. Kardelis, *A Study of the CTC-CMU Matching Cut Efficiency for W Muon Analysis*, **CDF-1336**.

[38] D. Kardelis, *Efficiency of the 'Standard' Muon Calorimeter Cuts*, **CDF-1301**.

[39] D. Kardelis, *Correlation Study for the Muon Cuts in the W/Z Cross Section Measurements*, **CDF-1525**.

[40] C. Campagnari, *A Fast W and Z Monte Carlo*, **CDF-1025**

[41] S.Eno, *et al., Update on the Measurement of the W/Z Cross Sections in the Muon Channel*, **CDF-1629**.

[42] I. Hinchcliffe, *The PAPAGENO Partonic Monte Carlo Program*, submitted to Workshop on Physics at Current Accelerators and the Supercollider, Argonne, Il, 2-5 June 1993, LBL-34372.

[43] M.Diemoz, F.Ferroni, E. Longo, G.Martinelli, Z. Phys. **39C**, 21 (1988).

[44] J.G. Morfin and Wu-Ki Tung, Z.Phys. **52C**(1991) 13.

[45] S.L. Lloyd, in proceedings of the Aspen Winter Conference, January 1991. Same values were also presented at Moriond, March 1991.

[46] J.Ng, *A Comparison between the W and Z* p_T *distributions*, **CDF1504**.

[47] F.Abe *et al.*,(CDF Collaboration), Phys. Rev. Lett. **66** (1991) 2951.

[48] F.Abe *et al.*, (CDF Collaboration), Phys. Rev. Lett. **67** (1991) 2937 and Fermilab PUB-91/199-E.

[49] D. Smith and H. Jensen, *Pion Punchthrough Probability in the Central Calorimeter*, **CDF-707**.

[50] B. Denby, *A New Look at Punchthrough*, **CDF-1324**.

[51] G. Ascoli *et. al.*, (UA1 Collaboration), NIM, **A268**, 33 (1988).

[52] C.Aljabar*et al.*,(UA1 Collaboration), Phys. Lett **253B**, 503 (1991).

[53] J.Alitti *et al.*, (UA2 Collaboration), Phys.Lett. **276B** 365 (1992).

[54] F. Abe, *et al.*, (CDF Collaboration), Phys. Rev. **44D** 29 (1991).

[55] G. Altarelli, *et al.*, Z. Phys. C-Particles and Fields, **27**, 617 (1985).

Appendix A

CDF/ANAL/MUON/CDFR/1259
Version 1.0
March 8, 1991

Fiducial Cuts for Central Muons

R. L. Swartz Jr., D. A. Smith

1 Introduction

One of the problems in analysing Central Muon data is calculating and understanding the geometric acceptances involved, necessary for the cross section measurements. This note establishes a set of fiducial cuts for central muons. Two types of muon-candidates are considered: CMUOs, where a stub in the muon chambers is matched to a CTC track, and CMIOs, where no muon chamber requirement is made. CMIO's extend the muon acceptance to the phi-cracks and to the endwall. The cuts ensure that the efficiency within the fiducial region be well understood, while keeping high acceptance. The routine, C$MUO:FIDCMU.CDF makes these fiducial cuts and returns a flag.

2 The Determination of the CMUO Cuts

Distributions taken from the 'M20' sample of high Pt muons were used to determine the fiducial cuts. This sample came from the Chicago spin, using a DFEXPR cut of 20 GeV, as detailed in CDF-795. Then the sample was retracked using Version_4_5 tracking (Berge algorithm) in the Electroweak spin, and again Pt $>$ 20 GeV/c was required, as well as Et $<$ 10 GeV in the muon tower. This procedure is described in CDF-802. Contreras and Westhusing then beam-constrained the fit and made the cuts Pt $>$ 20 GeV/c, EM $<$ 2 GeV, and Had $<$ 6 GeV. However, the definition of the muon tower changed between the two passes. Before this last stage, the definition of the muon tower was changed to the physical tower instead of a cone of 0.13. This change would cause problems for studies depending on the efficiency of the minimum ionizing cut, but does not affect the azimuth and pseudorapidity distributions used to make the fiducial cuts.

	David Smith	Tom Westhusing	Tim Rohaly
ϕ (radians)	0.027 - 0.235	0.026 - 0.236	0.034 - 0.226
modulo 15 °	1.55° - 13.5°	1.49° - 13.52°	2.00° - 13.00°
$\|\eta\|$	0.04- 0.62	0.04 - 0.61	0.04 - 0.62

Table 1: Table 1: CMUO Fiducial Cuts

From the M20 sample, the CMUO vertex and momentum parameters were used to propagate the muon track through the central region out to the CMU chambers. The propagation uses a zero magnetic field in the electromagnetic calorimeter and a -6.6% return field in the adronic calorimeter. The *detector* eta and phi of the extrapolated impact point at the muon chambers was the plotted, and the cuts were chosen at the point where the efficiency of the chambers began to drop off. These plots are reproduced in Figure 1 & 2. Chamber efficiency falls off towards the ends (in eta) of the chambers because the endplates and wire feed-throughs distort the electric field. The edges of the phi-distributions agree well with the known chamber geometry. Tom Westhusing and Tim Rohaly obtained similar results in independent studies. The CMUO fiducial cuts are listed in Table 1. We use the 'Smith' values. Tom's and Tim's numbers are included for comparison. The ϕ cuts are listed in both radians and degrees. Note that the phi cut is done on each wedge, which runs from 0.0° to 15.0°. Also, for the chimney in wedge 29-East, the cut is $\eta < 0.5$.

3 The FIDCMU Routine

The routine FIDCMU takes the track vertex, momentum vector and charge and then uses C$MUO:CMPROP to propagate the muon, in steps, to the radius of the solenoid, through the EM and hadron calorimeters, and on to the CMU chambers. The requisite magnetic field is used for each step, including the -6.6% return field in the HAD calorimeter.

When the propagation is finished, the fiducial cuts are made on the detector coordinates of the *predicted* CMU impact. FIDCMU returns a flag indicating whether the track passes the cuts or, if it didn't pass, the failure mode, i.e., where the track went. A returned value of zero indicates that the muon passed the cuts and is usable. The routine also returns the detector eta and detector phi of the propagated CMU impact position.

4 The Accuracy of the FIDCMU Propagation

Several checks of the accuracy of the FIDCMU propagation vs. the actual hit location in the CMU chambers were made. The hit location is obtained from the CMUS bank. Care must be taken here because the stub positions in the CMUS bank have not been corrected for the survey offsets of the CMU chambers from their nominal positions. This correction is done in CMLNK, during the creation of the CMUO banks. Without the survey corrections a plot of

the difference in z between the propagated impact position and the measured stub position yields a double hump (Figure 3). This results from an offset of 3.66 cm for the positive eta wedges (east) and 2.949 cm for the negative eta wedges (west). This offset does not affect our choice of fiducial cuts because we use the coordinates of the propagated track, and not that of the stub in the chamber, to determine the cuts. In Figures 4&5 we have the difference in centimeters between the propagated CMU impact position and the stub position in z and phi., where in Figure 4 we have the stub position for the z offset. Both plots were fit to a gaussian, and it can be seen that the propagation accuracy has a sigma of 0.81 cm in phi and 2.6 cm in z.

4.1 The effects of multiple scattering

Multiple coulomb interactions randomly deflect muons away from the path predicted by the propagation routine. The four possibilities are:

1. A track extrapolates to the muon chambers, and hits the chambers after scattering;
2. A track extrapolate to the muons chambers, but scatters out;
3. A track extrapolates beyond the chambers edges, and misses the chambers;
4. A track extrapolates beyond the chambers edges, but scatters into the chambers.

Obviously, the tracks that go where they are expected to go (1 & 3) are not a problem. Also, as many tracks will scatter in as scatter out, so that types (2 & 4) should cancel. The problem is that tracks from neither 2 nor 4 will be counted in the data, since (2) fails the fiducial cuts and (4) is not a CMUO. But type (2) will be counted in an acceptance calculation, meaning the fiducial cut introduces an inefficiency, that is, FIDCMU pushes the acceptance slightly high.

Because the fiducial cuts are slightly inside the chambers edges, it works out that even if the track scatters out of the fiducial volume it can still be detected in the chamber, diminishing the undercounting effect of category (2). Geometry implies that the effect affects only $\sim 1/2\%$ of the tracks, as we now describe: in the z-direction a muon chamber is ~ 200 cm long. The stub/track match distribution in the z- direction is a gaussian with $\sigma = 2.6$ cm and a flat tail out to about ± 10 cm. The fiducial cut goes to within 2 cm of the end of the chambers, or about 0.75σ in the z measurement. For a flat rapidity distribution 5/200 of tracks are within 5 cm of the ends of the chambers. Of these, 55% are within 0.75σ track match, and half of the remaining tracks, or 22.5% are scattered away from the chamber edge. So, naively, 1/40 * 0.225 = 0.6% of the muon tracks are susceptible to this effect. A similar argument applies in the ϕ direction.

For the W and Z cross-section measurements have measured the magnitude of this effect (see CDF-1349). Taking $Z \rightarrow \mu\mu$ events where one leg passes tight cuts and the other leg passes loose cuts, we use the second legs for a statistics-limited check on FIDCMU and multiple scattering. From the 69 Z's with both tracks projecting to the muon chambers,

only one track did not make a CMUO bank. This track passed through the good chamber region, but the hits failed a stub quality cut.

Cosmic rays give another check. Beginning with the 2056 cosmic ray events used in the trigger studies (CDF-937), we counted 70 tracks that FIDCMU said should hit the muon chambers but failed to make a CMUO bank. 70 of the 2056 tracks in the sample extrapolated to the chambers but didn't make a valid stub/track match. Of these, all but 8 were cases with hits in the muon chambers but the stubs failed a quality cut in the track/stub matching code. The remaining 8 are category (2) candidates. The effect on the acceptance is therefore less than $8/2056 = 0.4\%$. We found no category (4) candidates.

5 CMIO Fiducial Cuts

Both the $Z \rightarrow \mu\mu$ and $t\bar{t} \rightarrow e\mu X$ analyses, to name two, use muon candidates that miss the muon chambers. Beyond some eta the tracking efficiency and the calorimeter identification of minimum ionizing and/or isolated particles becomes poorly understood. FIDCMU returns a flag indicating whether a track falls within the CMIO fiducial region. This was done in a simple way. The routine calculates the detector eta η_{exit} at the point where the track leaves the CTC volume. If $|\eta_{exit}| < 1.0$ and the track doesn't hit the CMUO fiducial region, the muon will be flagged with a value from 1 to 5, corresponding to phi cracks, 90 degree crack, etc. $|\eta_{exit}| < 1.0$ corresponds to a track passing through all superlayers in the CTC. A track leaving the CTC outside this range will be flagged with a value of 6, indicating that it is not usable.

The reason that the eta cut was made at a detector eta of 1.0 can be seen in Figure 6. This plot measures, for $Z \rightarrow \mu\mu$ events, the ratio of the number of "CMUO-CMUO type" events seen to "CMUO-CMIO type" events for monte carlo and data, as a function of the detector eta cut for CMIOs. In this plot, FIDCMU is the sole determinant of whether a muon, in both data of MC, is a "CMUO-type" or "CMIO-type". It is an integral plot, so adjacent entries are highly correlated. The eta cut of 1.0 is at the point that the data begins to separate from the MC. At a detector eta higher than this, the track leaves the CTC without traversing all of the superlayers, and the track reconstruction efficiency begins to suffer. For this reason the cut is chosen at 1.0, to stay in the efficient region.

6 Conclusions

We have identified the fiducial region of the Central Muon Chambers and have written a routine FIDCMU, which will make these fiducial cuts for both data and monte carlo events.

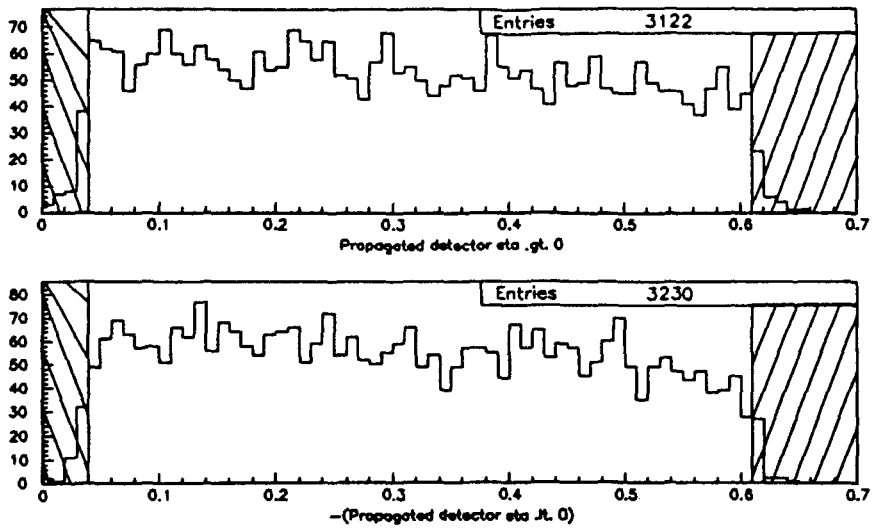

Figure A.1: Detector eta of CMUOs at CMU radius, with cuts shaded

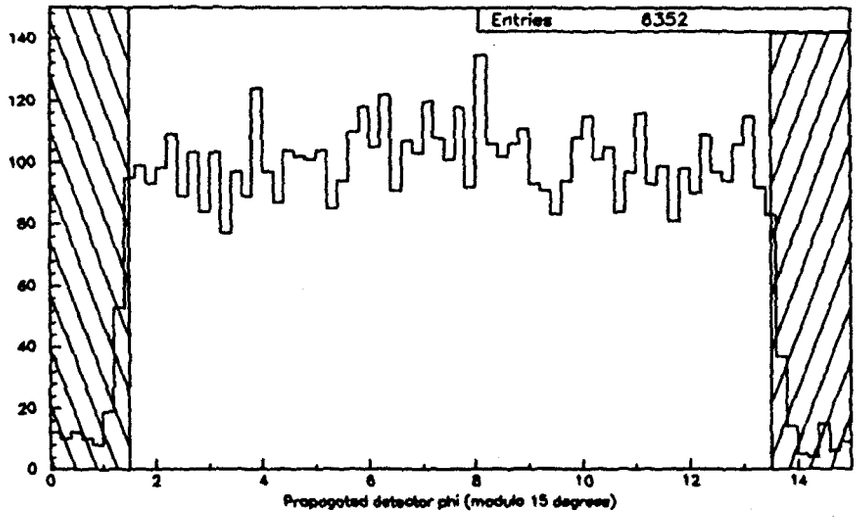

Figure A.2: Detector phi of CMUOs at CMU radius, with cus shaded

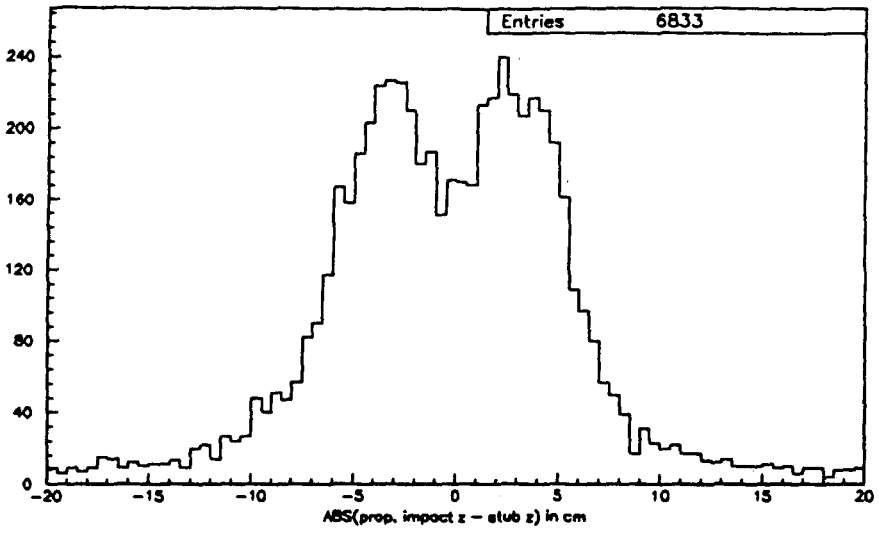

Figure A.3: Dist. from prop. impact to muon stub in z (cm)

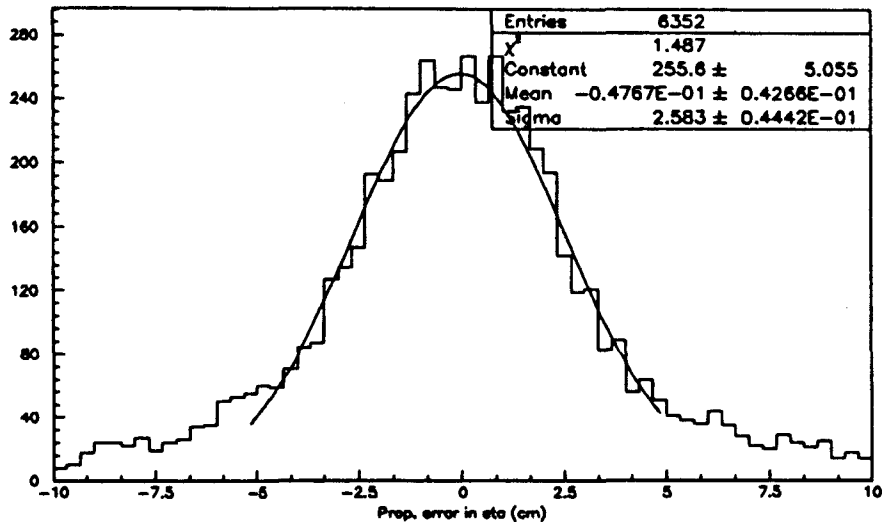

Figure A.4: Corrected propagation error in z (cm).

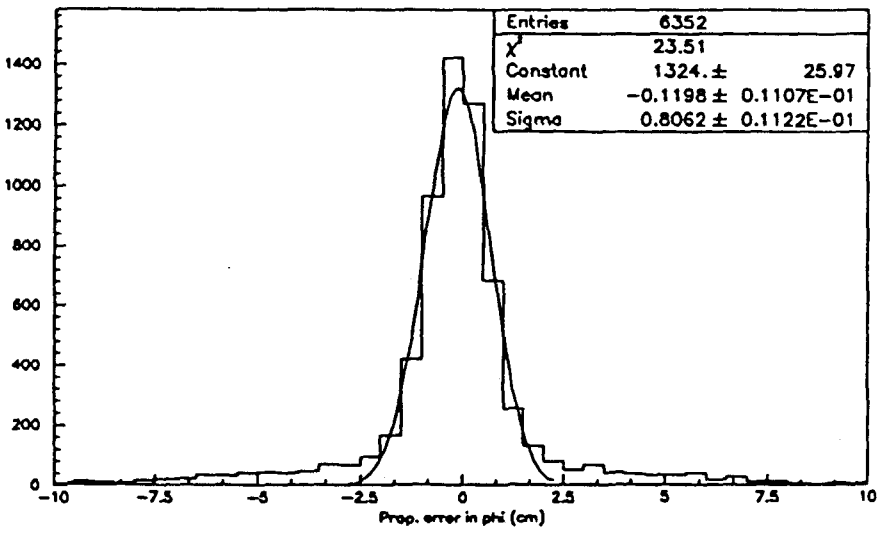

Figure A.5: Propagation error in phi (cm).

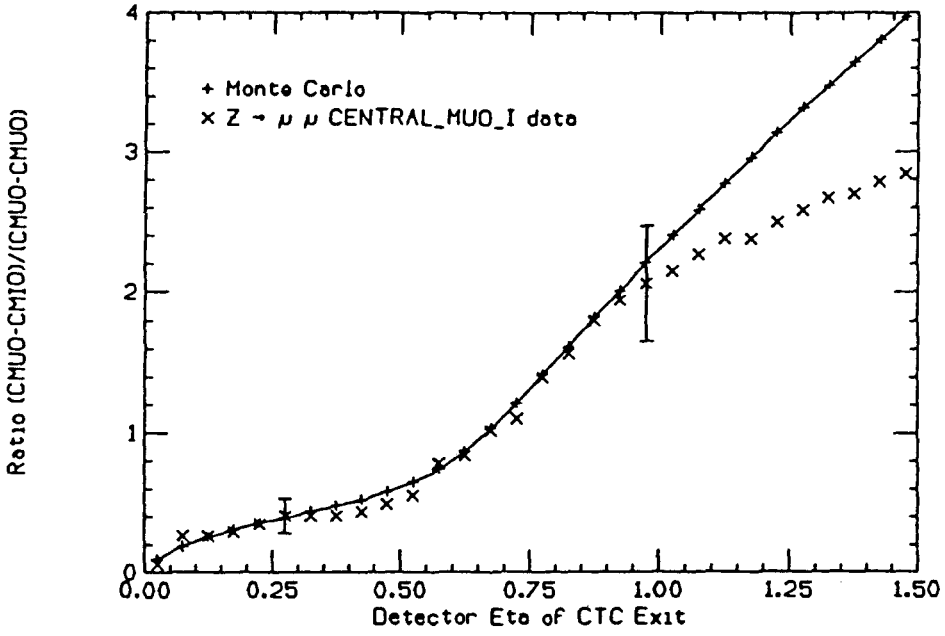

Figure A.6: Integral plot showing the ratio of CMUO-CMIO to CMUO-CMUO type Zs for both MC and data, showing the eta cut corresponding to the start of tracking ineffiency.

Appendix B

CDF/ANAL/MUON/CDFR/1525
Version 2.0

Correlation study for the muon cuts in the W/Z cross section measurements

D. Kardelis

Abstract

While correlations between the muon variables are present, most of these correlations are small and have no significant effect on the combined efficiencies. Using the product of the efficiencies creates no problems.

1 Introduction

This note discusses the study of correlations between the muon identification variables used in the muon R analysis. There are possible physical sources for correlations between the muon parameters used in the R analysis and the Z cross section measurement. Correlations between the EM/HAD (minimum ionization) deposition and δX (CTC-CMU matching) value could come from a muon depositing large amounts of energy in the calorimeter and, since the muon now has less momentum, it would multiple scatter more,thus having a broader δX distribution. The value of ISO (Isolation) and δX could be correlated through poorer track or muon reconstruction due to the higher multiplicity of particles near a non-isolated muon. Along the same lines ISO and EM/HAD energy deposition correlations may come from multiple particles traversing the muon tower.

2 Data Samples

The data sample used comes from Phase 3 (CDF1220)[1] that has been retracked and beam constrained. The cuts on Phase 3 were:
1 CMUO with

- $p_T \geq 18$ GeV/c

- Hadronic Energy (HAD) $\leq$ 12.5 GeV
- $|\delta X| \leq$ 10.0 cm.

To do this study, a subsample of Z events from Phase 3 was made with the requirements being opposite sign dimuon events, with both muon candidates having $p_T \geq$18 GeV/c, invariant mass between 65 and 115 GeV, and not flagged as a cosmic ray using CMUCOS, and one of the CMUO's passing the Phase 3 cuts. To increase statistics, the electron "bad runs" were not removed.

To get a sample with higher statistics than the above Z sample for the correlation study we went to the retracked PHASE 3 sample and selected a nojet W sample. Some cuts($\not\!\!E_T$ and p_T) in this analysis are tighter than those used in the muon R analysis to try to eliminate backgrounds in the W sample since we expect the muon variables to be highly correlated for background events.

This nojet W sample required:

- run number not be in the BADRUN list
- run number not be in the muon bad trigger list(see CDF-1029)[2]
- require events to have no jet (uncorrected jet $E_T \geq$ 10.0 GeV)
- $\not\!\!E_T \geq$ 30 GeV
- 65 GeV/$c^2 \geq$ Transverse Mass
- A CMUO bank with
  - $p_T \geq$ 30 GeV/c
  - Isolation $\leq$ 0.1
  - Ehad $\leq$ 12.5 GeV (Phase 3 requirement)
  - $|\delta X| \leq$ 10.0 cm (Phase 3 Requirement)
  - a Level 2 Central Muon Trigger associated with this CMUO
  - muon not associated with a cosmic ray by CMUCOS routine
  - muon not in a bad chamber

A third sample used is the cosmic ray data used for the muon trigger studies of CDF937[3] and the tracking studies of CDF965[4]. The only explicit muon quality cut used in this sample is a CMUO must be present and have a $p_T \geq$ 20 GeV/c. From CDF937, we see that the muons that do not have a trigger tend to have larger δX values than for those muons that do have a trigger. This correlation should cause no problems with our δX efficiency, since we required the muons in the δX efficiency study to have a muon trigger.

3 The Measurement

3.1 Method

To look for a correlation between 2 variables, we use the linear correlation coefficient described in Bevington[5]. The solution to a linear fit (y=a + bx) for the slope b is

$$b = \frac{N\Sigma x_i y_i - \Sigma x_i \Sigma y_i}{N\Sigma x_i^2 - (\Sigma x_i)^2}.$$

If there is no correlation, we would expect the slope to be 0, since the values of y will have no tendency to increase or decrease. There is the possibility for a correlation that yields a small slope, thus the magnitude of the slope alone is not enough to look for a correlation. Fitting x = (a' + b'y) and solving for b', we find that b = 1/b' or bb' = 1 for completely correlated variables, while for no correlation we expect b' to also be zero. Bevington then defines the linear correlation coefficient, r = $\sqrt{bb'}$ with r having the same sign as b. For correlated variables, |r| is near 1, and near 0 for uncorrelated variables. The sign of r does not matter, as it is just the magnitude of r that is important. In a practical form

$$r = \frac{N\Sigma x_i y_i - \Sigma x_i \Sigma y_i}{[N\Sigma x_i^2 - (\Sigma x_i)^2]^{1/2}[N\Sigma y_i^2 - (\Sigma y_i)^2]^{1/2}}.$$

The linear correlation coefficient, r, can not be used by itself to indicate correlations since this would necessitate knowing the correlation coefficient of the parent populations. In order to use the linear correlation coefficient, r, we compare it to a sample known to be completely uncorrelated. We use the integral probability that a random sample of uncorrelated data points from 2 gaussians would give a value of the linear correlation coefficient as large or larger than the observed value r. Probability curves versus number of events for constant values of r are shown in figure 1. Equations and programs for calculating the probability and integral probability are given in Bevington Chapter 7. Slightly modified versions of this code is avaliable in USR$ROOT33:[EVAD.ANA.FIT]. The necessary routines are GAMMA,RATIO_GAMMA, PCORRE, and FACTOR.

To double check if two variables are correlated beyond the cut regions, we compare the number of events that actually fail both cuts to the number predicted to fail both. If we let PP be the number of events that pass both cuts, PF be the number of events that pass cut 1 and fail cut 2, and FP the number of events that fail cut 1 but pass cut 2, then we can predict FF, the number of events that should fail both cut 1 and 2. For uncorrelated variables, the ratio of FP/PP = FF/PF should hold. Thus FF, or the number of events that we expect to fail both cuts is

$$FF = (FP \times PF)/PP$$

for uncorrelated variables. After we have determined whether there is a correlation or not, for the cases where there are correlations we have to then decide how much of an effect the correlation has on our combined efficiencies.

Table 1: Summary of results for Isolation and δX

Data	r	Prob(%) Uncorr	PP	PF	FP	FF (meas)	FF (pred)	$<\epsilon 1><\epsilon 2>$ (%)	$<\epsilon 1\epsilon 2>$ (%)
Z	0.039	72	79	7	3	0	0.4 ± 0.2	89.0	$88.7\ \pm^{3.4}_{4.4}$
W	0.017	66	637	31	3	0	0.15 ± 0.09	94.9	$94.9\ \pm^{0.8}_{1.0}$

3.2 Isolation and δX

While using the Z sample, the cuts used vary slightly depending on which cuts we are studying. For example, while looking for correlations between ISO and δX , the cuts on the muon being studied were a fiducial muon (FIDCMU = 0), $p_T \geq 18$ GeV/c, EM$\leq$ 2.0 GeV, HAD $\leq$ 6.0 GeV, plus the leg not being studied must pass the cuts of Phase 3. To increase statistics in this study of the Z sample if the first muon passes the Phase 3 cuts, we look at the second muon. Then, if the second muon passes the Phase 3 cuts and we go back and study the first muon. In general all the cuts used in the R analysis of CDF1349 are made on the leg being studied except the 2 cuts being studied. For the linear correlation coefficients , r, that involve δX measurements, the absolute value of δX was used since the correlations are expected to be sign independent.

We start by looking at the Isolation(ISO) vs δX distributions. Figure 2 shows the mass distribution for the Z sample used for the isolation δX study . Figure 3 is the unbounded Isolation vs δX distribution. Figure 4 is the same distribution except bounded by the analysis cuts of the R measurement. From figure 4 no events fail both cuts simultaneously. This null result is consistent with the 0.4 ± 0.2 events predicted for FF for uncorrelated variables. The linear correlation coefficient r for the Z sample is 0.039. The probability of getting this result or greater from 2 uncorrelated samples is 72%. The results of this section are summarized in Table 1.

To study the Isolation and CTC-CMU match correlations using the W sample, a slightly modified no-jet W sample was used. The cuts were the same as listed for the no-jet W sample in section 2 except for:

- the Minimum Ionizing cut was used (EM$\leq$ 2.0 GeV, HAD$\leq$ 6.0 GeV)
- the isolation requirement was removed.

The Isolation vs δX distributions for the W sample along with their profiles are plotted in figures 5 and 6, unbounded and bounded, of course. A profile plot is the plot of the mean of all the events in each bin. The error on the mean is the width as calculated by Hbook divided by the square root of the number of events in the bin. All the profile plots in this note do not show any bin that has less than 5 events in it. From the profile plot of figure 5, there is no correlation seen. We do not see an excess of events failing both cuts

Table 2: Summary of results for Electromagnetic Energy and δX

Data	r	Prob(%) Uncorr	PP	PF	FP	FF (meas)	FF (pred)	$<\epsilon 1><\epsilon 2>$ (%)	$<\epsilon 1\epsilon 2>$ (%)
Z	0.034	75	81	8	1	0	0.1 ± 0.1	90.1	$90.0 \pm^{3.2}_{4.2}$
W	-0.013	74	641	31	13	0	0.6 ± 0.2	93.7	$93.6 \pm^{0.9}_{1.0}$
Cosmic	0.012	58.3	2064	84	16	0	0.7 ± 0.2	95.4(5cm)	95.4 ± 0.5

simultaneously. We would expect .15 events to fail both cuts for uncorrelated distributions, we see 0. The linear correlation coefficient r is 0.017 and which yields 66% probability of being uncorrelated. These 2 variables are uncorrelated. The measured value of the two efficiencies is the same as the product of the two indivivdual efficiencies. The product of the two is 640/671*668/671 = 94.9%, the actual efficiency is 637/671 = 94.9%. These results of this section are summarized in Table 1.

3.3 Minimum Ionization energy and δX

Next we look at the EM vs δX distributions. Figure 7 is the mass distribution for the Z sample used in this study. Figure 8 is the unbounded plot of EM vs δX , with figure 9 being the bounded distributions. From the distributions no strong visual evidence of a correlation between these variables is seen. From Figure 9, we see that no muon fails both these cuts simultaneously again consistent with the no-correlation prediction of FF = 0.1 events to fail both cuts. The linear correlation coefficient is 0.034. The probability of getting this result from two uncorrelated gaussians is 75%. The Z data is again uncorrelated. These results are summarized in Table 2.

To make this study with larger statistics, we used the nojet W sample as given in section 2. For the W sample, we have the unbounded EM vs δX distribution in figure 10, also in figure 10 is the relevant profile plot. Figure 11 is the bounded version of figure 10. From the profile plot in figure 10, no correlation is seen between the matching and the EM energy. The number of events that actually fail both EM and δX cuts is also consistent with no correlation being present. For no correlation, we would expect FF = $0.6 \pm .2$ events to fail both cuts and we see 0 events that fail both cuts. The linear correlation coefficient for this data sample is r = -0.013 and the probability of these variables being uncorrelated is 74%. Again no correlation is seen between these variables. These W results are also summarized in Table 2.

Next we look for correlations between the HAD and δX , Figure 12 is the unbounded HAD vs δX distribution for the Z data, with figure 13 being the same distribution bounded by the analysis cuts. The mass distribution for this data is in figure 5. From figure 13 we see that 1 muon does fail both cuts simultaneously while the expectation for FF,the number

Table 3: Summary of results for Hadronic Energy and δX

Data	r	Prob(%) Uncorr	PP	PF	FP	FF (meas)	FF (pred)	$<\epsilon 1><\epsilon 2>$ (%)	$<\epsilon 1\epsilon 2>$ (%)
Z	0.144	18	80	7	2	1	0.2 ± 0.2	88.1	$88.9 \pm^{3.4}_{4.4}$
W	0.049	20	650	31	4	0	0.2 ± 0.1	94.9	$94.9 \pm^{0.8}_{0.9}$
Cosmic	0.113	0	2050	81	30	3	1.2 ± 0.3	94.7(5cm)	94.7 ± 0.5

of events that fail both cuts, for uncorrelated variables is 0.2 ± 0.2 events. The measured 1 event is higher than we would expect, and gives an indication of a correlation. The correlation coefficient is .144 for the Z data, which is consistent with uncorrelated distributions only 18% of the time. We summarize these results in Table 3.

Using the larger W sample, figure 14 shows the unbounded distribution and profile plot of hadronic energy deposition and δX for the W sample and figure 15 is the bounded version of figure 14. From the profile plots of figure 14, a correlation is present. If these two variables were uncorrelated, we would expect 0.3 ± 0.2 events to fail both cuts. We see 0 events that fail both cuts simultaneously. For the hadronic calorimeter, the mean is slightly over 2 GeV with an rms of about 0.8 GeV, the 6 GeV cut is about 5 sigma from the mean. The effect of the correlation moves the mean from slightly over 2 GeV to slightly above 2 GeV. At this level, the difference between a 4 sigma cut and a 5 sigma cut is insignificant. Looking at the linear correlation coefficient for the W sample, r = 0.049. The probability that these variables are uncorrelated is 20%. The actual effect of the correlation on the combined efficiency is tiny. For the multiplicative result, the combined efficiency is (654/685)*(681/685)= 94.9%. The actual efficiency is $650/685 = 94.9 \pm^{0.8}_{0.9}\%$. Even though these variables are correlated, the effect of the correlation on the actual efficiency is negligible. These results are summarized in Table 3.

3.4 Minimum Ionization energy and Isolation

Moving on to the Energy deposition vs Isolation, first in figure 16 we plot the invariant mass distribution for the Z sample of the Isolation-minimum ionizing energy sample. Figure 17 shows the unbounded EM vs ISO distribution for the Z sample followed by the bounded distribution in figure 18. In figure 18, we do see that one event fails the both the EM and ISO cuts, while we would expect FF = 0.02 ± 0.03 events for uncorrelated samples. The linear correlation value is 0.551 and the resulting probability is 0% for non-correlation. Table 4 is the summary of these results.

We use the W sample to study the Isolation and EM correlations with larger statistics. The cuts were the same as for the W sample listed in section 2 except for:

- require $|\delta X| \leq 2.0$ cm

Table 4: Summary of results for Electromagnetic Energy and Isolation

Data	r	Prob(%) Uncorr	PP	PF	FP	FF (meas)	FF (pred)	$<\epsilon 1><\epsilon 2>$ (%)	$<\epsilon 1\epsilon 2>$ (%)
Z	0.551	0	81	3	1	1	0.04 ± 0.05	93.1	$94.2 \pm^{2.2}_{3.6}$
W	0.175	0	641	3	13	1	0.06 ± 0.06	97.3	$97.4 \pm^{0.6}_{0.8}$

- the isolation requirement was removed.

Figures 19 and 20 show the unbounded and bounded EM vs Isolation distributions with their profiles for the W events. Figures 19 and 20 show a correlation between ISO and EM. For uncorrelated distributions we would expect 0.1 event to fail both cuts and we see 1 event. The linear correlation coefficient, r, is .175 for the EM and isolation distribution. The probability of getting a value for the linear correlation coefficient greater than this from uncorrelated gaussian distributions is 0%. While there is some correlation between these 2 variables, its effect on the product of the efficiencies is negligible, especially when compared to the statistical uncertainty. The actual efficiency of the 2 cuts from figure 20 is 641/658 $= 97.4 \pm^{0.6}_{0.8}\%$ and the product of the efficiencies is 644/658*654/658 = 97.3%. These results are also summarized in Table 4.

The Hadronic energy vs Isolation distributions for the Z sample are shown in figures 21 (unbounded) and 22 (bounded). The mass distribution for this sample is seen in figure 18. No muon fails both the HAD cut and the ISO cut in figure 22 which is consistent with the no correlation prediction of 0.1 events for FF. The value of r, the linear correlation coefficient is 0.029. This value of r gives a probability of 79% that the 2 variables are uncorrelated.

Looking at the W sample of section 2, figures 23 and 24 show the Hadronic energy versus Isolation distributions, unbounded and bounded respectively. We see no events that fail both the HAD and ISO cuts in figure 24, which is consistent with the no correlation prediction. The linear correlation coefficient for the hadronic energy vs Isolation distribution is -0.007, yielding a 86% probability of being uncorrelated. The results of the hadronic energy and isolation variables is gathered in Table 5.

3.5 Cosmic Rays

Another check is to use the cosmic rays to search for correlations. The only requirement on the muons from cosmic rays is a CMUO with $p_t \geq 20.0$ GeV. There is a possibility of poor δX measurement from cosmic rays due to poor timing resolution. Regardless of this possible problem, we should be able to measure δX to 5 cm easily, the half width of a individual muon cell is about 3.2 cm. Due to the muon chamber's geometry and electronics, the side of the cell the muon passed on is unambiguous for a well-reconstructed muon. Plotted in figures 25 and 26 are the EM vs δX distributions for the cosmic ray data. Figure 25 is

Table 5: Summary of results for Hadronic Energy and Isolation

Data	r	Prob(%) Uncorr	PP	PF	FP	FF (meas)	FF (pred)	$<\epsilon 1><\epsilon 2>$ (%)	$<\epsilon 1\epsilon 2>$ (%)
Z	0.029	79	80	4	2	0	0.1 ± 0.1	93.1	$93.0 \pm^{2.7}_{3.9}$
W	-0.007	86	650	4	4	0	0.02 ± 0.01	98.8	$98.8 \pm^{0.4}_{0.6}$

the bounded distribution. It is bounded by a δX of 5 cm instead of the normal 2 cm cut to study correlations. For the EM vs δX distribution, we expect the number of events to fail both the 5 cm cut and the 2 GeV EM cut to be about 0.7, we see no events that fail both simultaneously. Calculating the linear correlation coefficient for the EM energy and δX distribution gives r = -0.012 which has a 58.3 % chance of being uncorrelated. These results are summarized back in table 2.

We also use the cosmic ray data to look at the Hadronic energy vs δX correlation. Figures 27 and 28 are the HAD vs δX distributions with profile plots, figure 28 being the bounded distribution. The distribution does not show as nice a correlation as figure 15 does. This may be in part caused by the timing in cosmic ray data. The hadronic energy and δX distribution has a value of r = 0.113 which has a 0 % chance of being from an uncorrelated sample. From figure 28, we would expect 1.2 events to fail both a 5 cm δX cut and the 6 GeV hadronic energy cut. We actually see 3. Again while there is a correlation, the effect on the efficiency is nil. The product of the 2 individual efficiencies is 94.7% and the efficiency from the direct measurement is $94.7 \pm 0.5\%$. These results for the cosmic rays are summarized back in table 3. The cosmic ray results while they may not be as pretty as the results from $p\bar{p}$ data are consistent with the actual collider data. Correlations are present but have a small effect on combined efficiencies.

4 Conclusions

There appear to be correlations present between several of the muon selection variables. The strongest of these correlations being between the EM energy deposition and the Isolation While these correlations are present, they do not have a strong effect on the resulting efficiencies obtained. This is mainly due to our cuts being fairly loose such that it requires a large change in the mean to have any effect on the efficiency. We conclude that using the product of the individual efficiencies presents no problem in calculating the W and Z cross sections.

5 References

1. CDF Note 1220, *The Making of a Muon Dataset*
2. CDF Note 1029, *Milestones of the Central Muon Trigger*
3. CDF Note 937, *Efficiency of the Level 1 Central Muon Trigger*
4. CDF Note 965, *CTC Tracking Studies with Cosmic Rays*
5. Bevington, P. R., *Data Reduction and Error Analysis for the Physical Sciences*

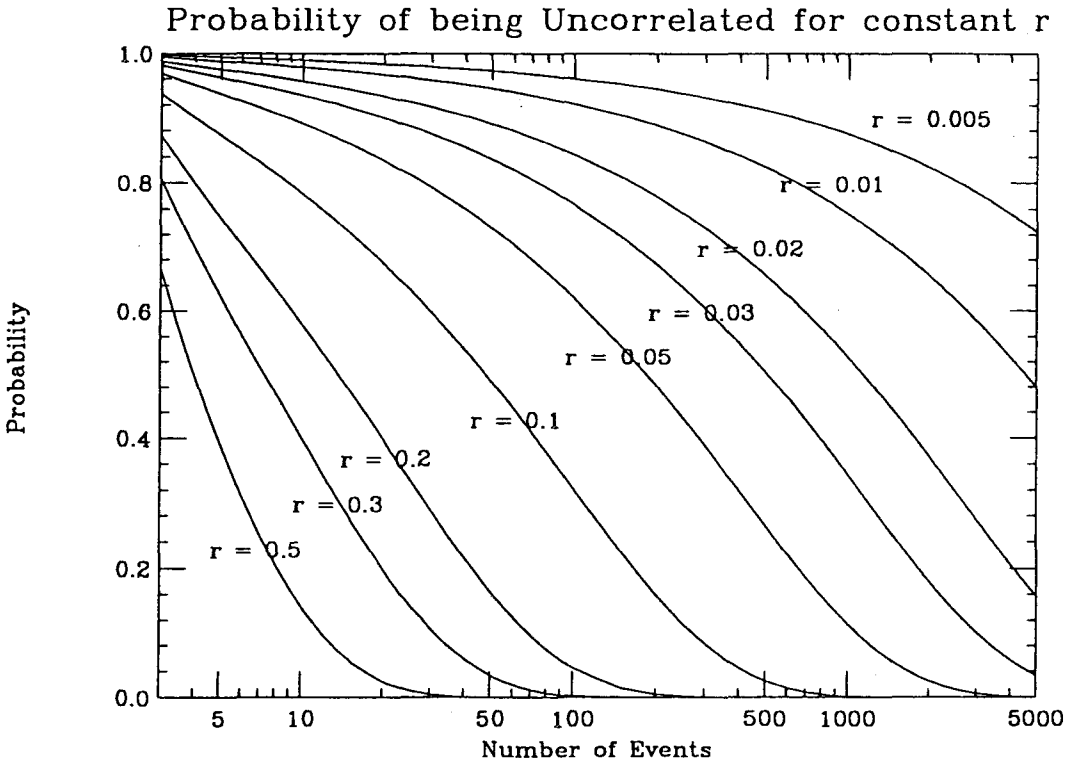

Figure B.1: Probability of Uncorrelation versus number of events for constant values of r

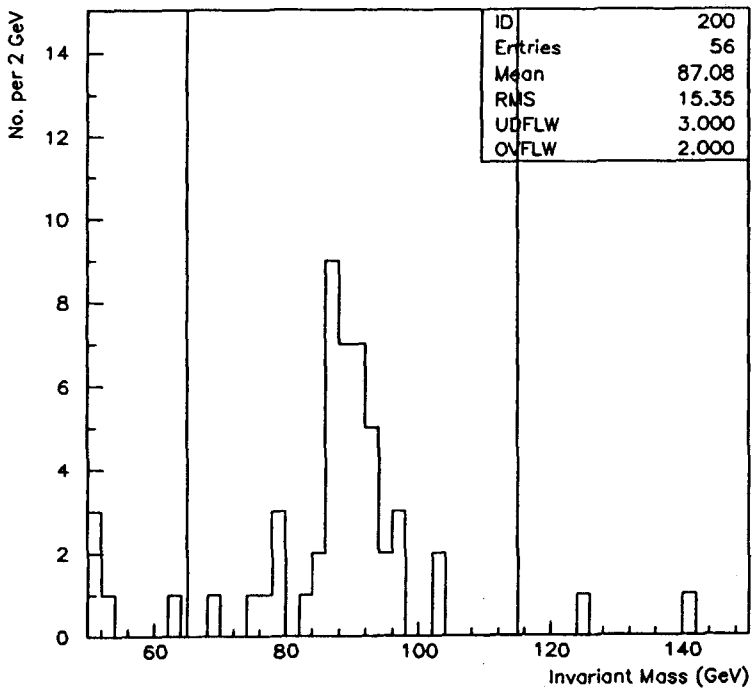

Figure B.2: Dimuon Invariant Mass distribution for the Isolation- CTC-CMU matching correlation study

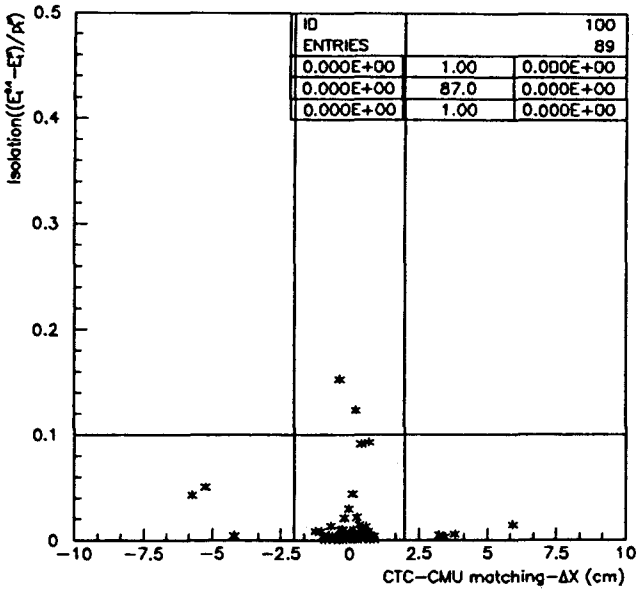

Figure B.3: Isolation versus CTC-CMU Matching-Z data(unbounded)

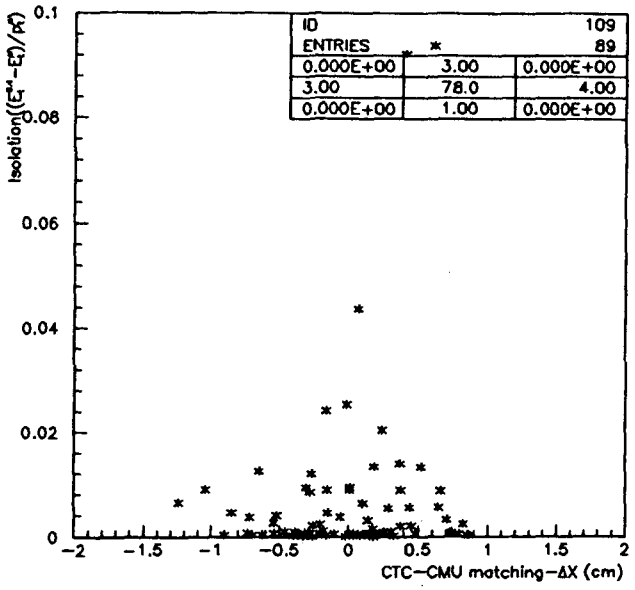

Figure B.4: Isolation versus CTC-CMU Matching-Z data(bounded)

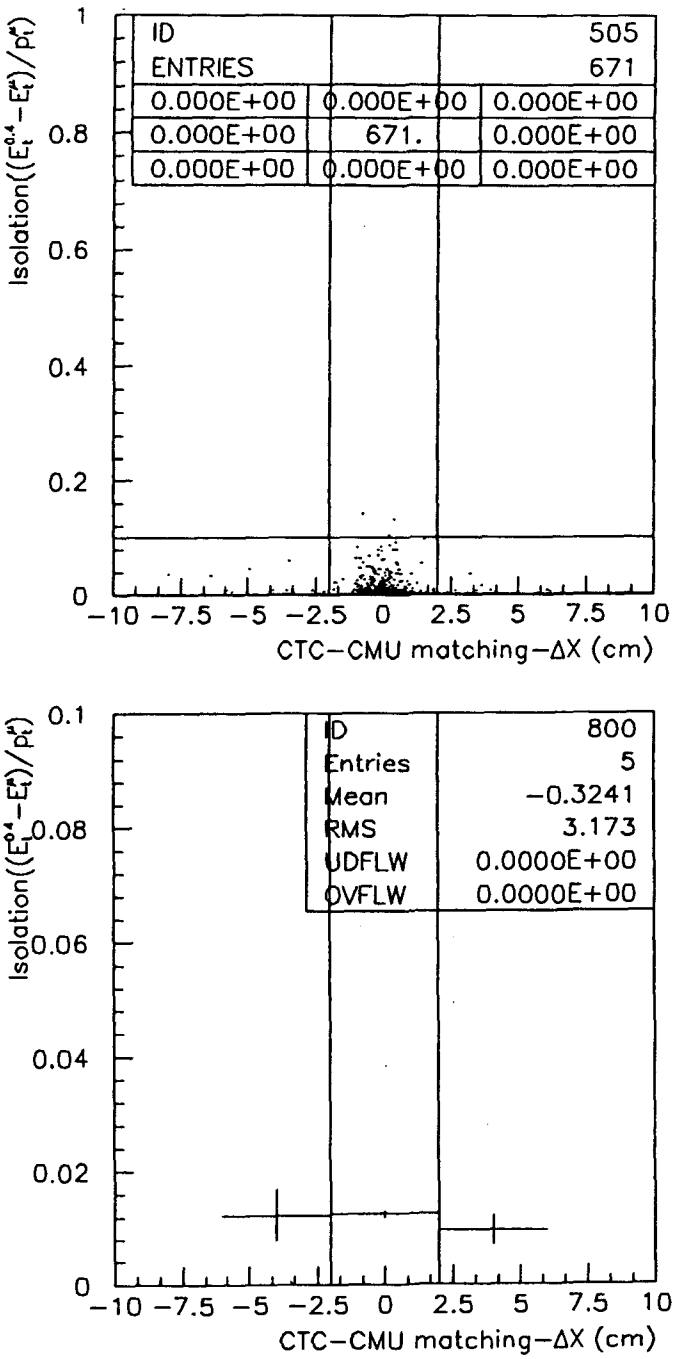

Figure B.5: Isolation versus CTC-CMU matching with profile (unbounded)-W data

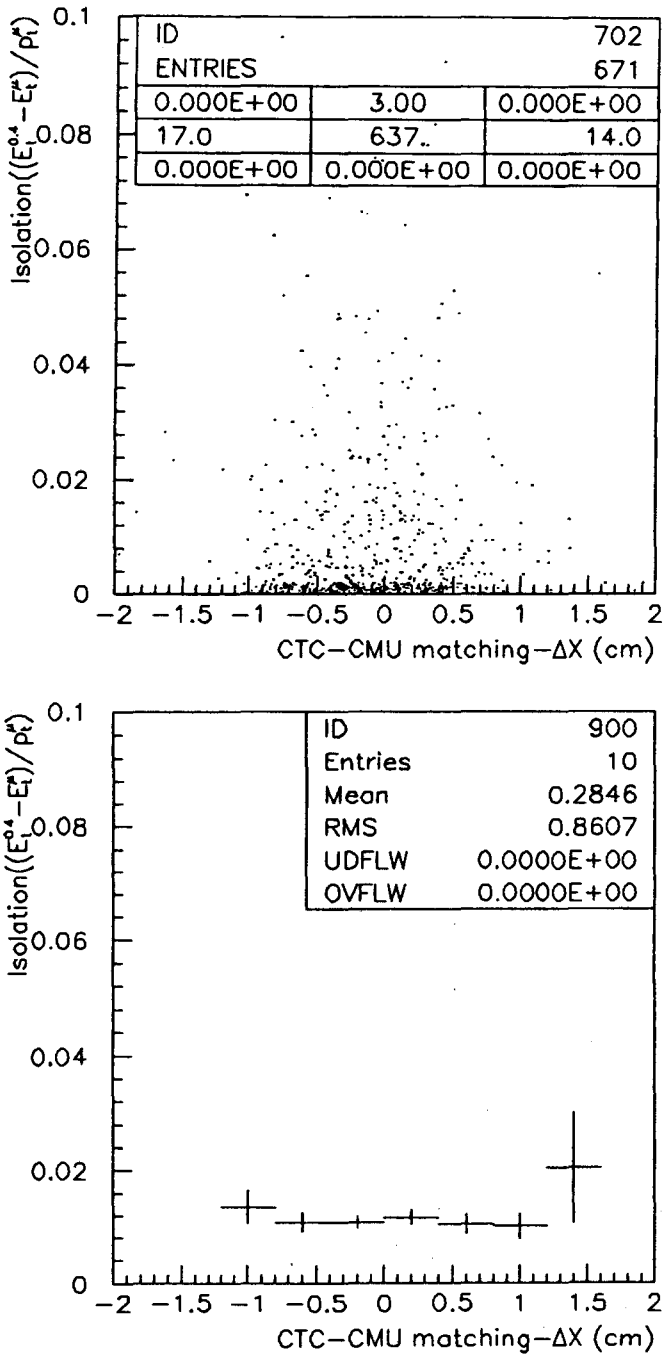

Figure B.6: Isolation versus CTC-CMU matching with profile (bounded)-W data

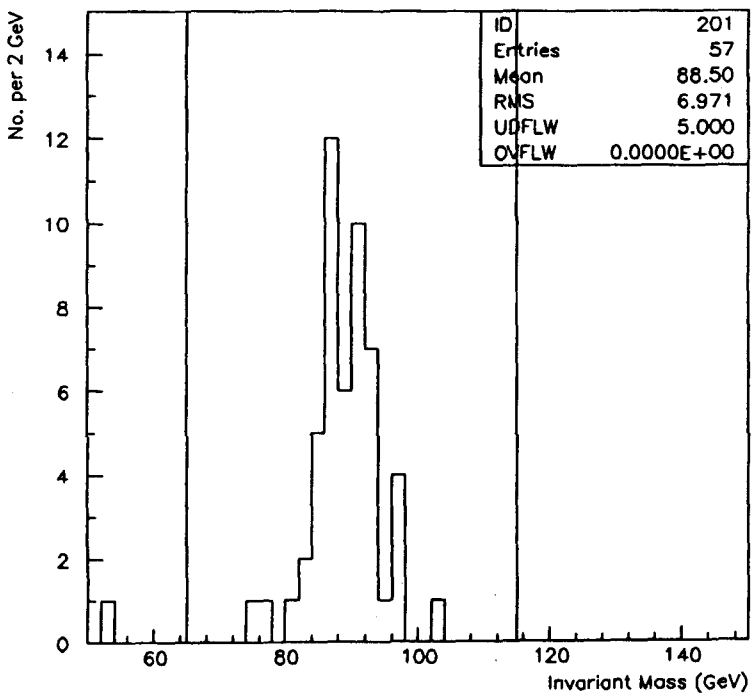

Figure B.7: Dimuon Invariant Mass distribution for Energy deposition - CTC-CMU matching correlation study

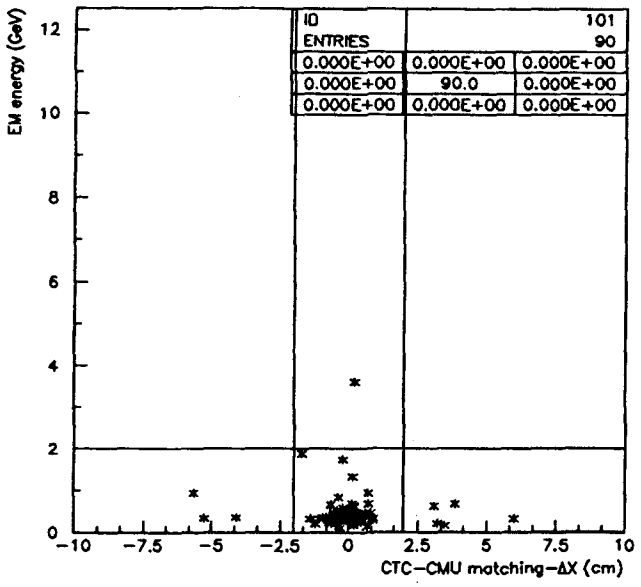

Figure B.8: EM energy deposition versus CTC-CMU Matching-Z data(unbounded)

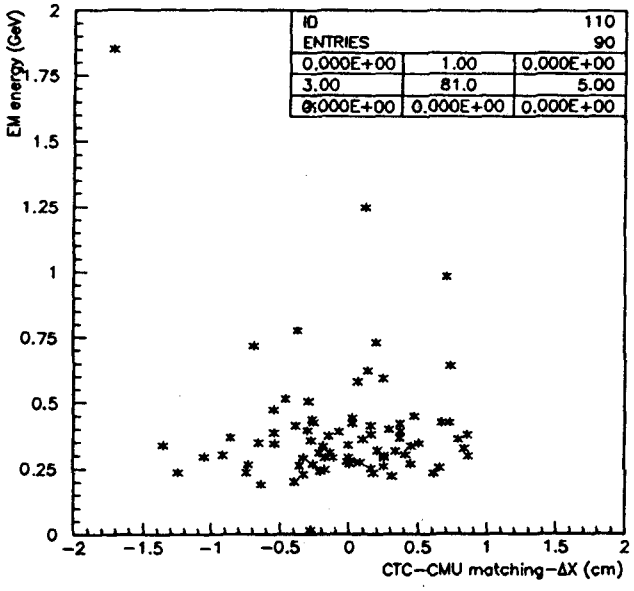

Figure B.9: EM energy deposition versus CTC-CMU Matching-Z data(bounded)]

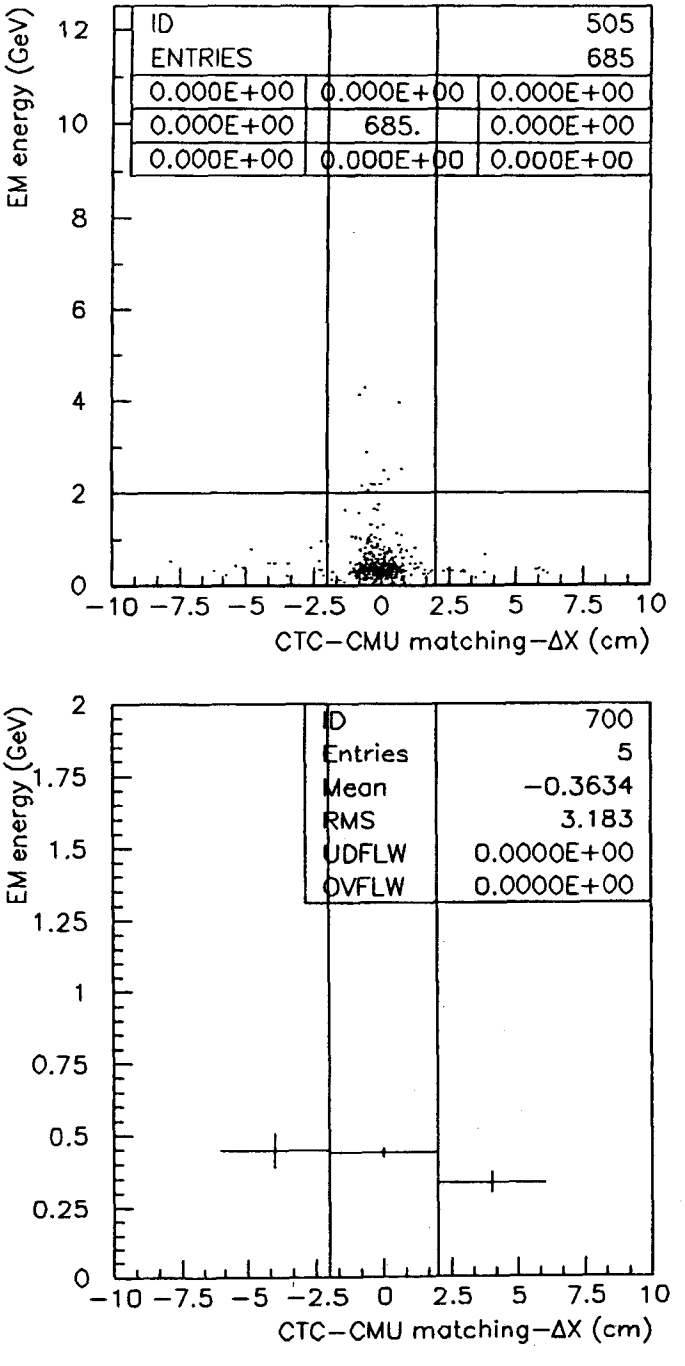

Figure B.10: Electromagnetic energy deposition versus CTC-CMU matching with profile (unbounded)-W data

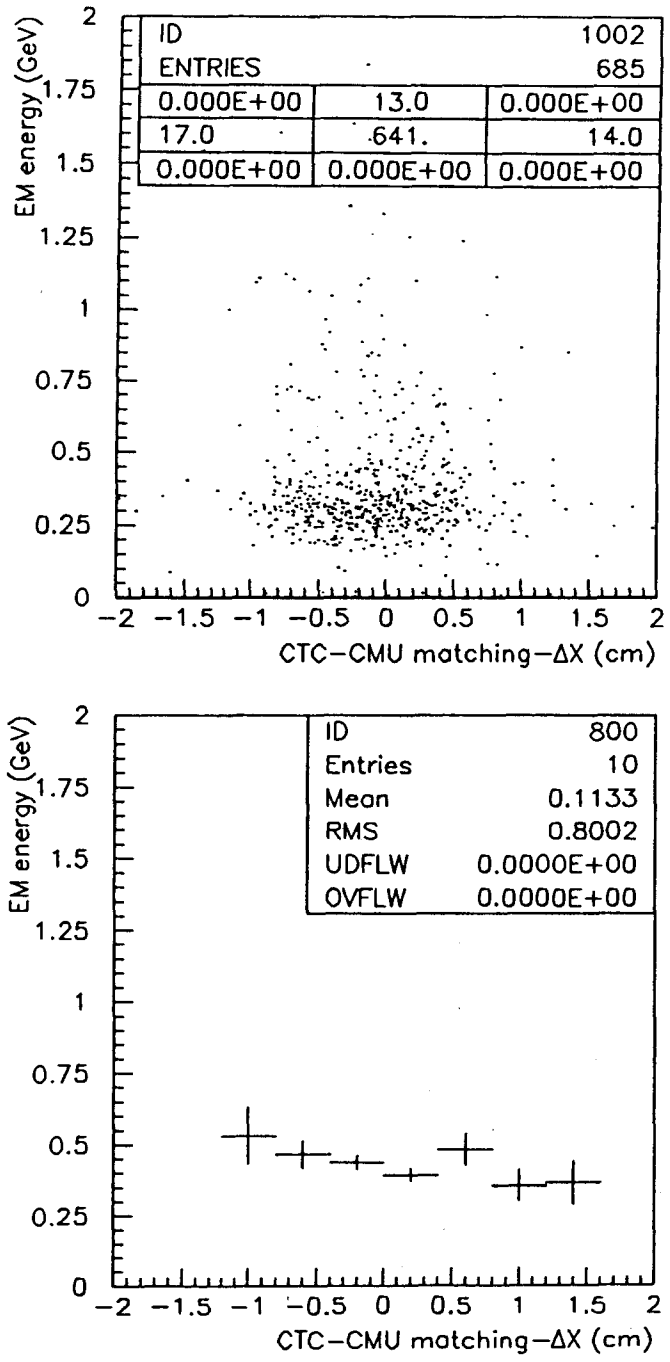

Figure B.11: Electromagnetic energy deposition versus CTC-CMU matching with profile (bounded)-W data

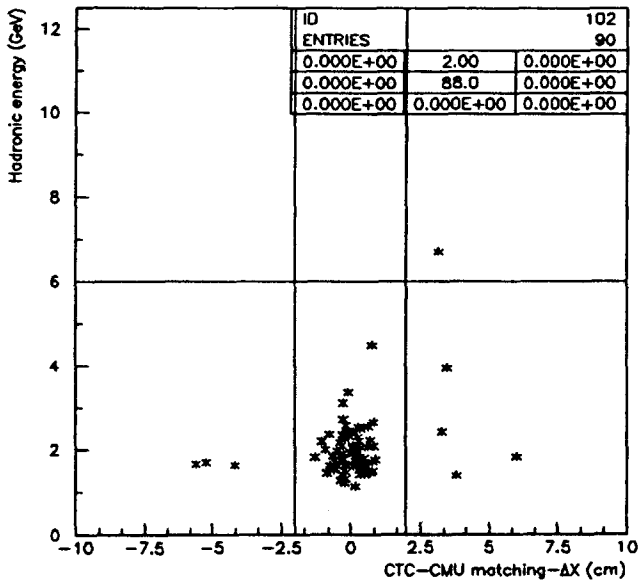

Figure B.12: Hadronic energy deposition versus CTC-CMU Matching-Z data (unbounded)

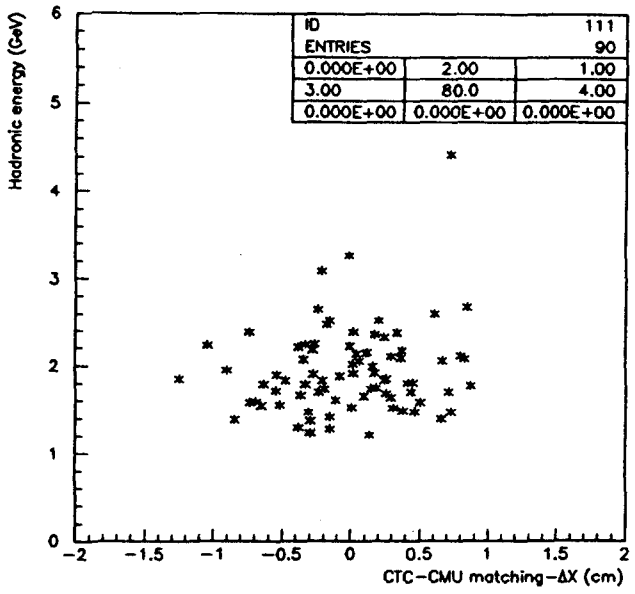

Figure B.13: Hadronic energy deposition versus CTC-CMU Matching-Z data (bounded)

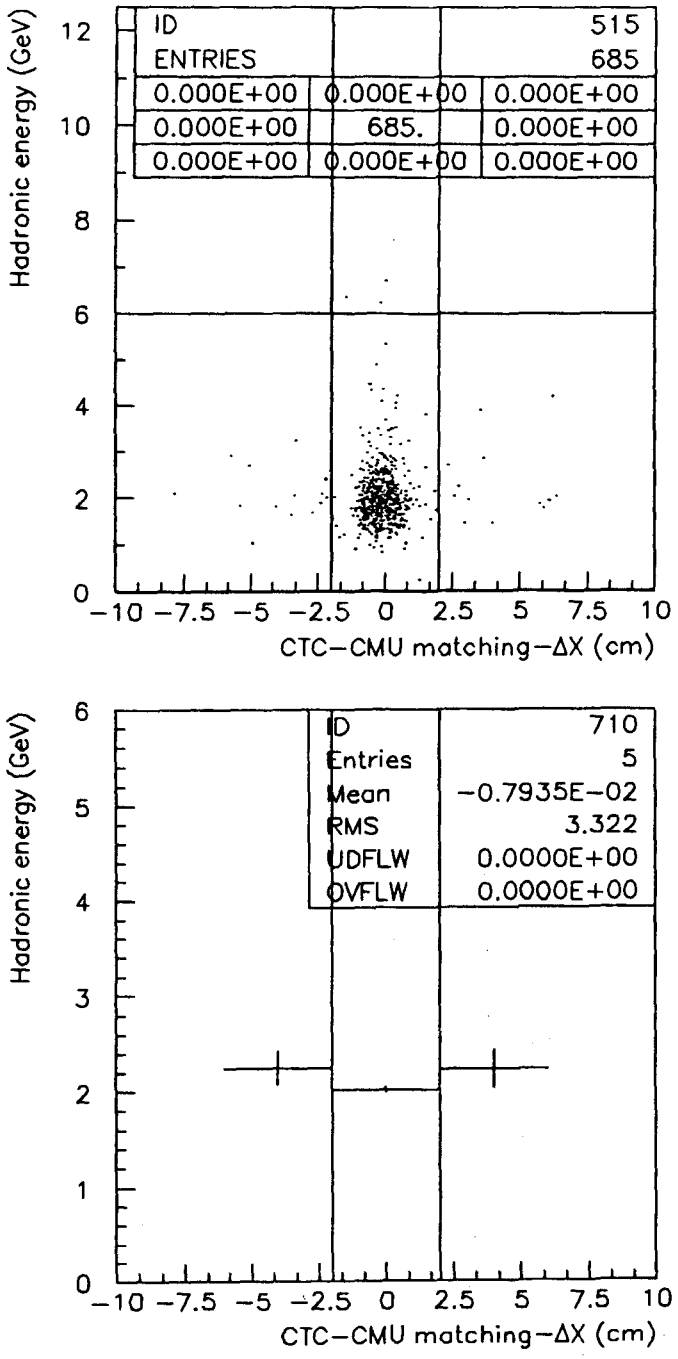

Figure B.14: Hadronic energy deposition versus CTC-CMU matching with profile (unbounded)- W data

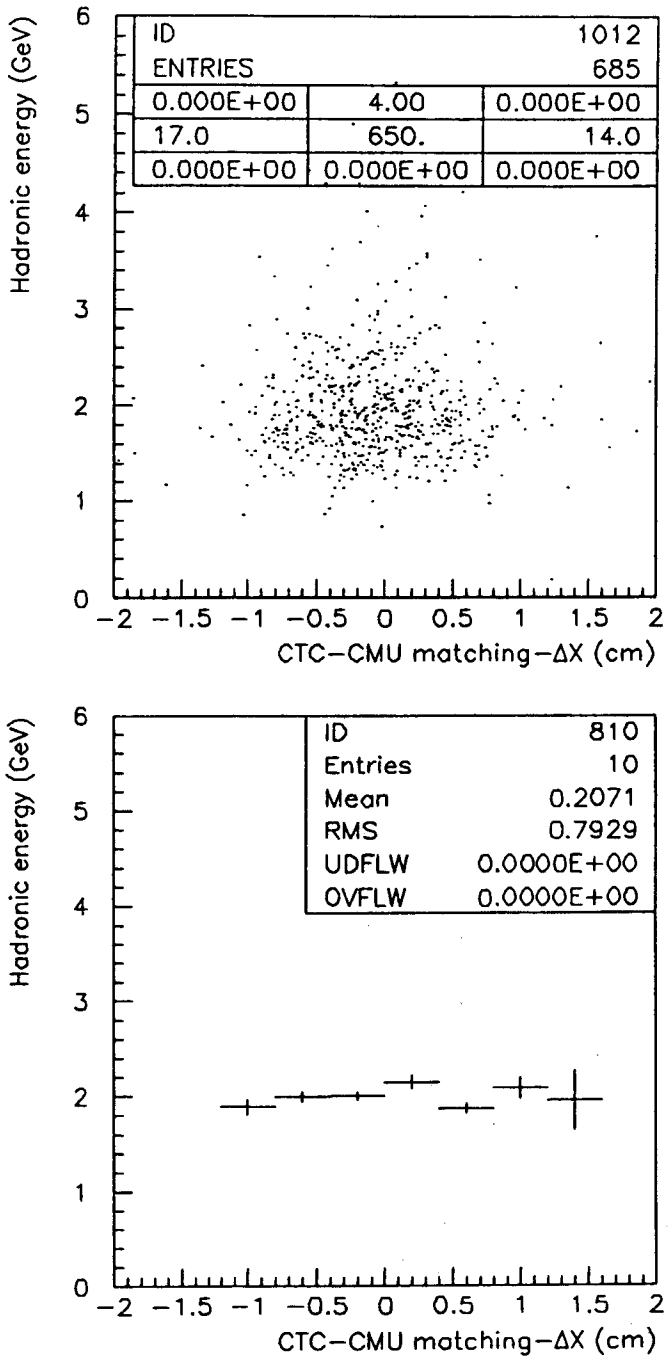

Figure B.15: Hadronic energy deposition versus CTC-CMU matching with profile (bounded)-W data

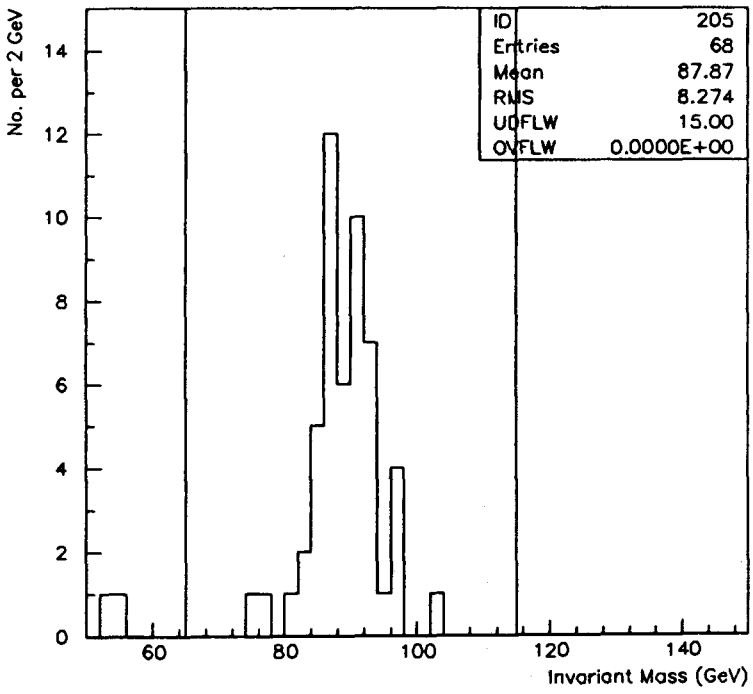

Figure B.16: Dimuon Invariant Mass distribution for Energy deposition - Isolation correlation study

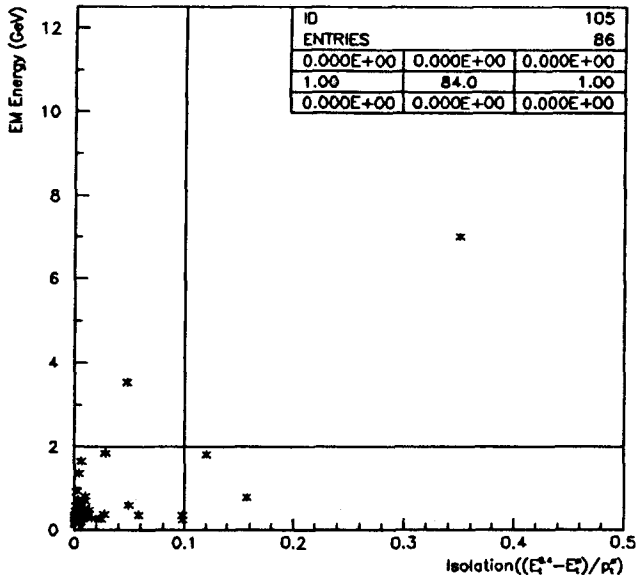

Figure B.17: EM energy deposition versus Isolation-Z data (unbounded)

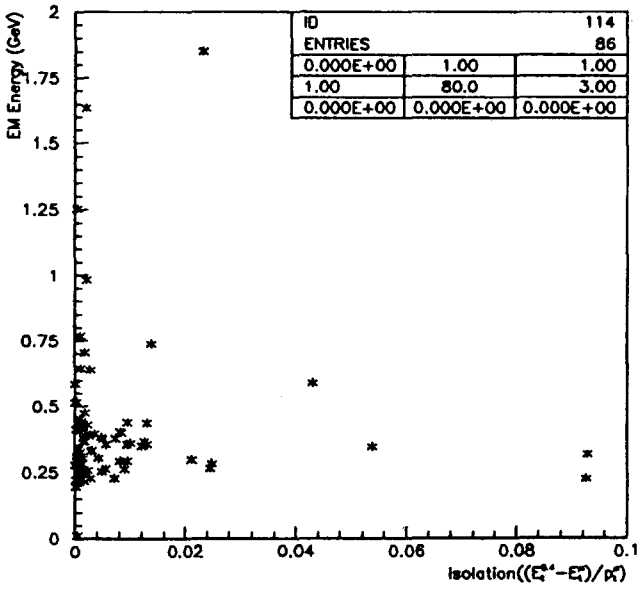

Figure B.18: EM energy deposition versus Isolation-Z data (bounded)

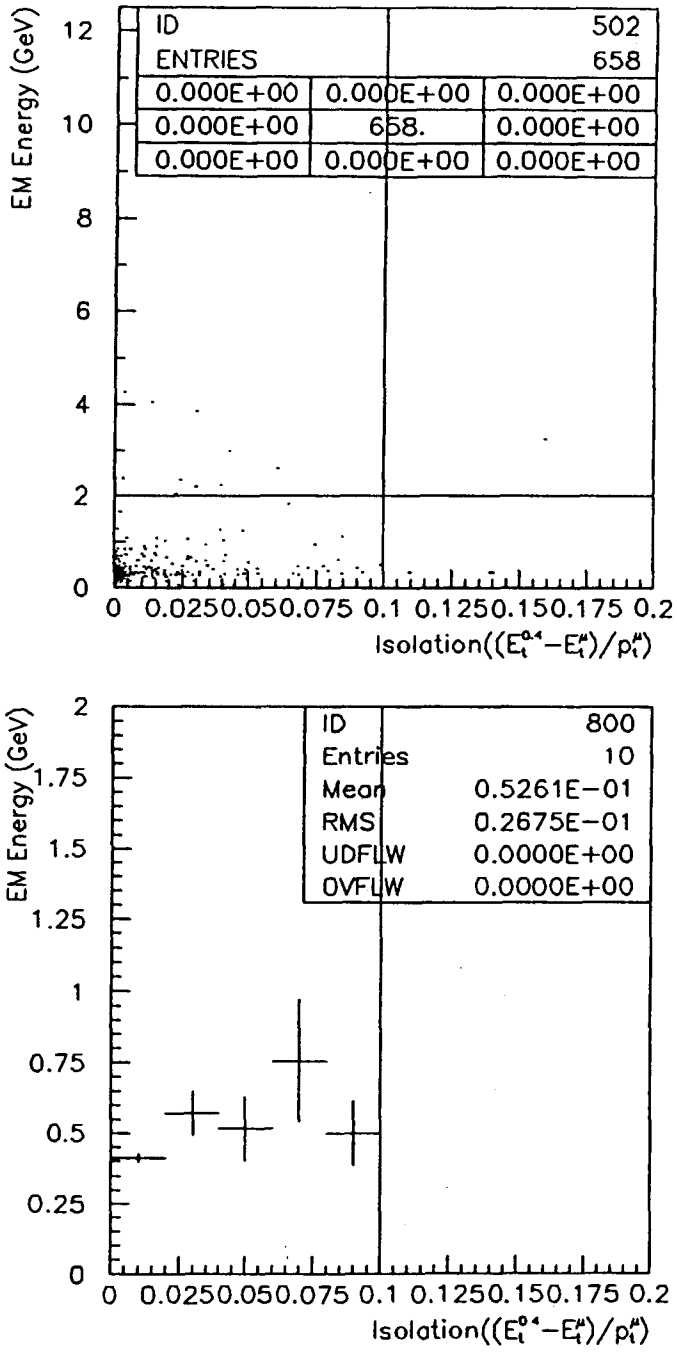

Figure B.19: Electromagnetic energy deposition versus Isolation with profile (unbounded)- W data

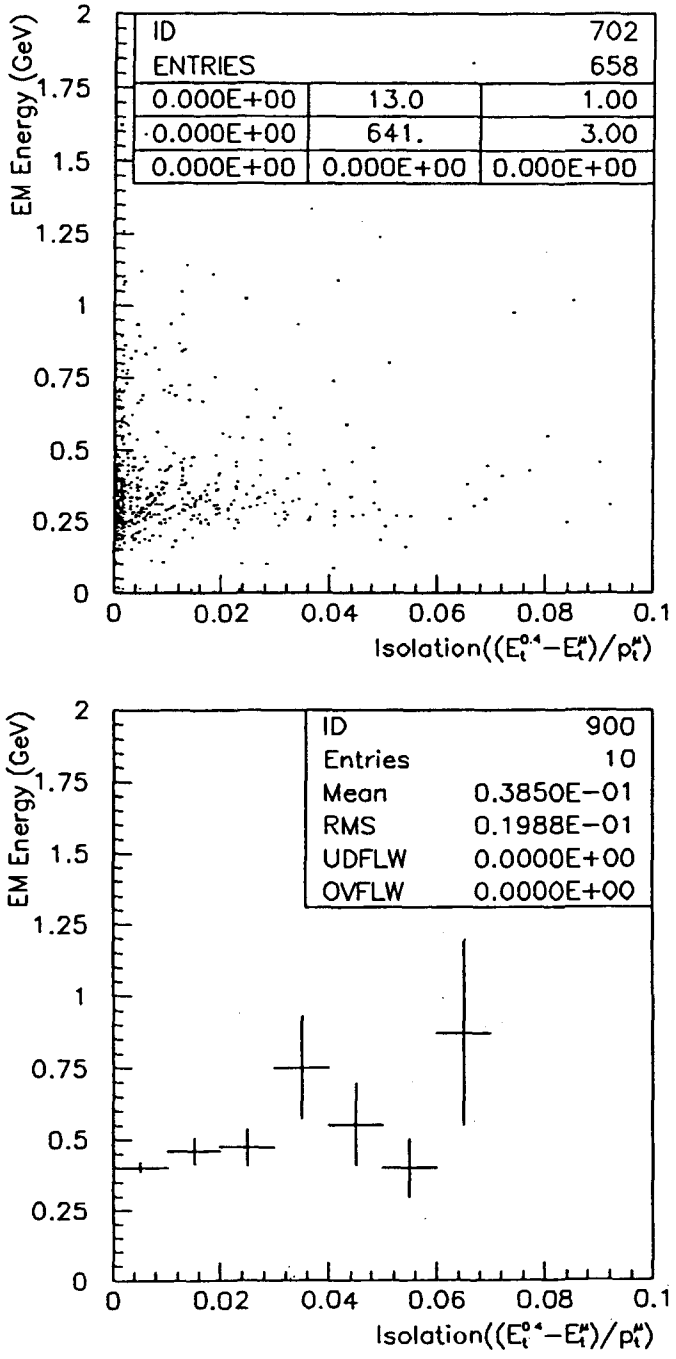

Figure B.20: Electromagnetic energy deposition versus Isolation with profile (bounded)- W data

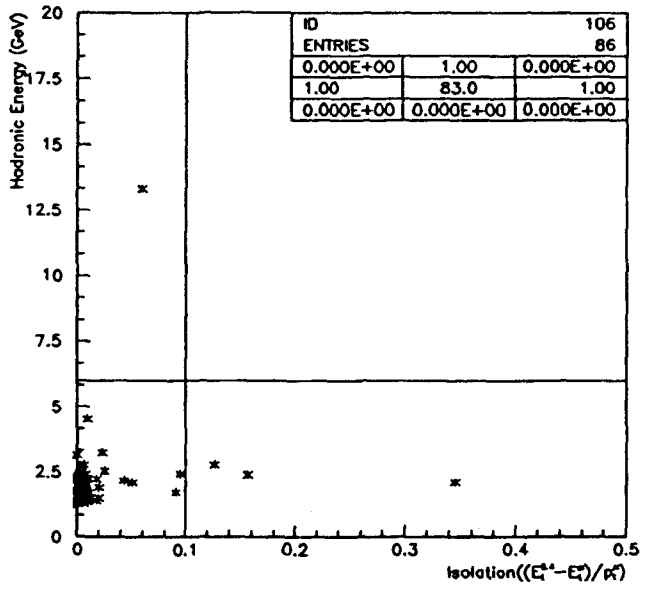

Figure B.21: Hadronic energy deposition versus Isolation-Z data (unbounded)

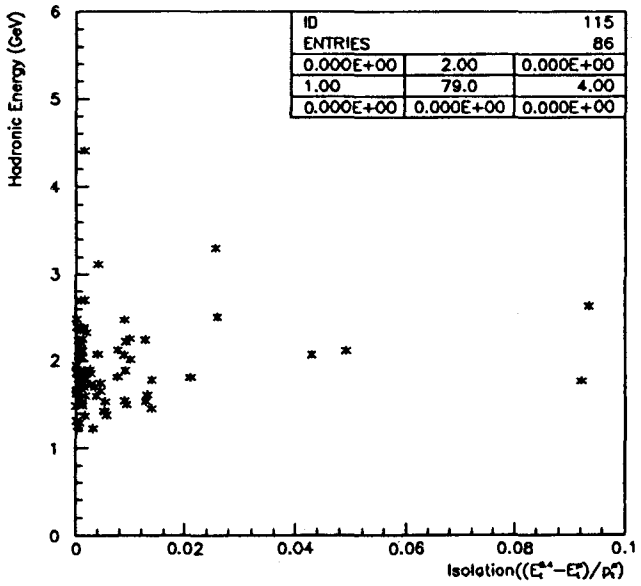

Figure B.22: Hadronic energy deposition versus Isolation-Z data (bounded)

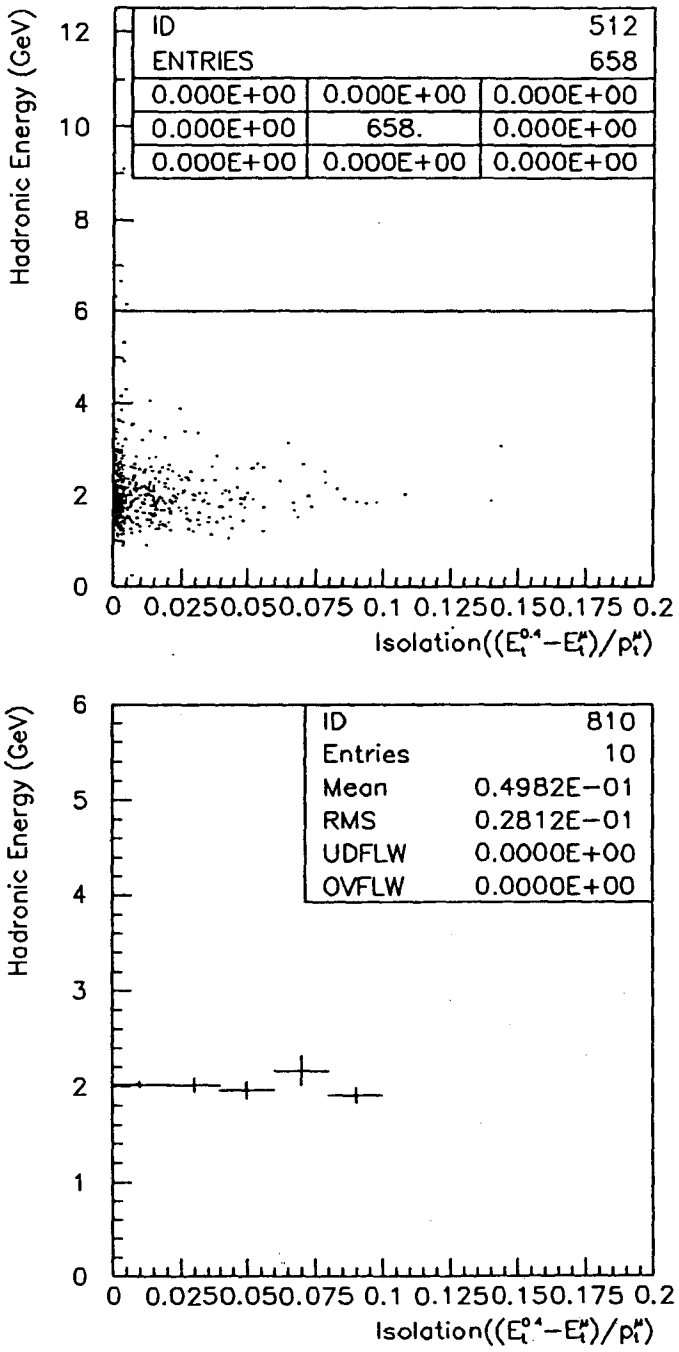

Figure B.23: Hadronic energy deposition versus Isolation with profile (unbounded)-W data

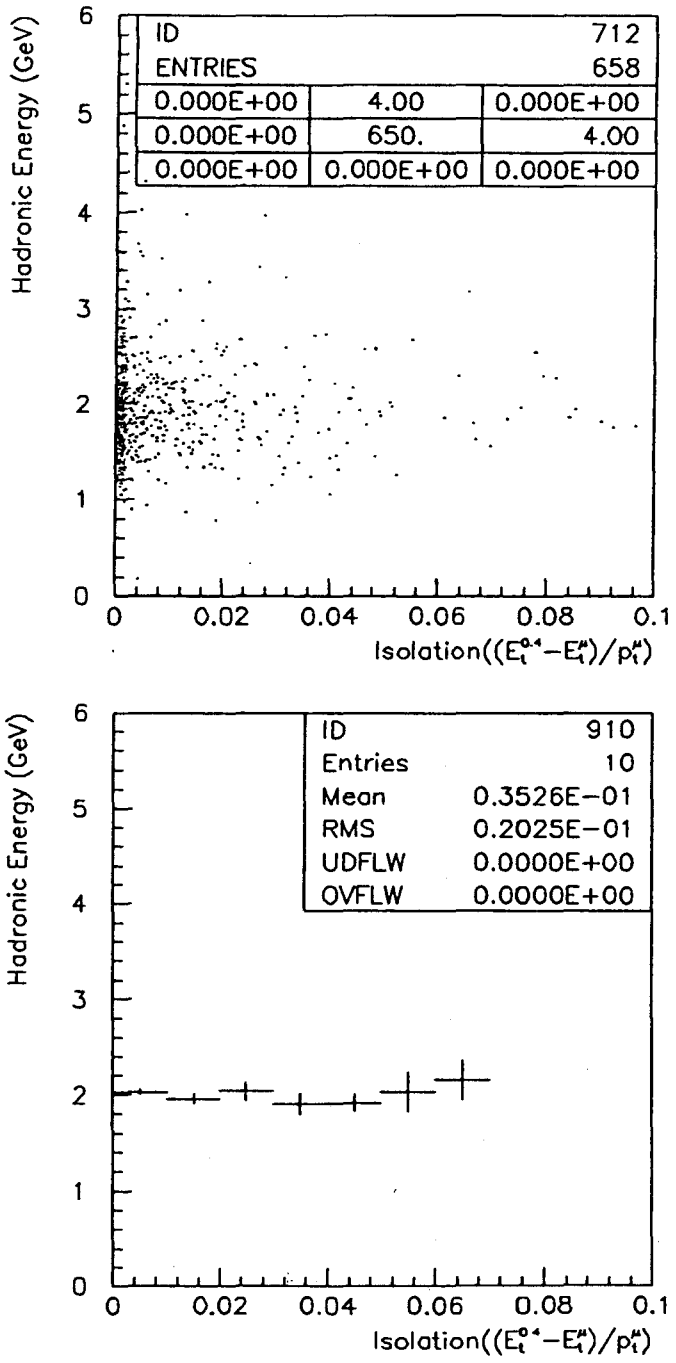

Figure B.24: Hadronic energy deposition versus Isolation with profile (bounded)-W data

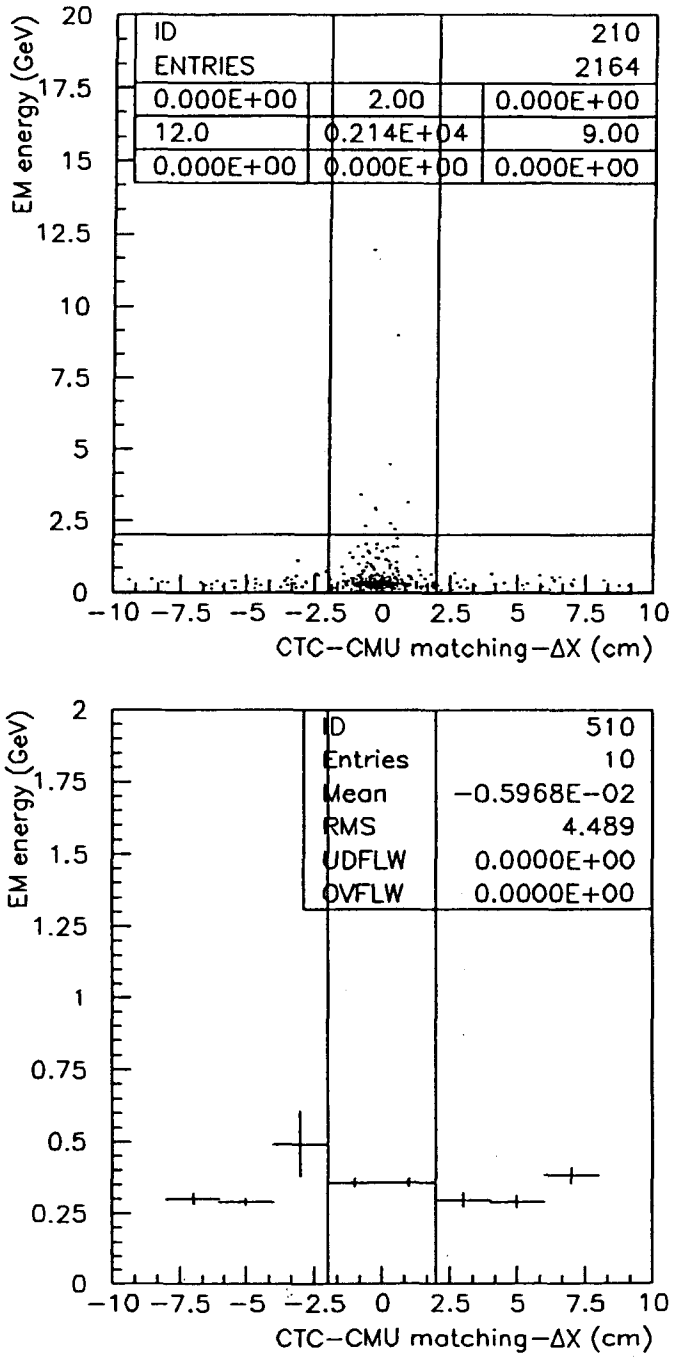

Figure B.25: Electromagnetic energy deposition versus CTC-CMU matching with profile (unbounded)-Cosmic Ray data

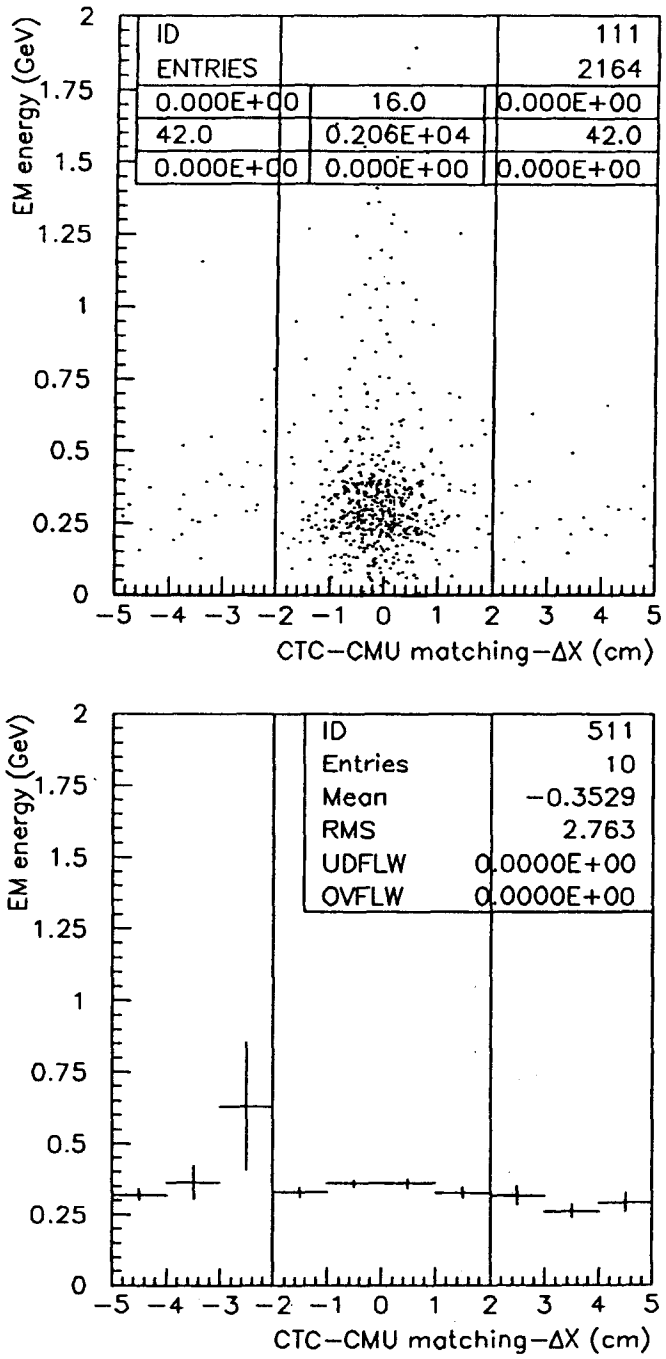

Figure B.26: Electromagnetic energy deposition versus CTC-CMU matching with profile (bounded)-Cosmic Ray data

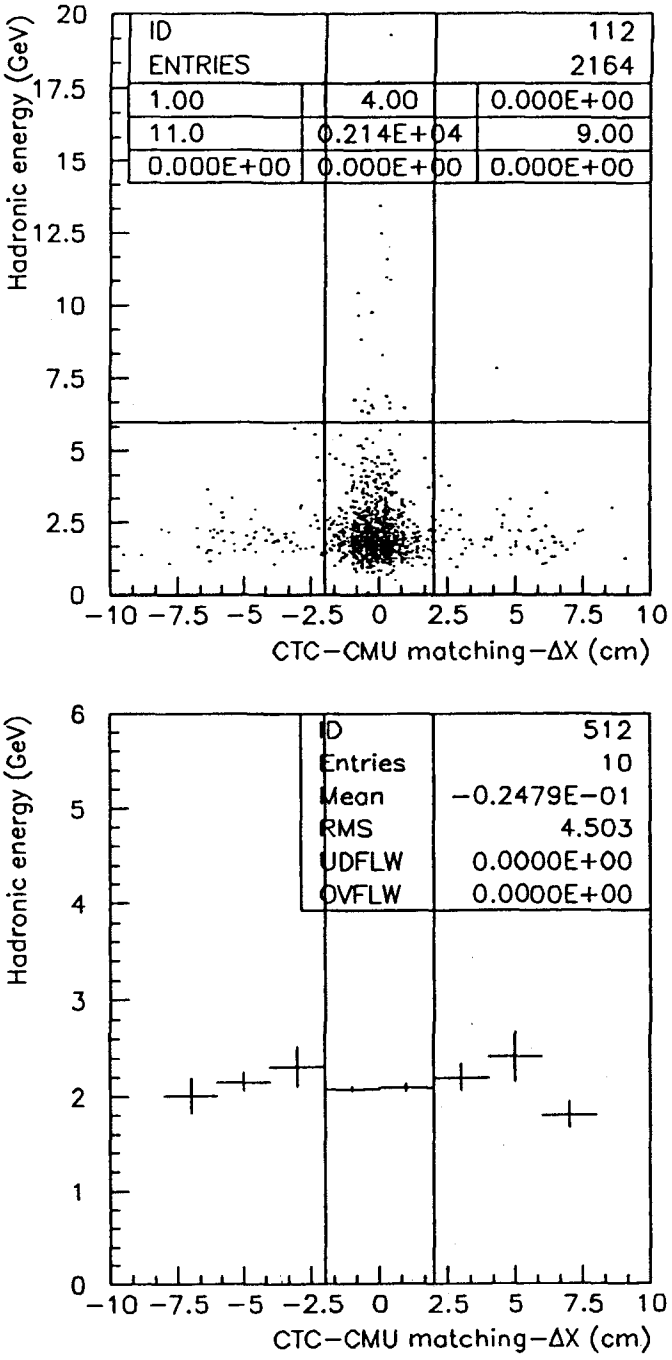

Figure B.27: Hadronic energy deposition versus CTC-CMU matching with profile (unbounded)-Cosmic Ray data

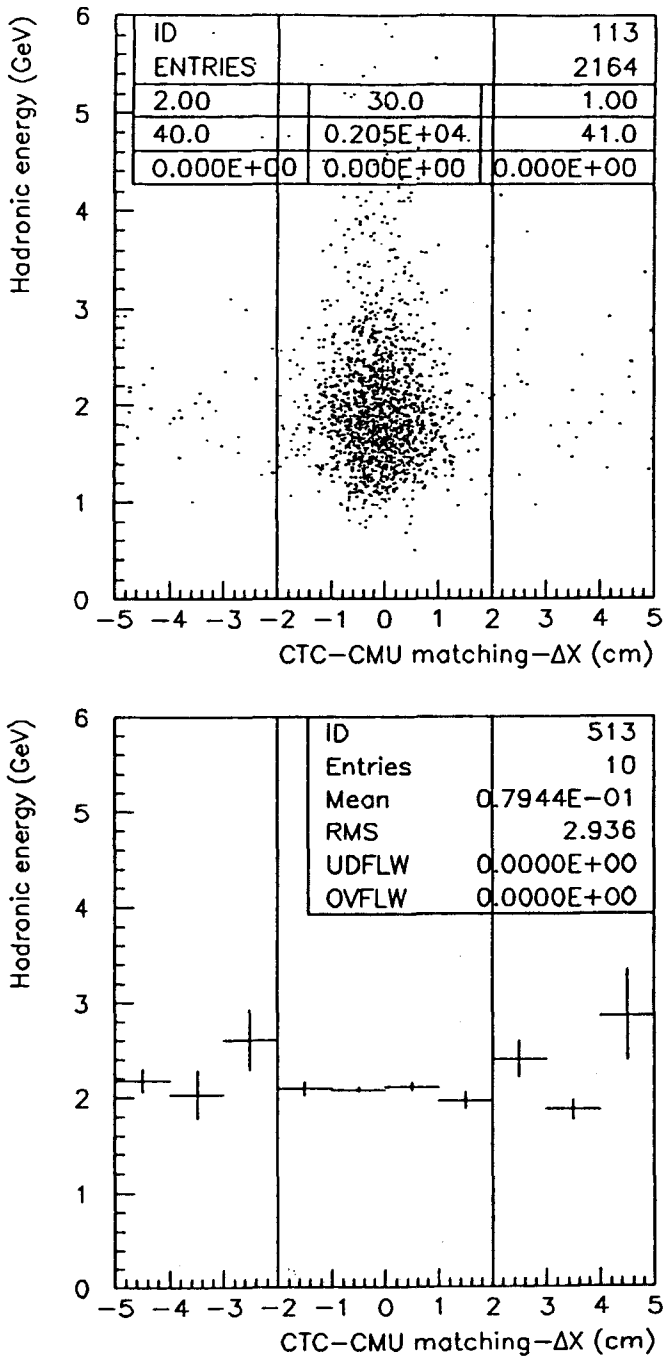

Figure B.28: Hadronic energy deposition versus CTC-CMU matching with profile (bounded)-Cosmic Ray data

Vita

Dave [redacted] At the age of 17, he ventured down to Champaign to get his education. While there he learned about beer, physics and building particle detectors. Towards the end of this schooling, Dave decided to venture across the sea to what he could see. This adventure placed him in Bangor, North Wales where he learned some physics, some Welsh and English history but mostly he learned about beer. He learned much about beer. and having learned what he could, he returned home. Finding there was no future in beer, he returned to particle detectors and the University of Illinois for graduate school. After many years and many beers, Dave finished his thesis but not before getting married. Dave was awarded his Doctorate in early 1994. With the thesis finished, Dave is looking towards a teaching career.